OBSERVATIONS OF MESOSCALE EDDIES OVER ROUGH TOPOGRAPHY IN THE WESTERN NORTH ATLANTIC

by

Stephen Craig Riser

B.S.E.E., Purdue University

(1971)

SUBMITTED IN
PARTIAL FULFILLMENT
OF THE REQUIREMENTS FOR THE
DEGREE OF MASTER OF SCIENCE

at the

MASSACHUSETTS INSTITUTE OF TECHNOLOGY

January, 1974

Signature of Author _____

Department of
Earth and Planetary Sciences
January 23, 1974

Certified by _____

Thesis Supervisor

Accepted by _____

Chairman, Departmental Committee
on Graduate Students

Observations of Mesoscale Eddies Over Rough Topography in the Western North Atlantic

by
Stephen Craig Riser

Submitted to the Department of Earth and Planetary Sciences on January 23, 1974 in partial fulfillment of the requirements for the degree of Master of Science

ABSTRACT

In planning for Mid-Ocean Dynamics Experiment I (MODE-I) three pilot arrays of moored current meters were set in an area of the western North Atlantic. Array-1 and Array-3 were set over smooth topography. Array-2 was set on rough topography centered on 68°25'W. 28°10'N. A chain of seamounts runs directly through the center of the array.

Vertical profiles of horizontal velocity and progressive vector diagrams are drawn from the data, and the shears are found to be somewhat higher than those determined from the smooth area in the region below the thermocline. Calculated spectra show two main features. First, there is a decided drop in coherence of velocity components between instruments separated by the ridge, and one measurement suggests that topography may be influencing the flow as high as 3700 m. above the bottom. Second, a smaller scale of variable flow with periods of 5 to 15 days is noted in the very deepest measurements but not higher in the column. A simple model is developed that suggests this variability is consistent with bottom trapped waves forced by the topography acting on the larger scale flow.

Thesis Supervisor: Carl Wunsch
Title: Associate Professor of Oceanography

ACKNOWLEDGEMENTS

The author is indebted to Dr. Carl Wunsch for the guidance, support, and encouragement he has given freely while this work was in progress.

This work was supported by the National Science Foundation, as part of the International Decade of Ocean Exploration, under contract GX29034.

TABLE OF CONTENTS

Page

Abstract.....2

Acknowledgements.....3

List of Tables and Figures.....5

Chapter 1: Introduction.....6

Chapter 2: A Description of Data.....10

Chapter 3: Calculations from Spectra.....67

Chapter 4: Theoretical Calculations.....89

Chapter 5: Summary and Conclusions.....113

References.....115

LIST OF TABLES AND FIGURES

TABLES

		Page
I	Usable Array-2 Data	14
II	Coherences	71-2
III	Periods and Wavelengths of Topographic Waves	105-6
IV	Energy in the Topographic Wave Band	110

FIGURES

1	Array-2 Topography	12
2,3	Mooring Configurations	15,16
4,5	Low Passed Velocity Data	18,19
6-9	Vertical Structure of Low Passed Velocity	24-27
10	Horizontal Velocity Vectors	29
11-13	Progressive Vector Diagrams	31-5
14-29	Horizontal Kinetic Energy Spectra	37-52
30-32	Temperature Data Plots	56-8
33-35	Temperature Power Density	60,62
36	Temperature Spectra Comparisons	64
37-39	Coherence vs. Horizontal Separation	74-5,77
40-45	Coherence Maps	80-87
46-47	Fourier Coefficients in 5-15 Day Band	94-5
48	Theoretical Vertical Energy Trapping	109

CHAPTER I.--INTRODUCTION

Until the 1959 Aries measurements of Swallow (1971) and Crease (1962), the deep ocean was considered to be relatively quiet. Sverdrup (1947) described the overall dynamics of the ocean interior as a balance between the meridional transport and the curl of the wind stress, implying mean horizontal velocities of much less than one centimeter per second. The Aries measurements revealed the existence of dynamical processes in the deep ocean with r.m.s. speeds several orders of magnitude greater than those predicted by Sverdrup. These eddy motions were transient with periods of several weeks, and they were so large and energetic that it was difficult to imagine them decoupled from the slower climatological mean. In addition, the motions were depth dependent, and speeds seemed to actually increase in deep water. Numerous hydrographic stations showed the motions to be nearly geostrophic.

Several investigators attempted to explain these phenomena. Longuet-Higgins (1965), using a flat, homogeneous model ocean, suggested that these motions might be wind generated planetary waves. Later Phillips (1966) decomposed the Aries data into two modes of oscillation, a barotropic and a baroclinic, and showed that 78% of the kinetic energy in the Aries data was in the barotropic

mode, based on this model. Using linear theory he could explain the frequencies and wavenumbers estimated from the Aries data as planetary waves forced by the wind. His theory failed to explain the large amplitudes seen in the measurements, however, and he thus assumed that nonlinearities were inevitably important in the dynamics of these motions, possibly through nonlinear interactions with the Gulf Stream.

Later Rhines (1971 a,b) found that the presence of a simply sloping bottom could account for the apparent bottom intensification present in the Aries data, though he did not account for generation mechanisms for such waves. Schulman (1970) showed that the baroclinic instability of the climatological mean circulation could possibly account for such eddy processes.

To further study the dynamics of these mid-ocean processes, the Mid-Ocean Dynamics Experiment (MODE) was conceived in 1970 as part of the International Decade of Ocean Exploration. The experiment was planned as an in depth study of these eddy motions in a two degree square of the North Atlantic. It was the objective of MODE to map the velocity and temperature fields for a four month period in this area using moored current meters and temperature recorders, Swallow floats, hydrographic stations, plus several new forms of instrumentation. The experiment had several objectives, including testing the geostrophic

relation, testing the conservation of potential vorticity, testing the effects of bottom roughness features on the mid-ocean flow, and comparing Lagrangian and Eulerian scales of motion. Ultimately it was hoped to study the relationship of these transient eddies to the long term climatological mean flow. The experiment was planned for the spring of 1973.

In planning for this large experiment, known as MODE-I, three smaller current meter arrays, collectively known as MODE-0, were deployed as a preliminary test of the mid-ocean environment. Known as Array-1, Array-2, and Array-3, these three current meter arrays served to define the scales of interest for the larger experiment as well as to study the engineering problems encountered in working in the mid-ocean environment.

Array-1 consisted of eight moorings set on a smooth area in the North Atlantic centered nominally on 28°N 70°W. The instruments were put out in November, 1971 and recovered in March, 1972. A detailed hydrographic survey was done in conjunction with Array-1. Array-2 consisted of six moorings set on a rough area 75 kilometers east of the Array-1 site; this array was set in March, 1972 and recovered in May, 1972. Array-3 was a larger scale array made up of six moorings set near the Array-1 area. No quantity of hydrographic data was taken to accompany Arrays-2 and 3.

All three arrays revealed the presence of mesoscale (hundreds of kilometers), long period (tens of days) phenomena which seemed to be similar to the Aries observations. There were some striking differences in the results from the three arrays, however, and the most obvious differences seemed related to the differing forms of the bottom topography at the three array sites. The results from Arrays-1 and 3, on smooth topography, have been discussed by Gould, Schmitz, and Wunsch (1974) (hereafter GSW) and are quite distinct from the measurements made on the rough bottom of Array-2. These Array-2 measurements will be the subject of this work.

This paper will proceed as follows: in Chapter 2 the data from MODE-0 Array-2 will be presented in the form of component plots, progressive vector diagrams, and kinetic energy spectra. Effects of local topography will be noted. In Chapter 3 the data will be examined more closely, and coherences between velocity components at various positions in the array will be interpreted. In Chapter 4 several theoretical explanations for phenomena present in the data will be pursued, and conclusions will be presented in Chapter 5.

CHAPTER 2--A DESCRIPTION OF ARRAY-2 DATA

Location

The configuration of Array-2 is shown with the associated bottom topography in Figure 1. The center of Array-2, mooring 433, is located approximately 100 kilometers to the east of where Array-1 had been located. The local topography consists of generally rolling hills of height less than 300 meters superimposed on an area of nominal depth 5300 meters. Running through the area at an angle approximately 15 degrees from north is a chain of seamounts of amplitude 400 to 600 meters. 75 kilometers to the west of the array center lies the abyssal plain, and 50 kilometers to the east there are seamounts with amplitudes of 400 meters. 50 kilometers to the southeast there exists an area of larger seamounts with amplitudes of up to 1000 meters. We are thus looking at an area with many scales of bottom roughness, including relatively flat areas, rolling hills, and seamounts. This type of bottom topography is common in the Sargasso Sea and is much more representative of the bottom topography of the North Atlantic than is the smooth area in the vicinity of Array-1.

Instrumentation

The moorings of Array-2 were deployed in a cross type

pattern shown in Figure 1. Mooring 424, instrumented with Geodyne 850 current meters at depths of 1500, 4000, and 5000 meters, was set as part of a program of site moorings of the Woods Hole Oceanographic Institution on February 10, 1972. The other moorings were set on R.V. Chain cruise 63 between March 18, 1972 and March 22, 1972, and these moorings were instrumented with Vector Averaging Current Meters (VACM's) at depths of 1500 meters and 4000 meters. In addition, mooring 430 was also instrumented at 5000 m. Gould (1972a) has discussed the individual characteristics of different types of moored current meters.

Mooring 424 was set using a toroidal buoy at the surface. The other instruments were all set on subsurface moorings with a buoyant float approximately 300 meters below the surface. Recently several investigators, notably Gould (1972b), have discussed the problem of making deep sea measurements of low frequency currents from surface moorings. Gould finds that the most obvious effect of the surface buoy is to increase the kinetic energy spectrum by a factor of five to ten over that expected from a current meter on a subsurface mooring in the same place at the same depth. It is true that horizontal velocity components measured from current meters on surface moorings are generally larger by a factor of two or three than those measured from subsurface

FIGURE 1

Array-2 Bottom Topography

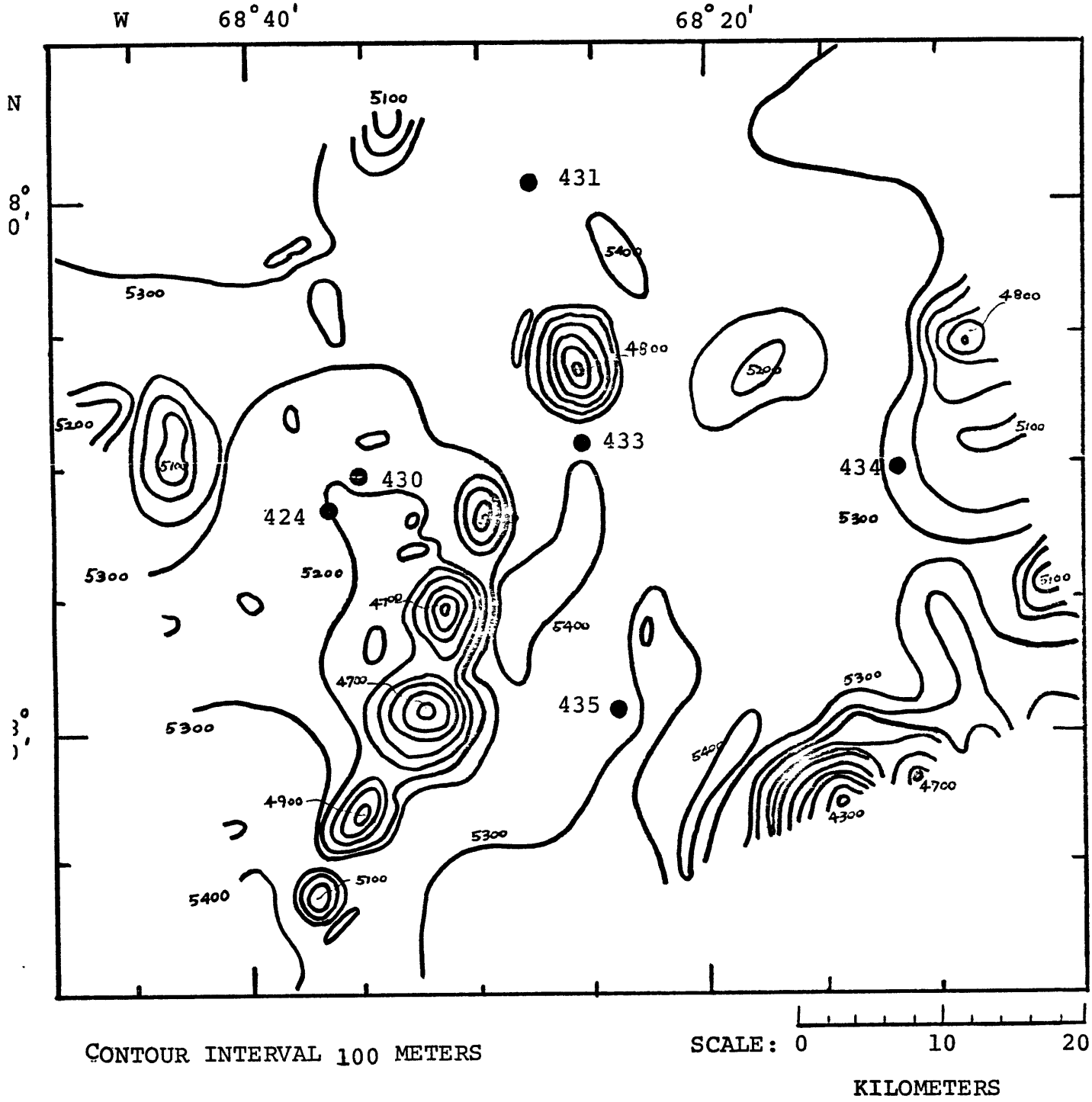

moorings at the same depth. This added energy is possibly related to vertical pumping of the current meter through the action of surface waves. Surface and subsurface mooring configurations are shown in Figures 2 and 3, which have been reproduced from Fofonoff and Webster (1971).

Velocity Data

A. Velocity Components

After processing the data tapes from all of the current meters, it was found that only one current meter at 1500 m., 4242, operated properly (the Woods Hole convention for naming moored instruments is to give the mooring number, 424 in this case, followed by the sequential position in the mooring line counting from the surface, 2 in this case). All current meters at 4000 m. operated for at least 38 days, with the exception of the VACM 4354. Both deep instruments at 5000 m. operated properly for the duration of the experiment. A table of usable data obtained from the experiment is given in Table I.

Geodyne 850 type current meters generally are set to take and store a burst of samples once every 15 minutes in a method described by Webster (1967). The newer VACM's do not store all of these samples, but average them so that only one value of compass, vane, and rotor count is recorded every 16 minutes. This

TABLE I.

Usable Data from MODE-0 Array-2

Instrument	Time Start (GMT)	Time Stop (GMT)
4242	II-7-72	V-25-72
4243	II-7-72	IV-24-72
4244	II-7-72	V-25-72
4301	III-21-72	V-25-72
4302	III-21-72	V-25-72
4312	III-21-72	V-26-72
4332	III-21-72	V-1-72
4342	III-21-72	V-26-72
4354	III-24-72	V-26-72

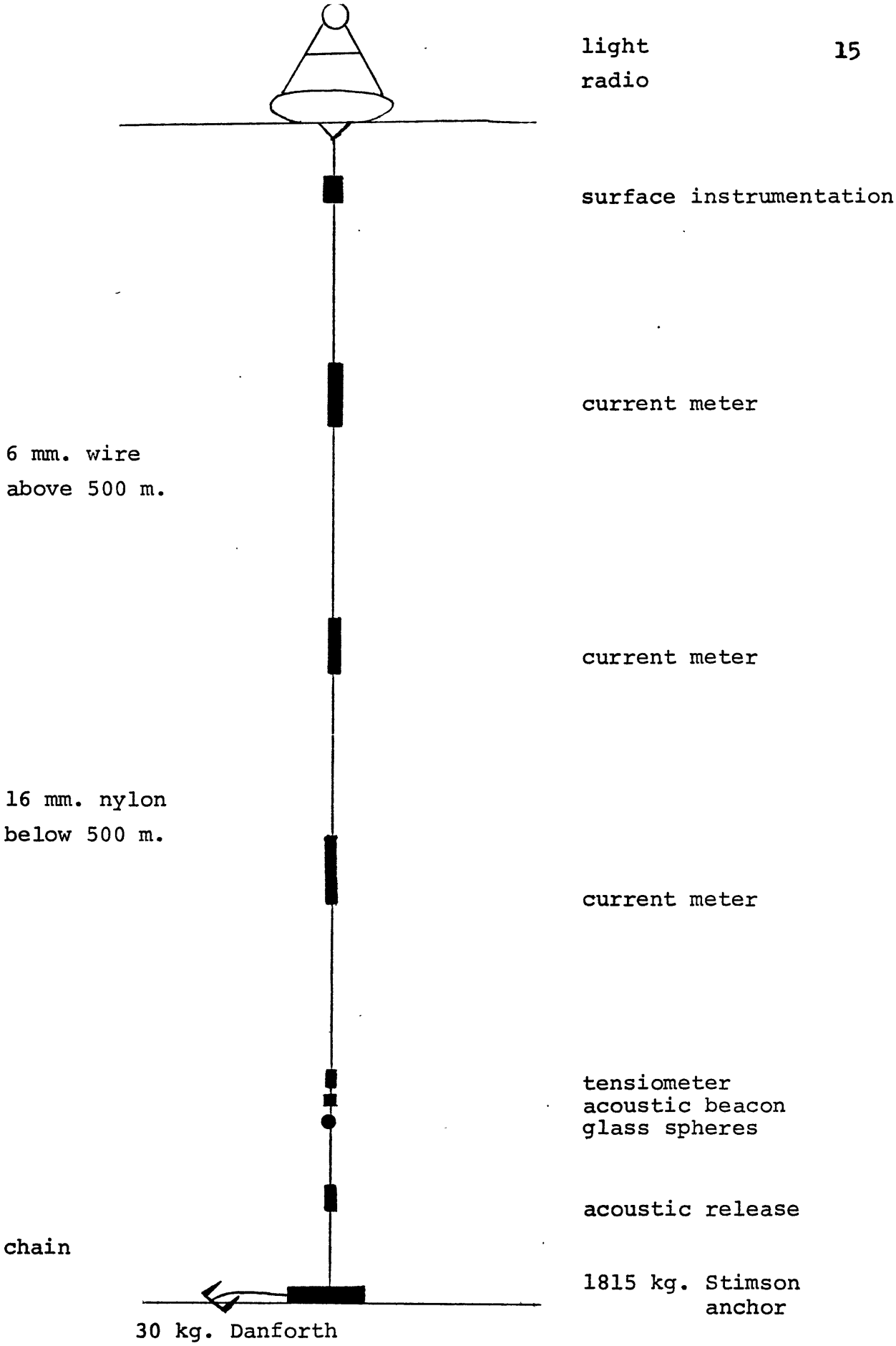

FIGURE 2
A surface mooring

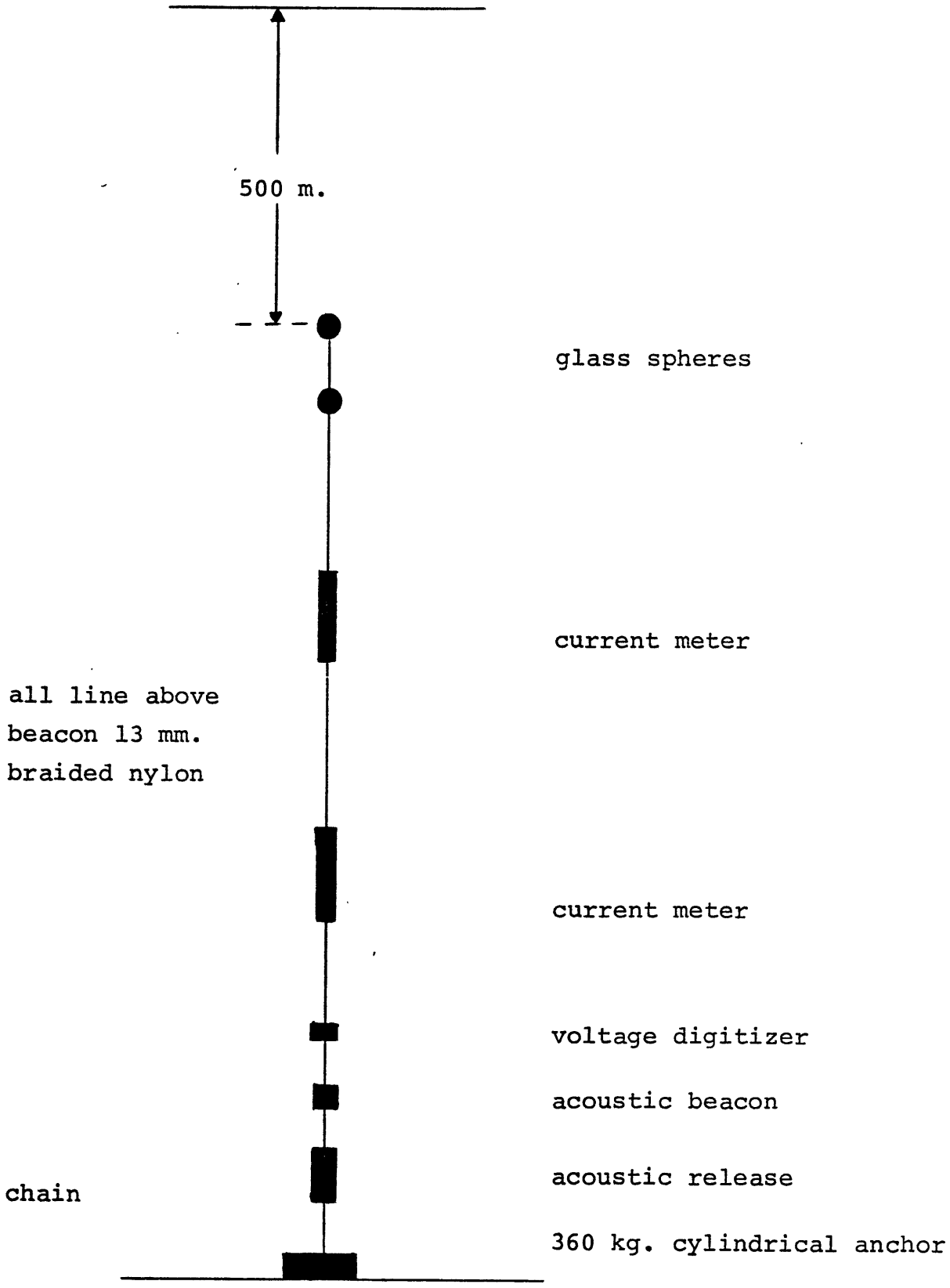

FIGURE 3
A subsurface mooring

sampling scheme provides a compromise between the twin constraints of aliasing due to high frequency surface wave action and the data storage capacity of the instrument. For the purposes of this work we are interested only in the low frequency portion of the signal. Thus the data have been low passed using a Gaussian filter described by Schmitz (1972a). The filter is designed so that 90% of the signal amplitude in periods of less than two days is removed. The data is averaged after low passing to give one sample per day. These low passed daily averages given by Schmitz (1972b) are shown in Figures 4 and 5.

We note first the tendency for the north components (v's) to have higher amplitudes than the east components (u's). This is generally true in all the records to varying degrees, and may be related to the anisotropic structure of the bottom. Overall for Array-2, $\overline{u^2}/\overline{v^2}$ has been calculated to be .30. For all of the data from 4000 m. depth from Array-1 and Array-3 on the smooth area, $\overline{u^2}/\overline{v^2}$ was found to be 1.0. Thus the bottom topography may be influencing the Array-2 flow. This aspect of the data will be explored further in later chapters.

In most of the measurements the duration of the experiment was too short to truly define a characteristic time scale. On current meter 4312 in the north components, speed begins to increase positively around March 20;

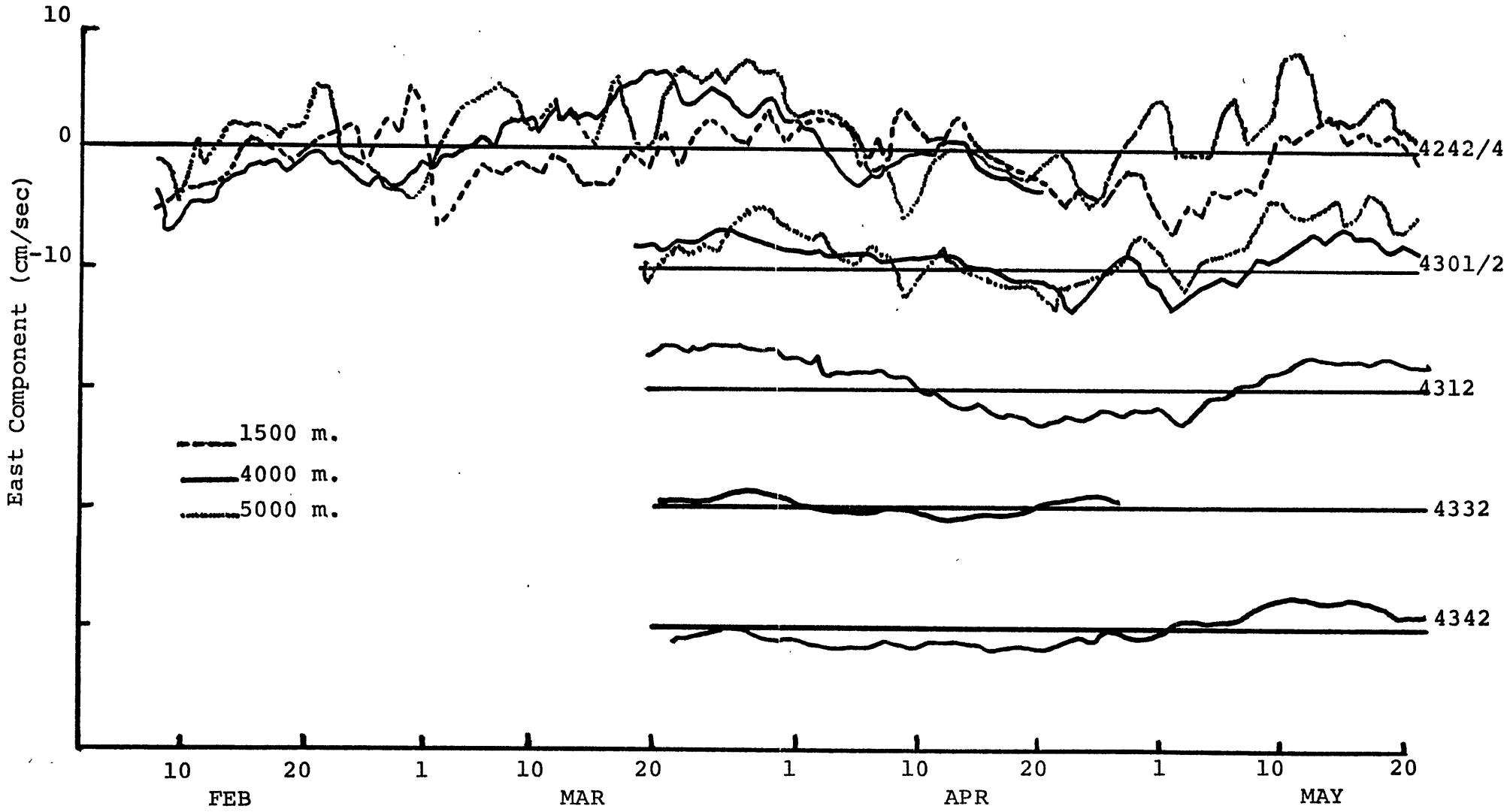

FIGURE 4
(from Schmitz)

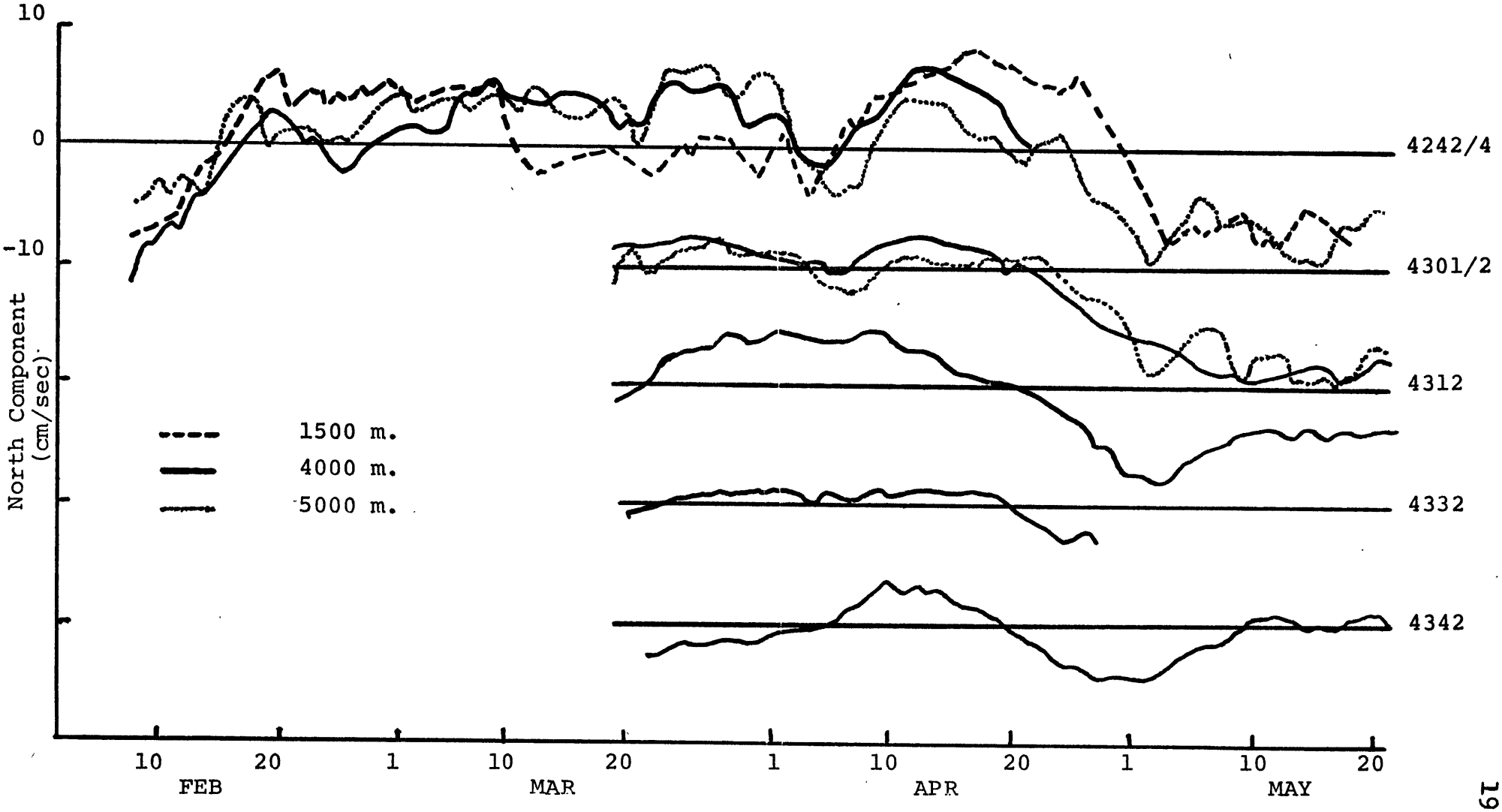

FIGURE 5

(from Schmitz)

the speed reaches a maximum around April 5, and falls back to zero on April 20. The speed then begins to increase negatively (to the south). It reaches a maximum negative value on May 1 and appears to be slowing back to zero on May 20 when the instrument is recovered. In the east component we note a similar oscillation shifted in phase by about 10 days. This indicates apparent periods of slightly greater than 60 days. Periods of the order of 60 to 80 days were also identified by GSW as typical periods in the other MODE-0 experiments.

Several other phenomena are evident when viewing the velocity components. We note the small amplitude of the motion at current meter 4332. This instrument failed on April 27 after 38 days of operation. The data suggests that very little motion was occurring at 4332 compared to the other instruments, and for the entire 38 days the current speed barely rose above 3 cm/sec in the north component and 1.5 cm/sec in the east. A possible clue to the cause of this comes to mind when we refer back to Figure 1. We note that mooring 433 is located very near a seamount. Since the overall flow is primarily north-south, the presence of this seamount may have the effect of sheltering instrument 4332 from the flow. In a numerical simulation, Bryan (1973) has verified that an instrument in the position of current meter 4332 would measure a

smaller current than other instruments in the area due to the presence of the seamount. Bryan's model used actual bottom topography from the Array-2 area.

Another striking feature of the data is the persistent high speed in the north components of the instruments on moorings 424 and 430. For the final month of the experiment a strong southward current of nearly 10 cm/sec is evident which shows little tendency of subsiding at the end of the record. From April 20 to May 20, these instruments show a collective mean speed of 7.4 cm/sec to the south. While the north components of these instruments were very different from the north components of the other instruments, the east components show little variation from the east components at other instruments. Looking again at Figure 1, we see that moorings 424 and 430 are located to the west of the seamount chain, while the other moorings are to the east of it. The ridge may be influencing the flow. We note, however, that all current meters on mooring 424 show this trend to the south, including 4242 at 1500 m. This current meter is more than 3500 m. above the highest topographic feature in the area, so if in fact the local topography is influencing the flow, its effects are being felt high in the water column. Instrument 4312 shows a moderate 20 day increase in speed in a southerly direction between

April 20 and May 10, so this strong flow to the south may also be present further to the north for a short time. Near moorings 424 and 430, however, the effects are very much amplified and do not relax by the end of the experiment as they seem to at 431.

A third feature of the data is evident in the 5000 m. deep records from current meters 4244 and 4302. While at each instrument the motion in both components generally tracks the motion of the instruments higher on the mooring, we see some additional effects of somewhat shorter period (5-15 days) superimposed on the longer period variations. Though for the long term variations the velocities along depth contours (north components) are more energetic than those across depth contours (east components), the opposite seems true for these shorter period motions. In the last two months of record 4244 these oscillations are very obvious in the east component and to a lesser extent in the north component. Generally, the same is true for current meter 4302 during the same interval of time, though the oscillations are less energetic. Another look at the topographic chart may help to clarify this. Since these current meters are actually deeper than the peaks of the highest topographic features in this area, we may be seeing the effects of processes which do not occur higher up in the water column; these may be bottom trapped effects.

B. Vertical Structure

We can examine more closely the vertical structure of the horizontal velocity field. Figures 6 through 9 show plots of five day averages of low passed velocity from 1500 to 5000 m. on mooring 424, a surface mooring. We note that there are obvious vertical shears in the velocity field for most of the 100 days of the experiment, with large intermittent shears between 4000 and 5000 m. These shears are especially striking during days 40 through 75. During this period there is a shear of approximately 3 cm/sec between 1500 and 4000 m. Between 4000 and 5000 m. there are shears as high as 4.5 cm/sec (days 50-60). Thus during this time $\frac{\Delta V}{\Delta z}$ between 1500 and 4000 m. is 1.2×10^{-3} cm/sec-m and between 4000 and 5000 m. $\frac{\Delta V}{\Delta z}$ is 4.5×10^{-3} cm/sec-m; this is a shear about four times as high at great depth. This shear corresponds to the period of high activity in the east components of 4244 shown in Figure 4. By days 76-100 the situation has changed. At first the velocities have adjusted so as to create a mean shear in the north components of 7 cm/sec ($\frac{\Delta V}{\Delta z} = 2 \times 10^{-3}$ cm/sec-m) over the whole column. By day 91 the north-south velocity field in the column is almost homogeneous from 1500 to 5000 m. This corresponds to the southward trend in the velocity field seen near the end of the experiment at all depths.

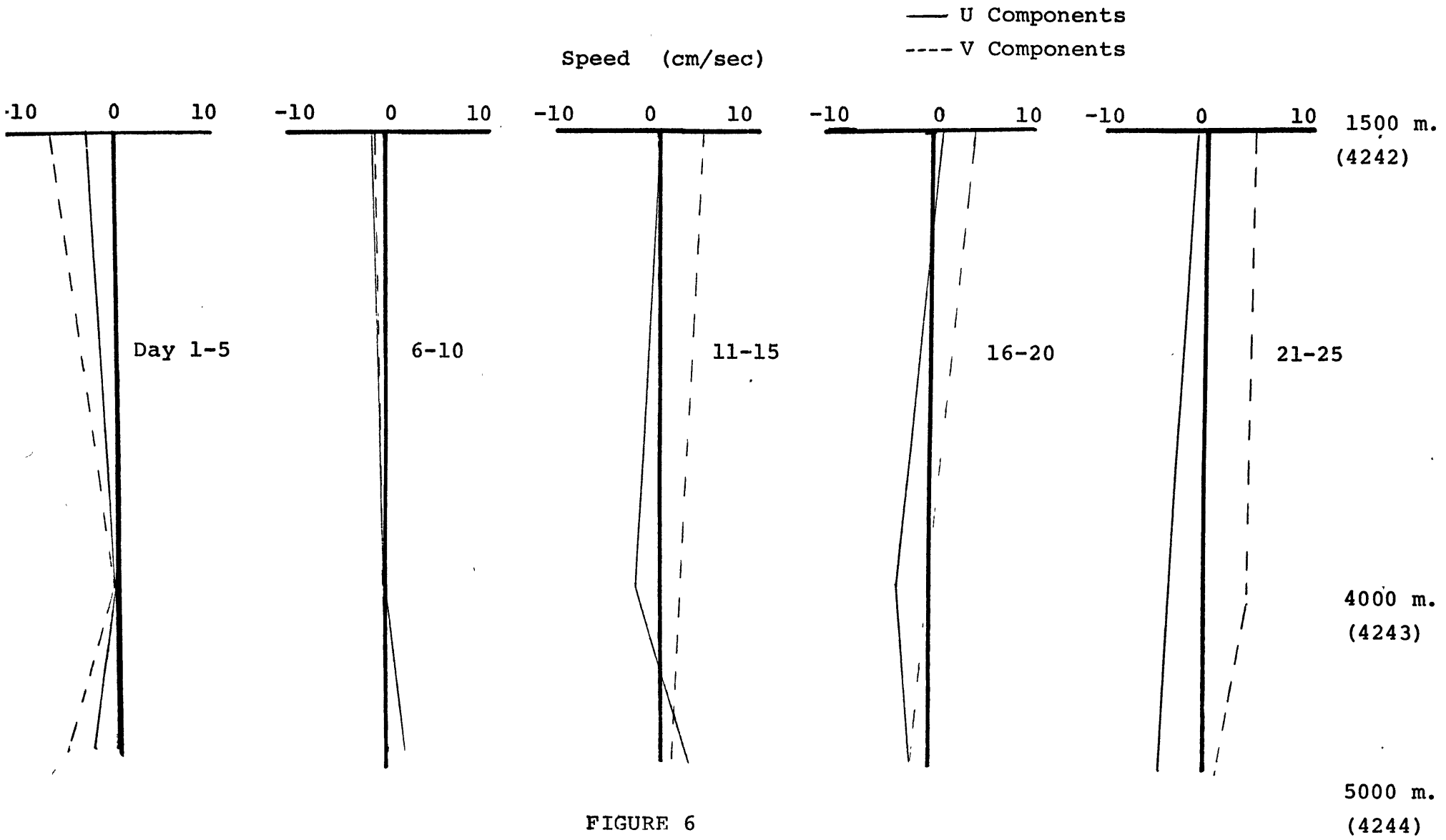
—— U Components
---- V Components
Speed (cm/sec)
-10
0
10
Day 1-5
6-10
11-15
16-20
21-25
1500 m.
(4242)
4000 m.
(4243)
5000 m.
(4244)

FIGURE 6

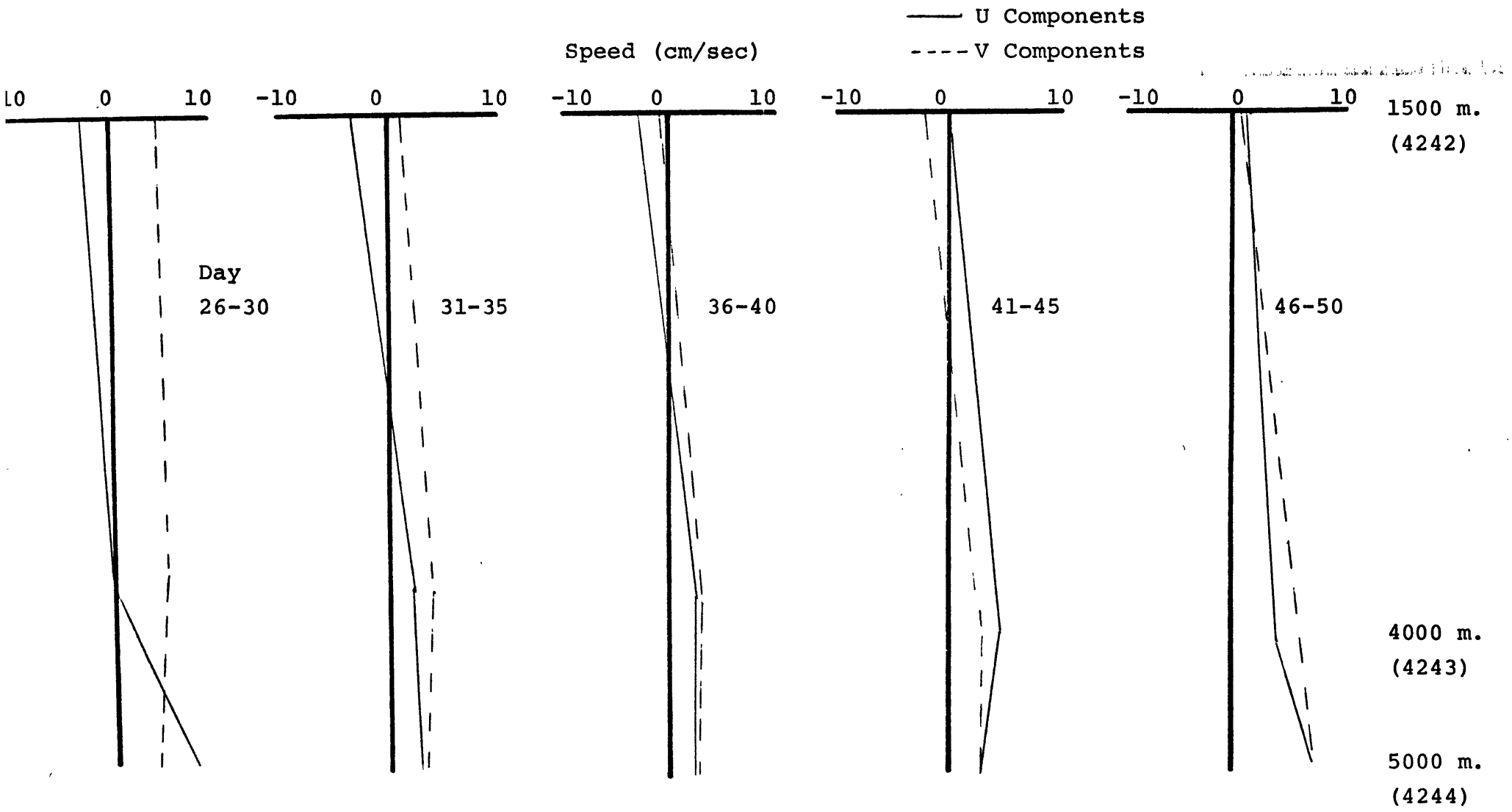
U Components
V Components
Speed (cm/sec)
-10 0 10
Day
26-30
31-35
36-40
41-45
46-50
1500 m.
(4242)
4000 m.
(4243)
5000 m.
(4244)

FIGURE 7

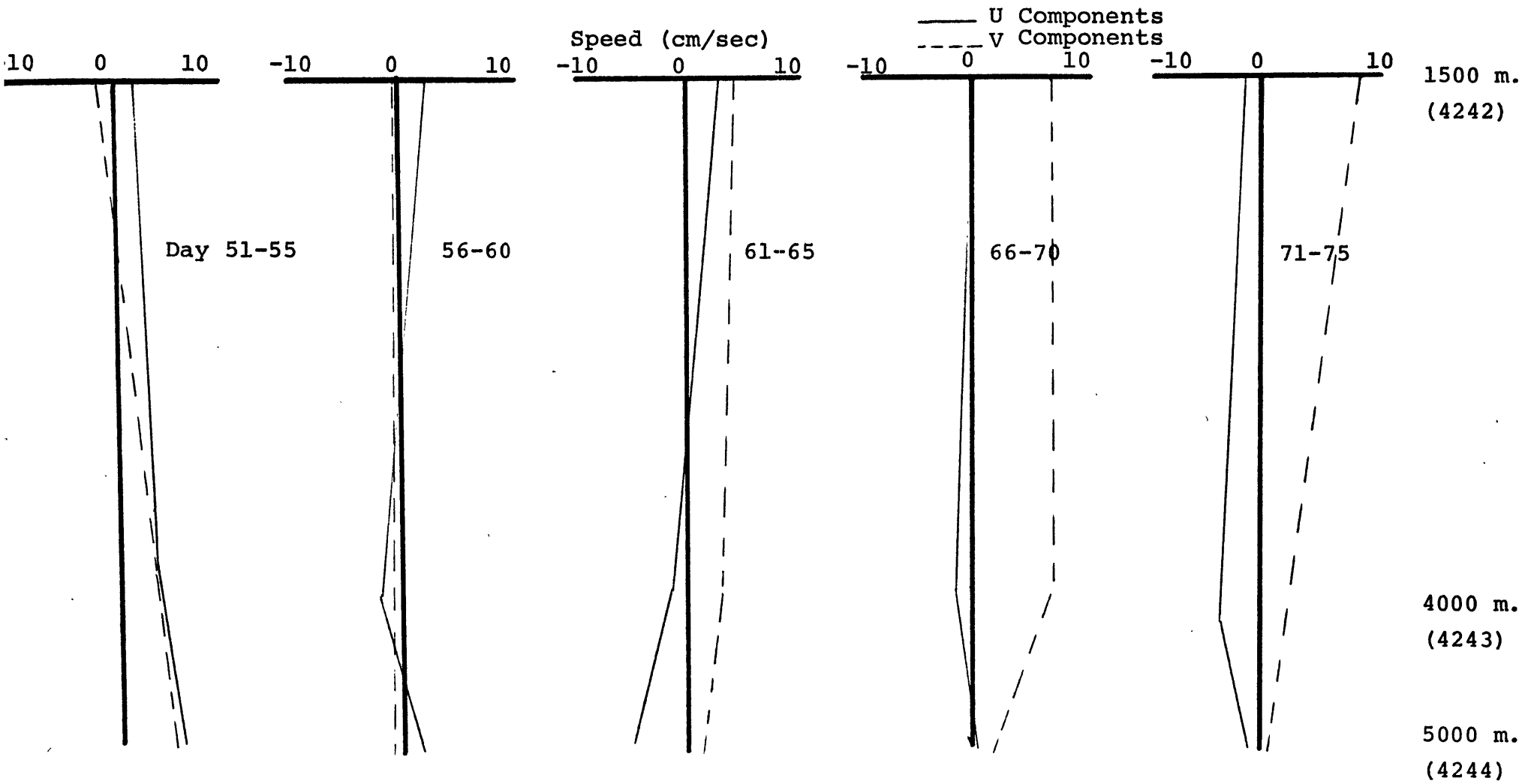
Speed (cm/sec)
U Components
V Components
-10 0 10
Day 51-55
56-60
61-65
66-70
71-75
1500 m.
(4242)
4000 m.
(4243)
5000 m.
(4244)

FIGURE 8

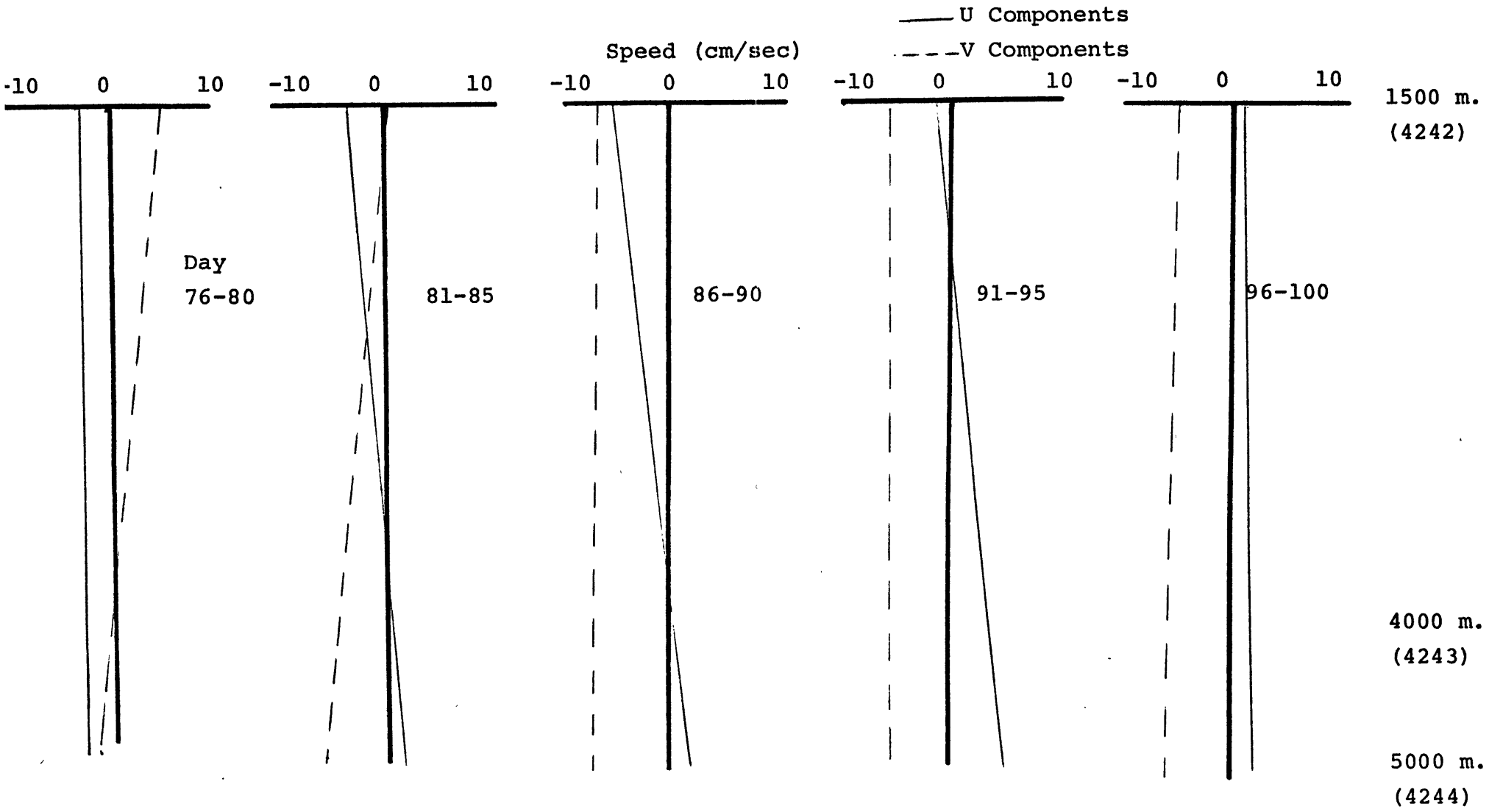

FIGURE 9

(Data at 4000 m. taken from 4301, 4 km. to the northeast, for Days 76-80)

Stommel (1972) has constructed similar plots from low passed Array-1 data. Of course, velocity measurements from above the thermocline were available from Array-1. From Stommel's plots the shears between 1500 and 4000 meters ($\lesssim 10^{-3}$ cm/sec-m) were generally smaller on the average than those calculated above. Over the smooth topography of Array-1 there were no 5000 m. measurements so we cannot make a comparison of deep shears.

In Figure 10 horizontal velocity vectors have been plotted for the two month duration of the experiment. Once again, we note the shears between instruments at 1500 and 4000 m. and 4000 and 5000 m. Generally currents at moorings 424 and 430 show the most activity although the current at mooring 431 is very active around May 1, in agreement with the velocity component plots already discussed. We note that at 4000 m. the sense of rotation of velocity vectors is cyclonic at all moorings except 434, where the rotation is anticyclonic until April 21. The short duration of the experiment does not allow us to observe a reversal of rotation over the entire array as was noted in the other MODE-0 experiments.

C. Progressive Vectors

Another way to view the data is with progressive vector diagrams (PVD). The interpretation of these is simple: if u is the east velocity component and v the

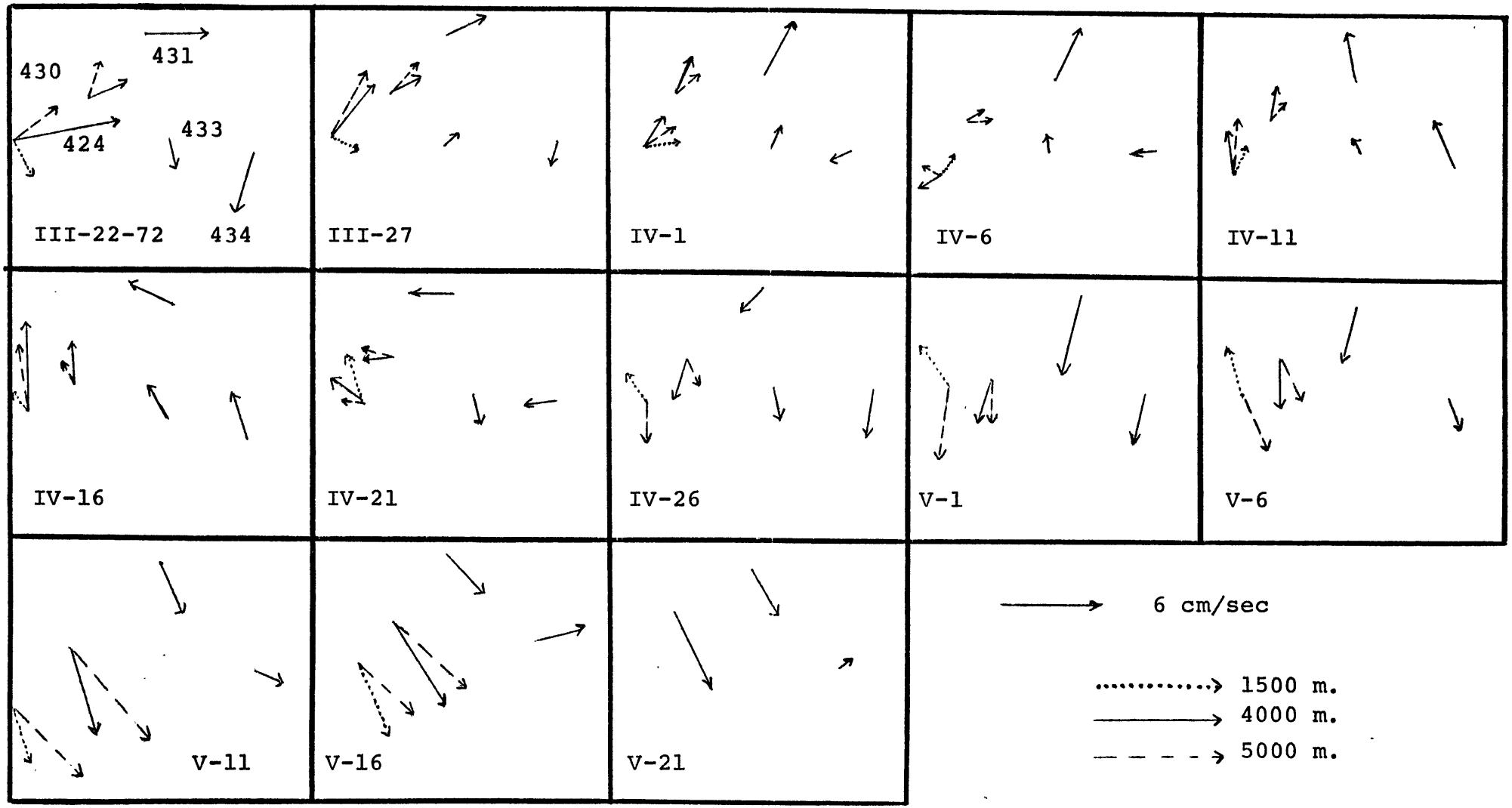
430
431
433
424
434
III-22-72
III-27
IV-1
IV-6
IV-11
IV-16
IV-21
IV-26
V-1
V-6
V-11
V-16
V-21
6 cm/sec
1500 m.
4000 m.
5000 m.

FIGURE 10

north, then $\underset{\sim}{u} = (u,v)$ is the velocity vector. The progressive vector diagram is constructed by integrating with time:

$$PVD = \int_{t_o}^{t_o+T} \underset{\sim}{u}(t)\,dt$$

where T is the duration of the record in time. A spatial scale is thus associated with a PVD. However, this must not be interpreted as the actual motion of a single particle. The diagram only represents the instantaneous motion of particles at the instrument.

Progressive vector diagrams for the current meters of Array-2 are shown in Figures 11 and 12. Because the current meters on mooring 424 were set one month before the others, arrows have been drawn on 4242, 4243, and 4244 to indicate the time origin of the other instruments. We note a southwestward flow until around February 20 on current meter 4242 and February 28 on 4243. The flow then reverses and goes north to northeast for approximately one month. During this month the mean velocity at 4000 m. is approximately twice that at 1500 m., as evidenced by the length of the curve during this time. At 1500 m. the current then enters a month long period of virtually no mean flow on March 4. This is where the PVD's for the other moorings begin. The current emerges from this period of stagnation on April 10, still flowing north. On May 1 it swings around

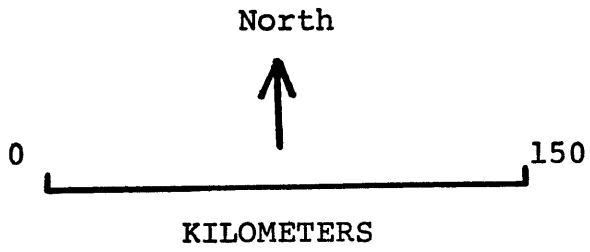

4242
1519 m.
II-7-72 to V-25-72

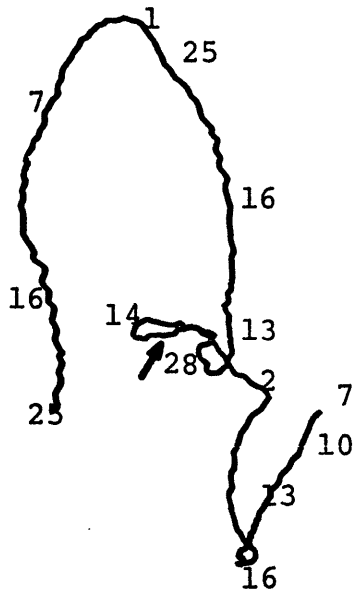

4243
4074 m.
II-7-72 to IV-25-72

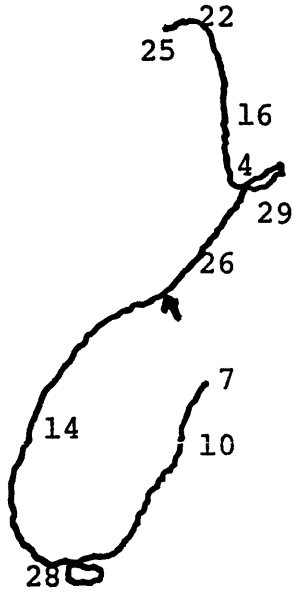

FIGURE 11
(from Schmitz)

4244
5131 m.
II-7-72 to V-25-72

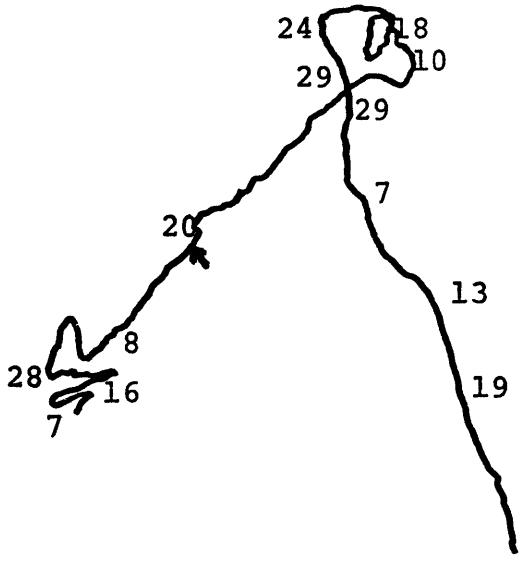

4312
3955 m.
III-19-72 to V-26-72

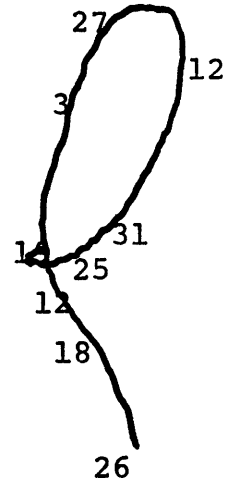

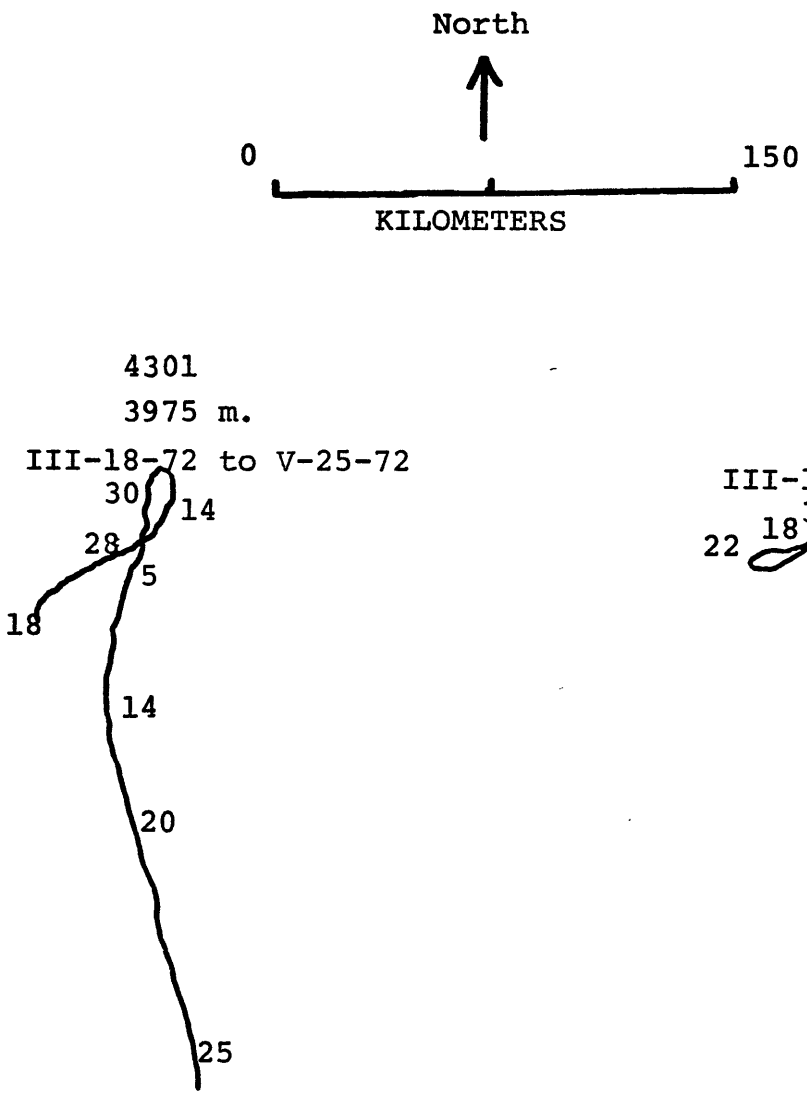

FIGURE 12
(from Schmitz)

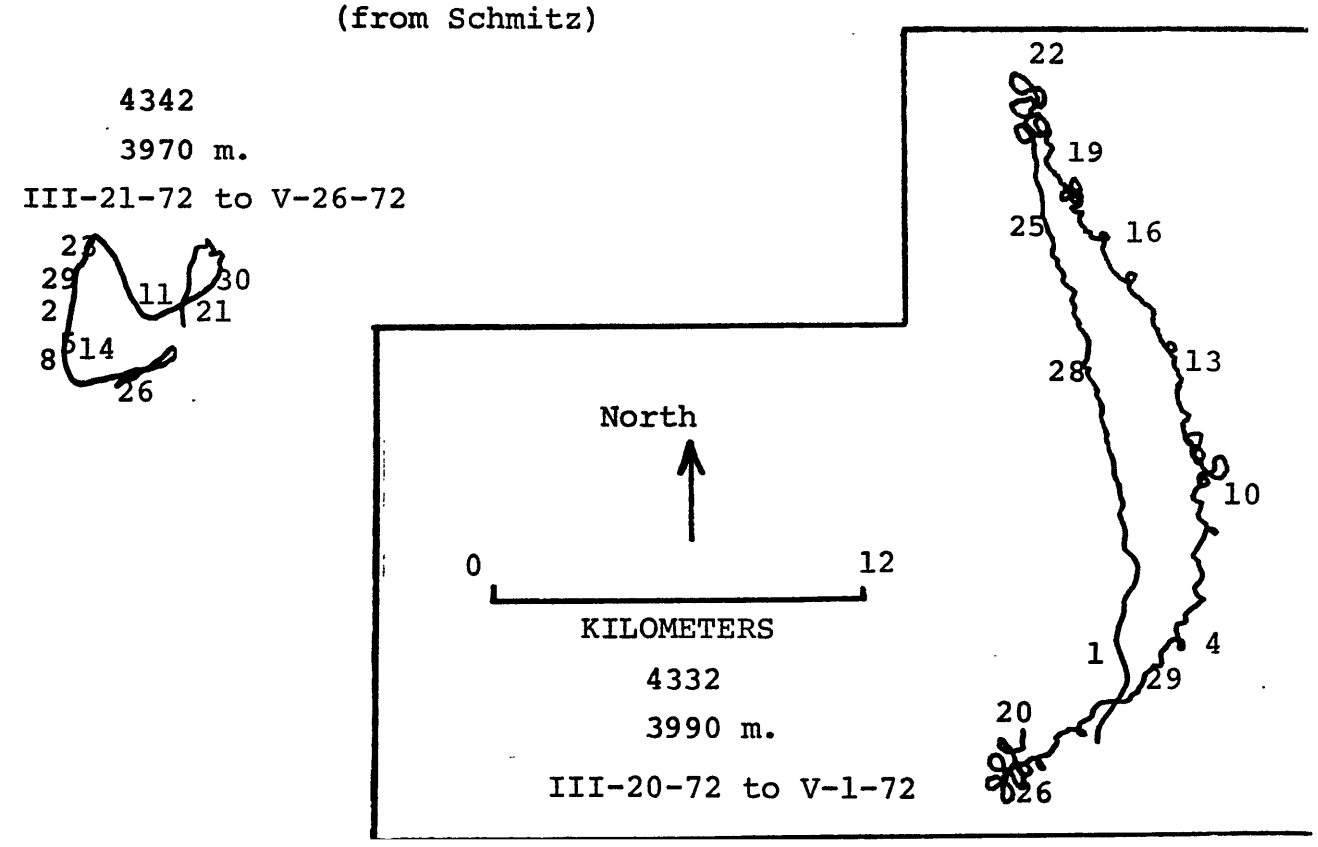

to the south and continues in this direction until May 25 when the instrument is recovered. Current meter 4243 at 4000 m. shows a similar diagram during this time. The current continues to flow north until March 29 when a short, 5 day period of quiescense is noted. The currents then continue north; the instrument fails on April 29.

At 5000 m. the currents are flowing northeast until March 29 when they too enter a month of relative calm. On May 1 the speeds begin to increase again, this time in a southerly direction, and the current continues in this direction till the end of the experiment. Each record of this mooring thus shows a period of relative quiet. A change of current direction follows the calm period at 5000 m. though there is no direction change after the quiet period at 1500 and 4000 m.

The only other measurement of vertical structure available in this experiment is on mooring 430. Mooring 430 shows nearly identical PVD's at 4000 and 5000 m., and both diagrams are very similar to that of 4244 for the two months common to all three records. The PVD from current meter 4312 also looks similar to those previously discussed: there is a general northward flow for one month followed by a flow to the south for the remainder of the experiment. The instruments on the eastern side of the ridge show somewhat different characteristics.

Currents at instrument 4332 show an excursion of only 25 km. for the 38 days that the current meter operated. Of course, during this time period the instruments west of the ridge also showed only small particle displacements, so we cannot conclude on this basis that the character of the motion here is any different than that west of the ridge. Even during this period, however, the velocities at instrument 4332 are smaller than those measured elsewhere in Array-2, as has been previously noted.

Instrument 4342 shows a PVD different than any of the others. There is almost no net displacement over the two months of the experiment, and the scale of motion estimated from the PVD is only of the order of 20 km. The difference may be explained from mooring 434's distance from the ridge. Mooring 434 is located 20 km. east of the array center on a patch of roughness sloping to the east. If local topographic features are important, as they seem to be, then the flow at current meter 4342 may be influenced more by features east of the ridge than by the ridge itself. In a sense, it may be in a different "topographic domain" than the other instruments.

Figure 13 shows progressive vector diagrams for current meters 4533 and 4536. Mooring 453 was set as part of Array-3 in the same location as mooring 424 of Array-2.

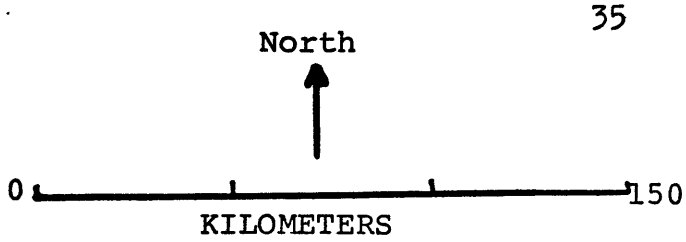

4533
1516 m.
V-26-72 to VII-8-72

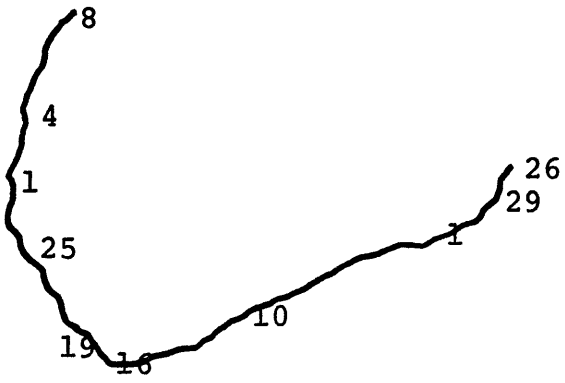

4536
4075 m.
V-26-72 to VII-19-72

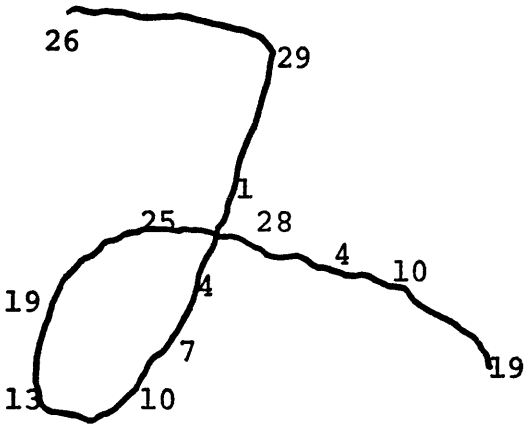

FIGURE 13
(from Schmitz)

We see that when current meter 4242, at 1500 m., was recovered on May 25, the flow was to the southwest. Mooring 453 was set on May 26. The currents at this point in space continued to the southwest until June 16 when the flow changed to the northwest; the flow remained northwest until July 8 when the instrument failed. At 4000 m., the current was just swinging around to the southwest when current meter 4243 failed on April 25. One month later on May 26, when mooring 453 was set, the currents were due east at 4000 m. On May 29 the flow turned south; on June 13 back to the north; on June 29 back to the east until the instrument failed on July 19. This may help to give us some idea of how complicated the currents are in this area. From Array-2 we are led to believe that currents flow mainly along contours of constant depth. However, in the two results from Array-3 that extend our knowledge of the time scales, currents are flowing across contours of constant depth 50% of the time. In addition, the strong similarities noted between flow at 1500 m. and 4000 m. in Array-2 are not evident in 4533 and 4536 from Array-3. We are led to believe that dynamic processes are possibly very complicated and intermittent in this area.

Power density spectra for horizontal velocities from each current meter are presented in Figures 14 through 29. The spectra have been computed using two

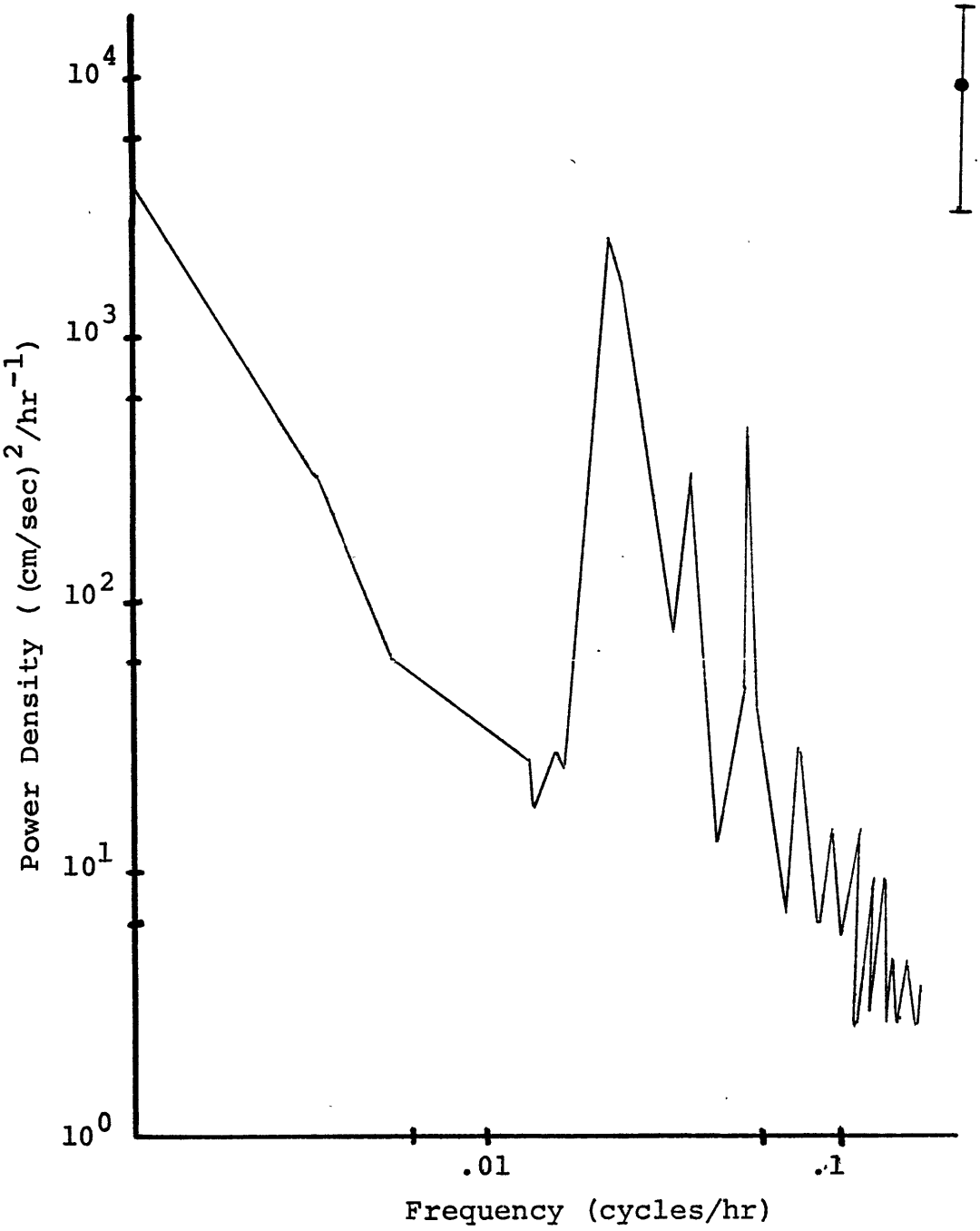

FIGURE 14
4242 U Power Density

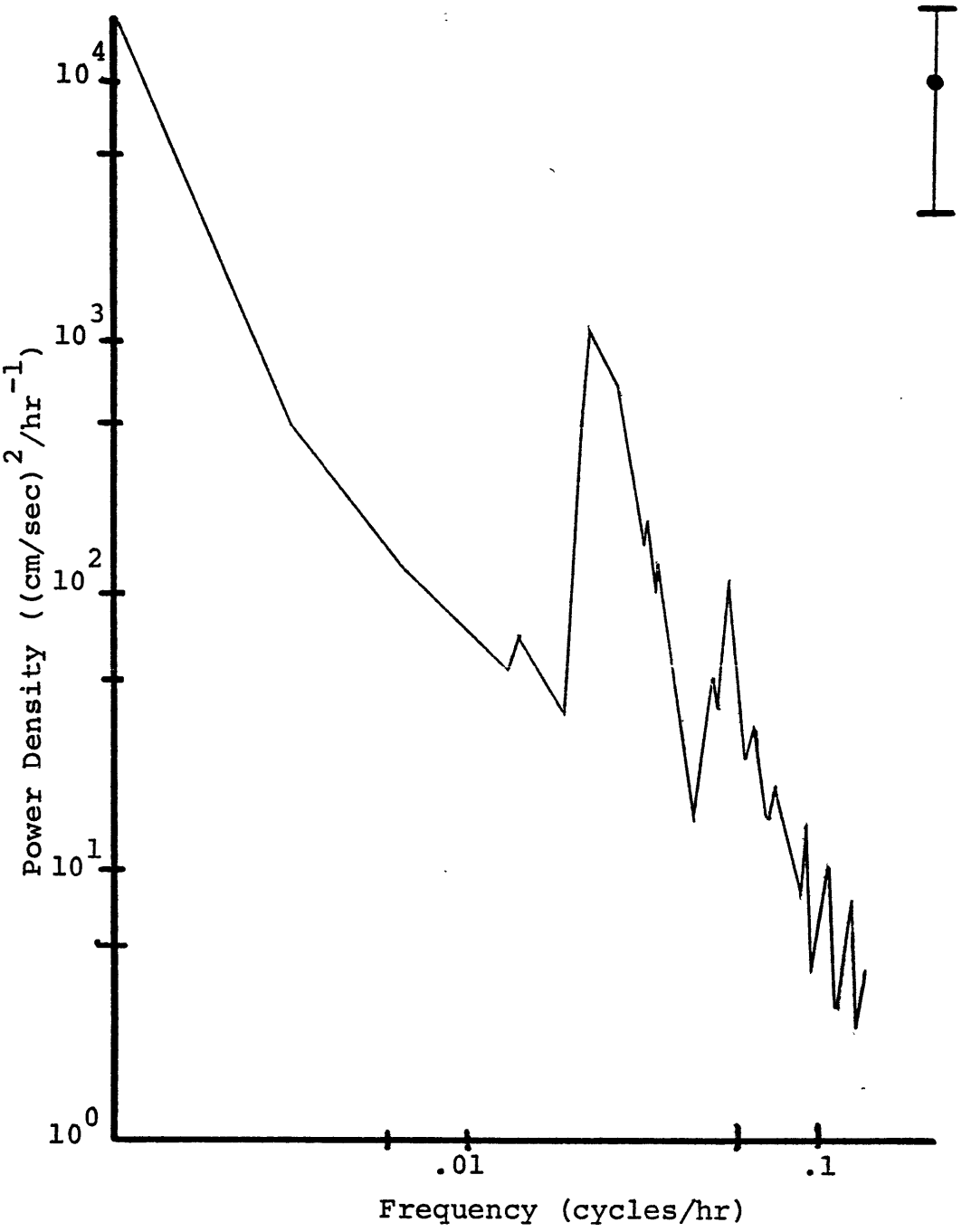

FIGURE 15
4242 V Power Density

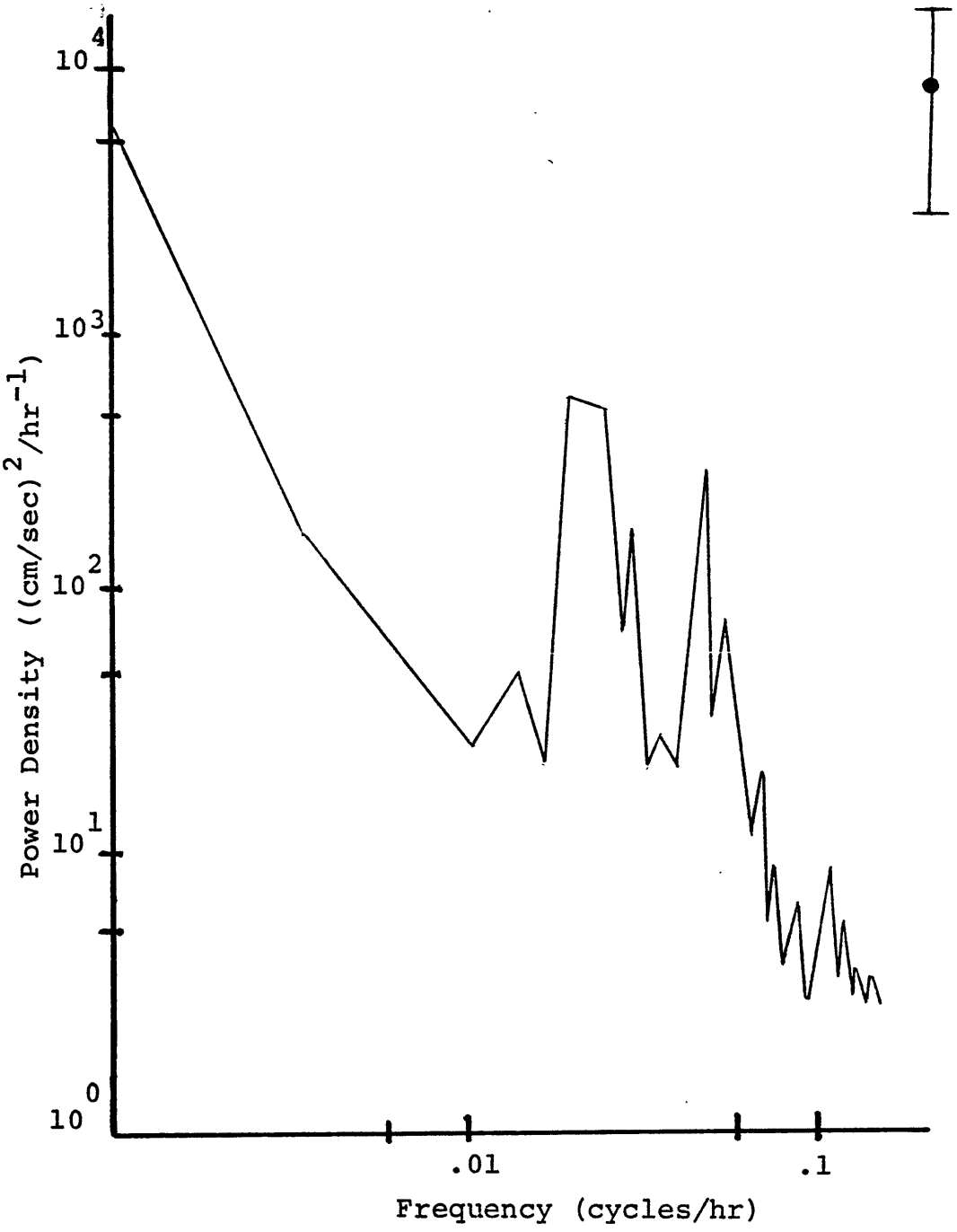

FIGURE 16
4243 U Power Density

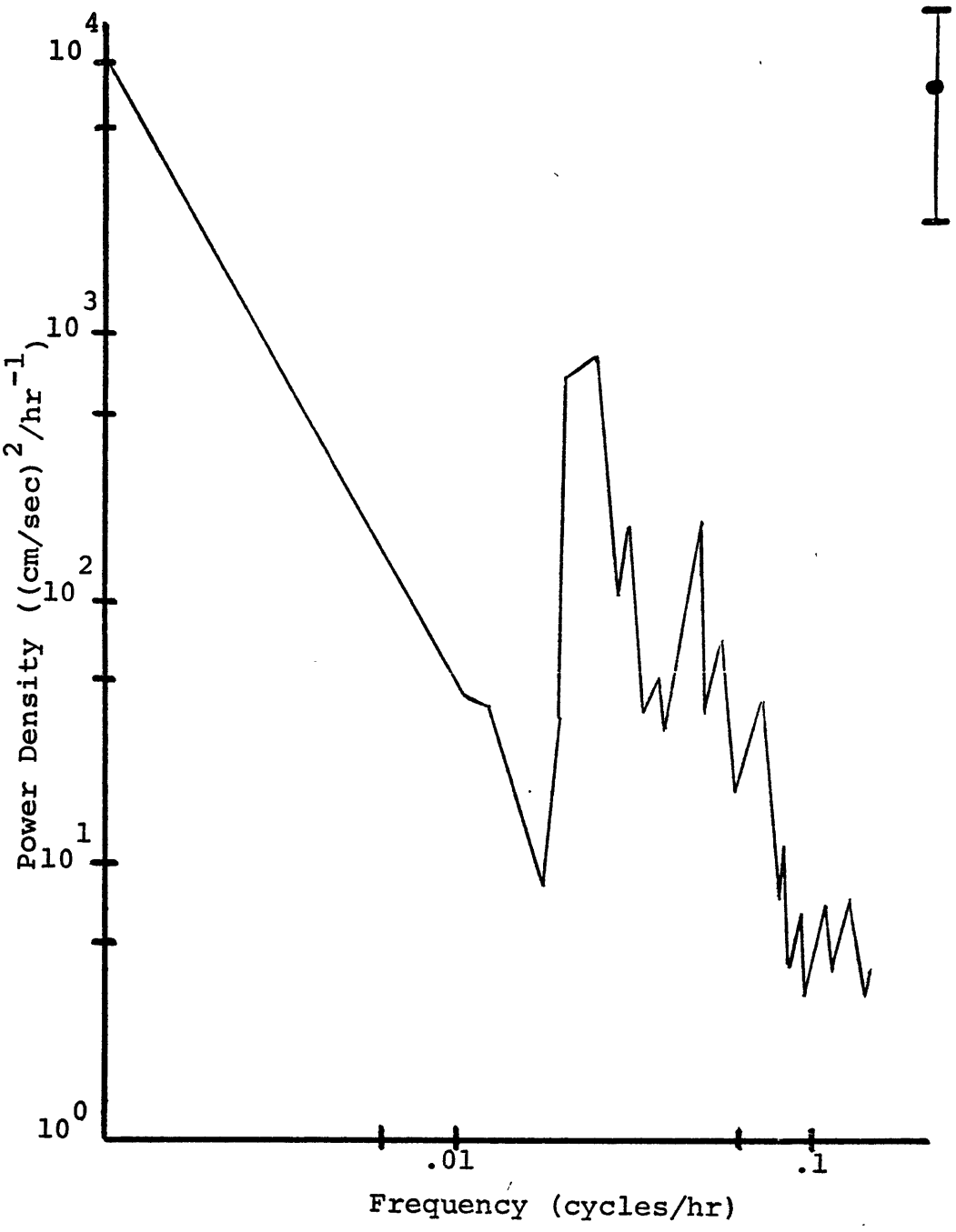

FIGURE 17

4243 V Power Density

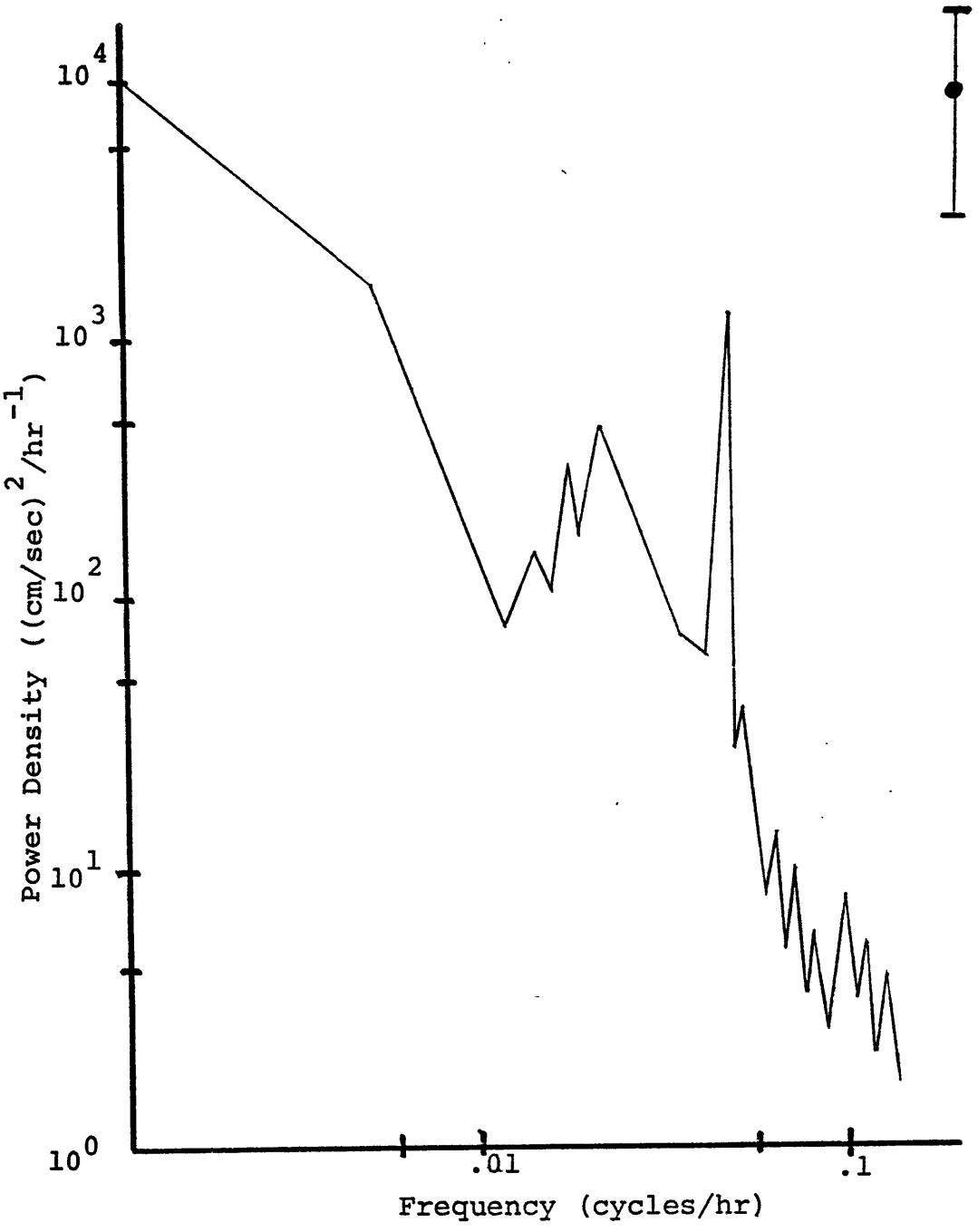

FIGURE 18
4244 U Power Density

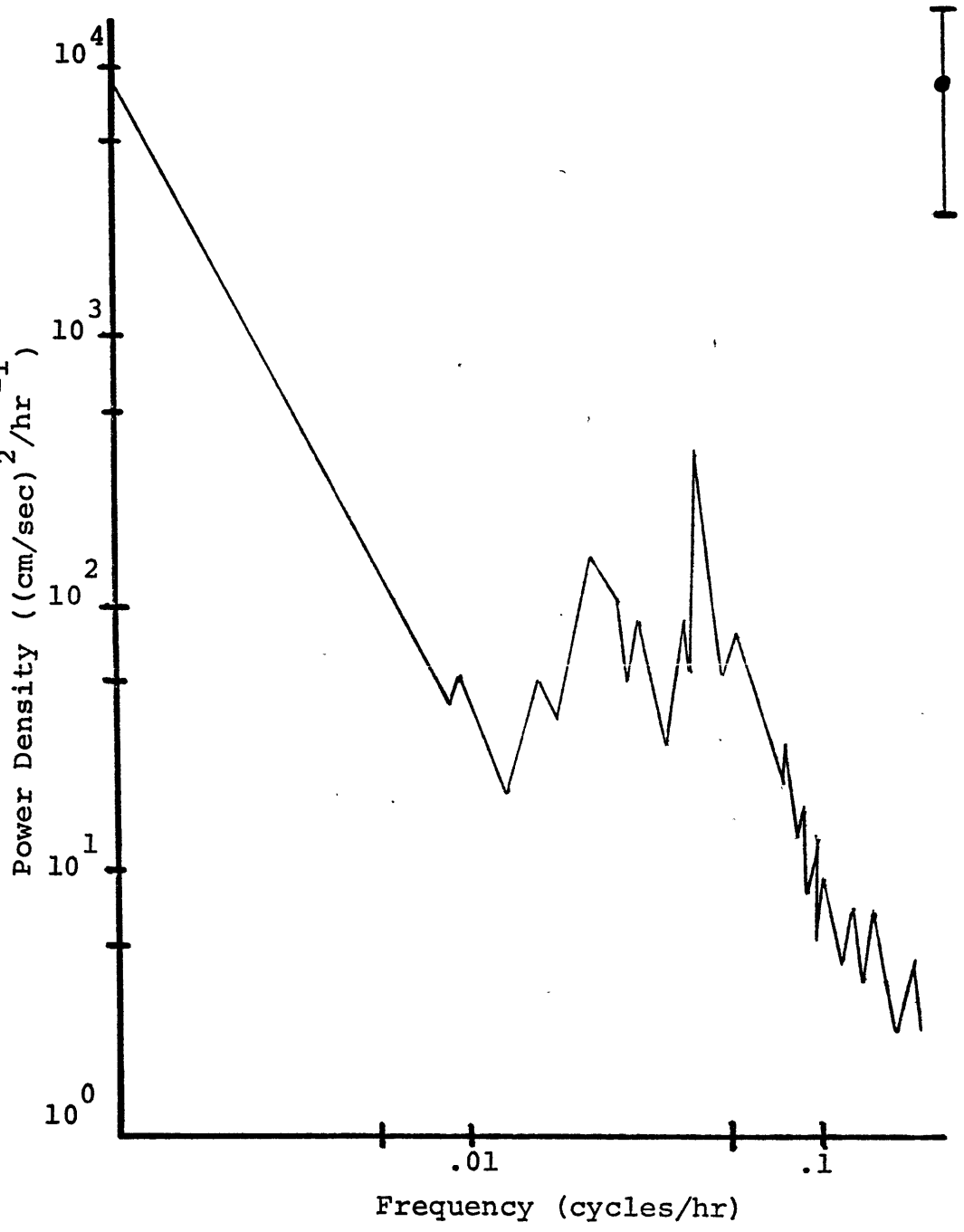

FIGURE 19
4244 V Power Density

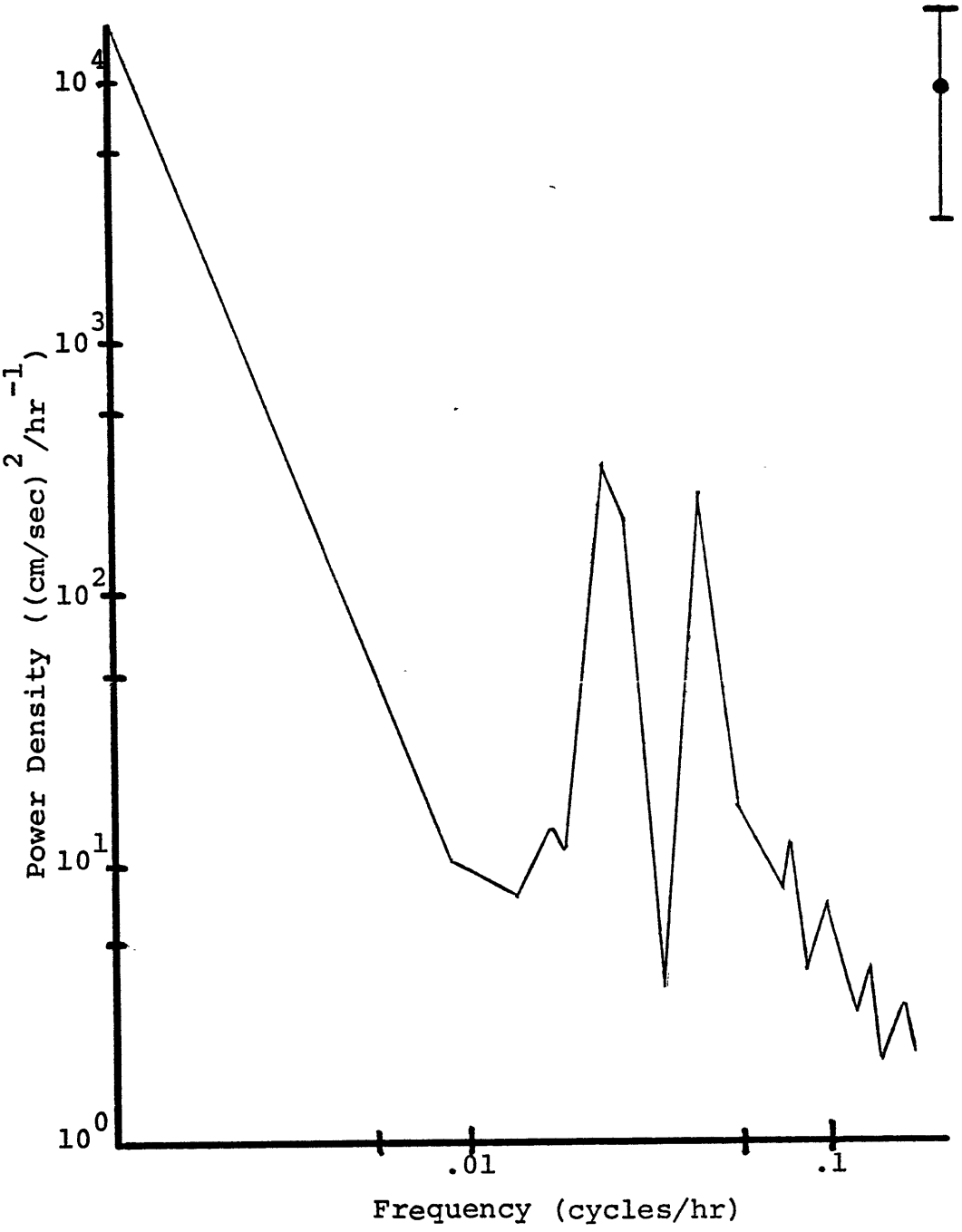

FIGURE 20
4301 U Power Density

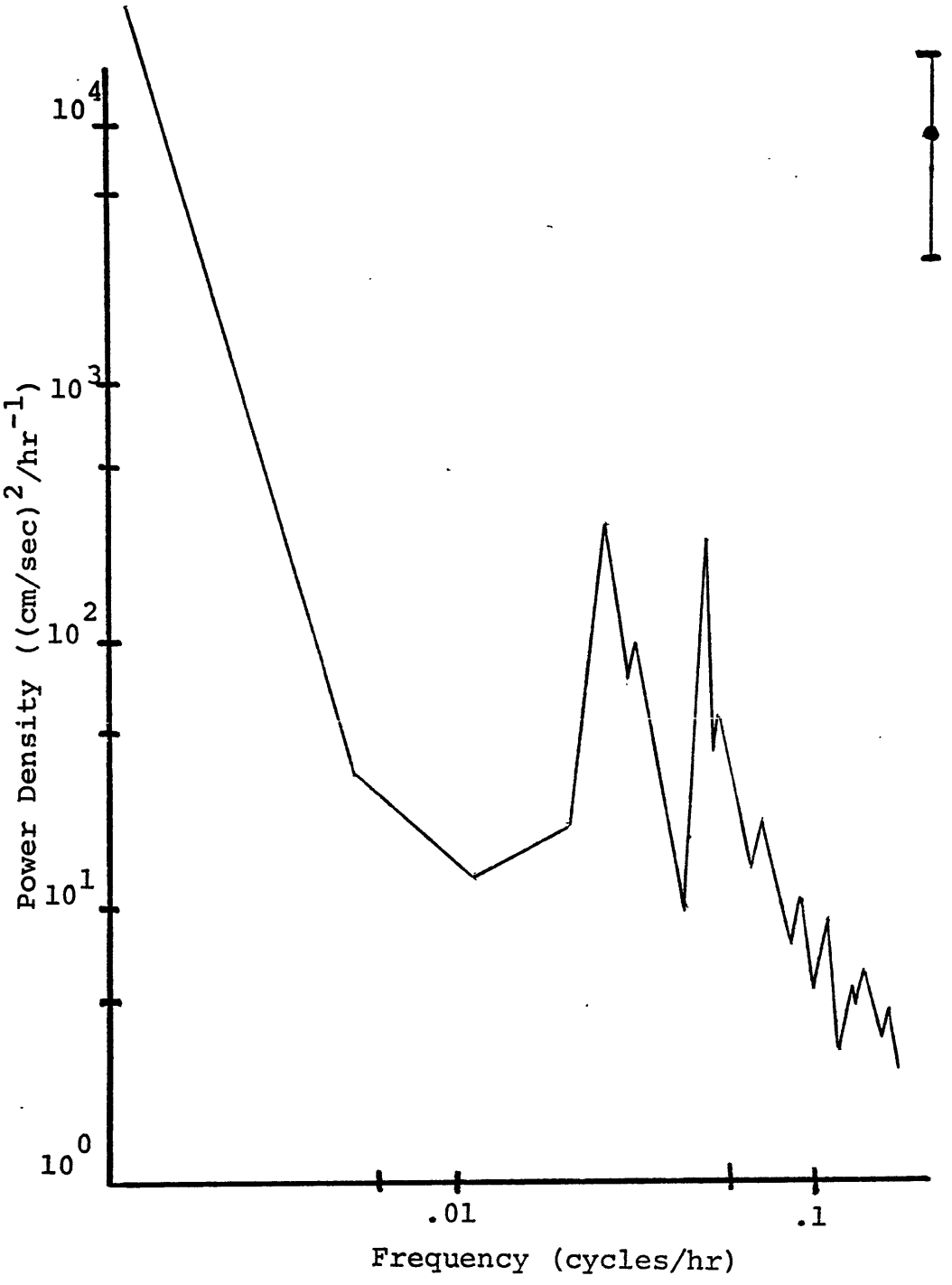

FIGURE 21
4301 V Power Density

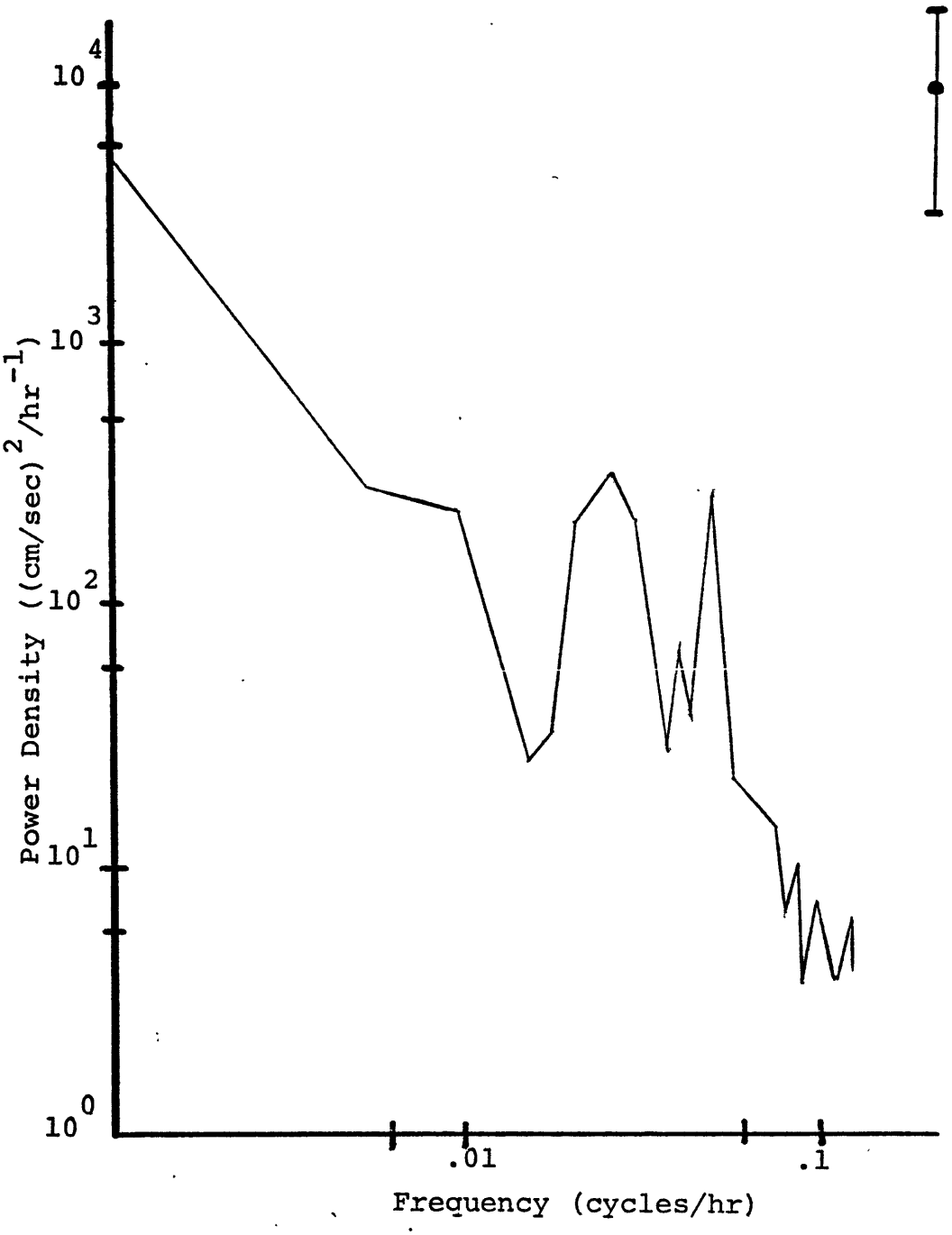

FIGURE 22
4302 U Power Density

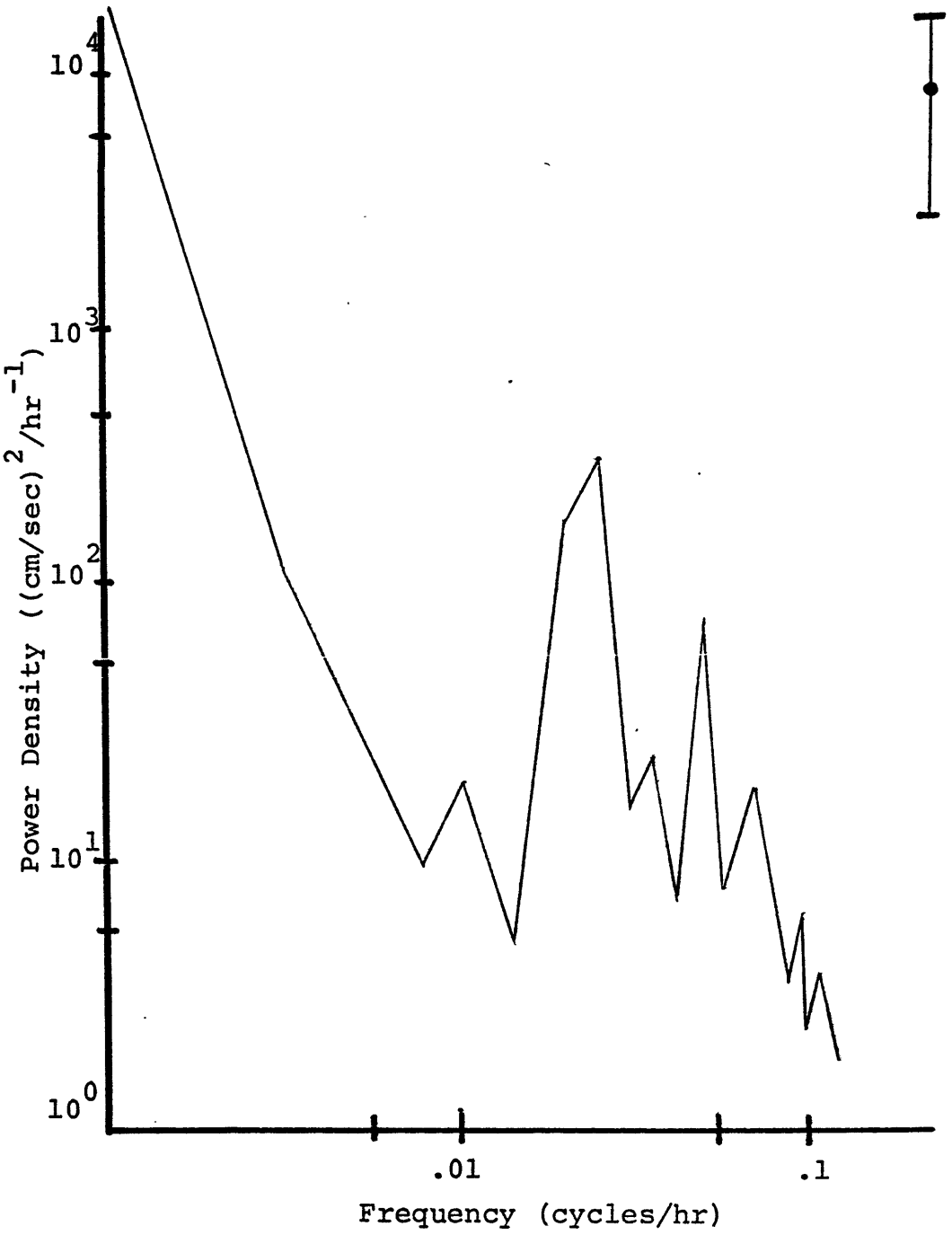

FIGURE 23
4302 V Power Density

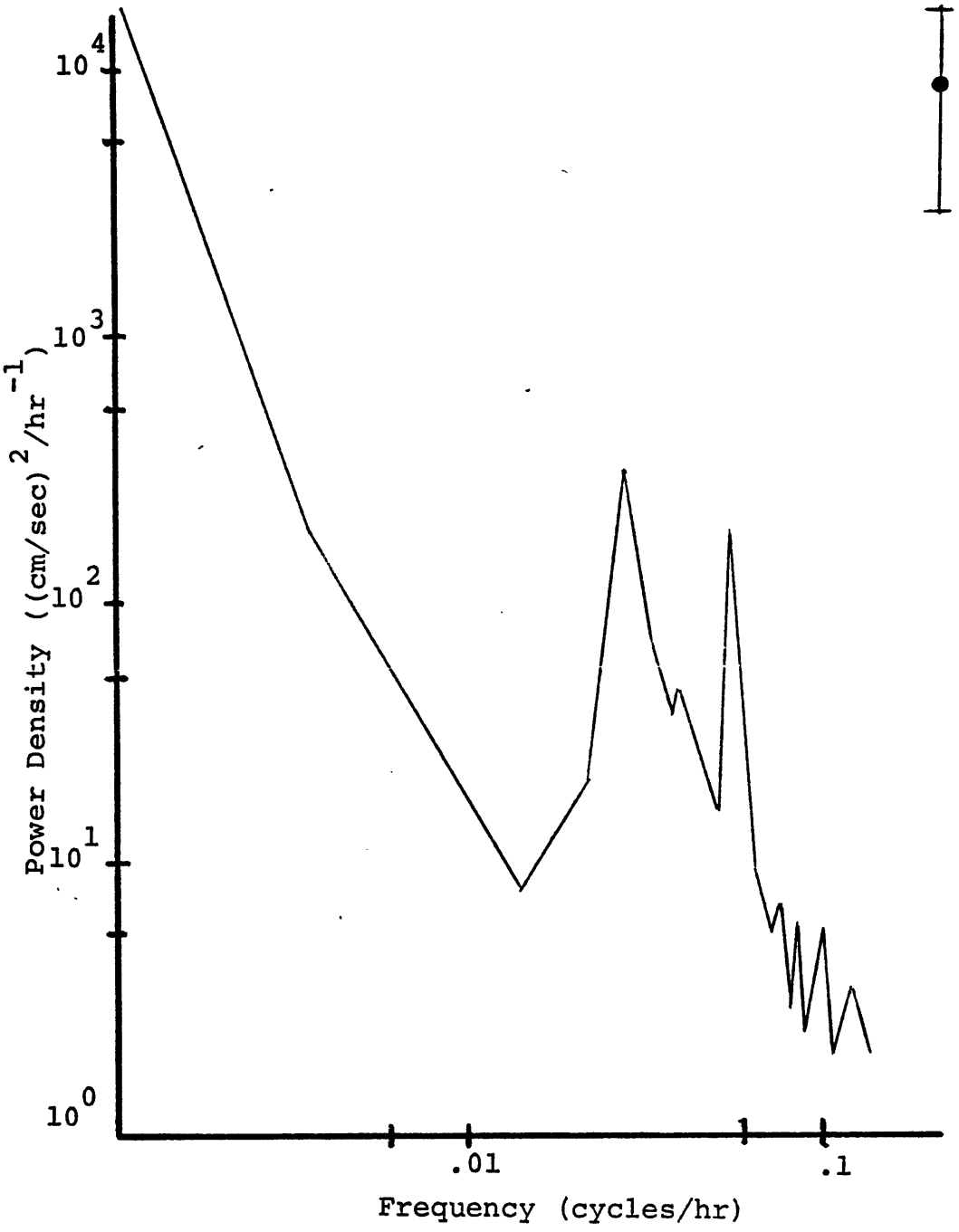

FIGURE 24
4312 U Power Density

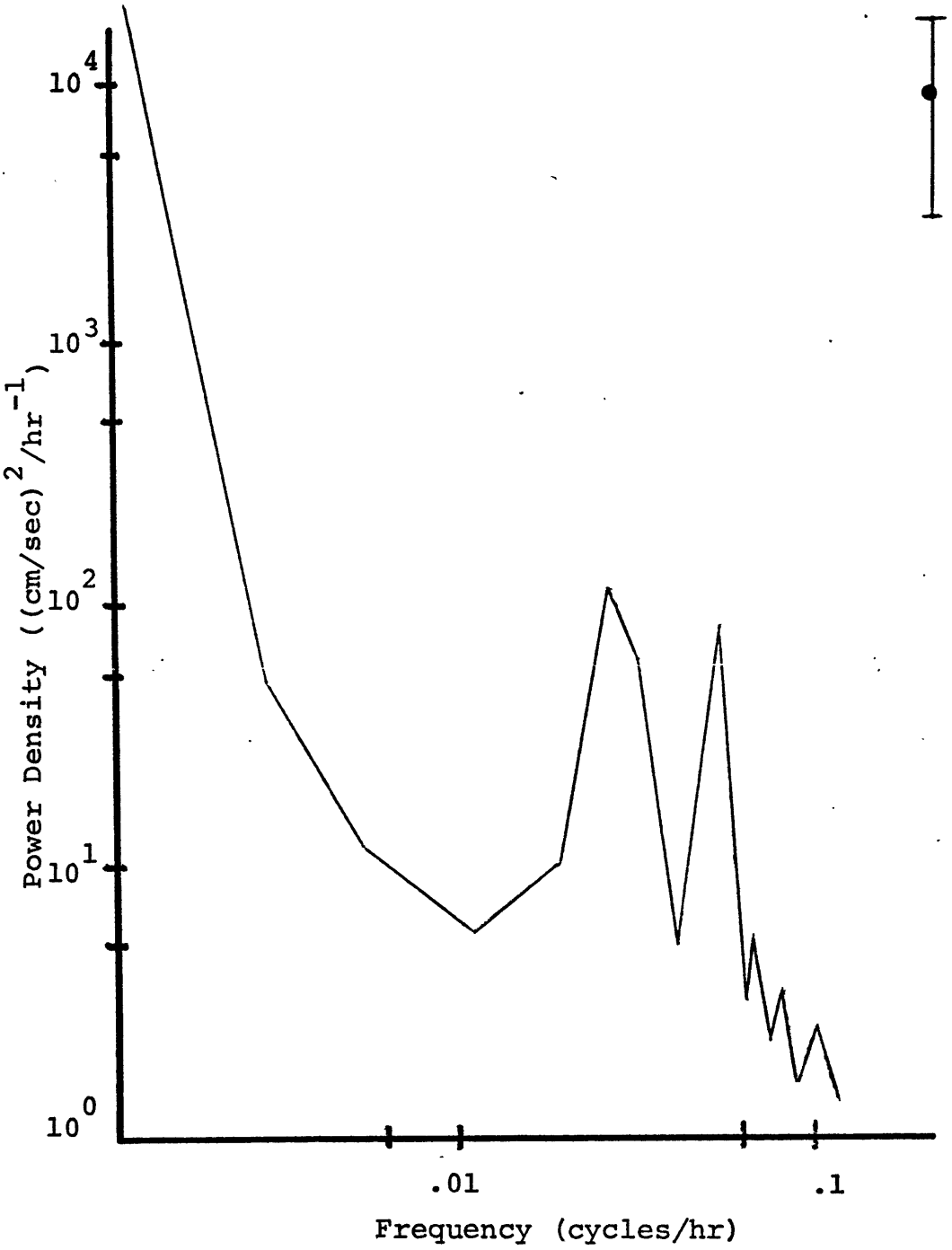

FIGURE 25
4312 U Power Density

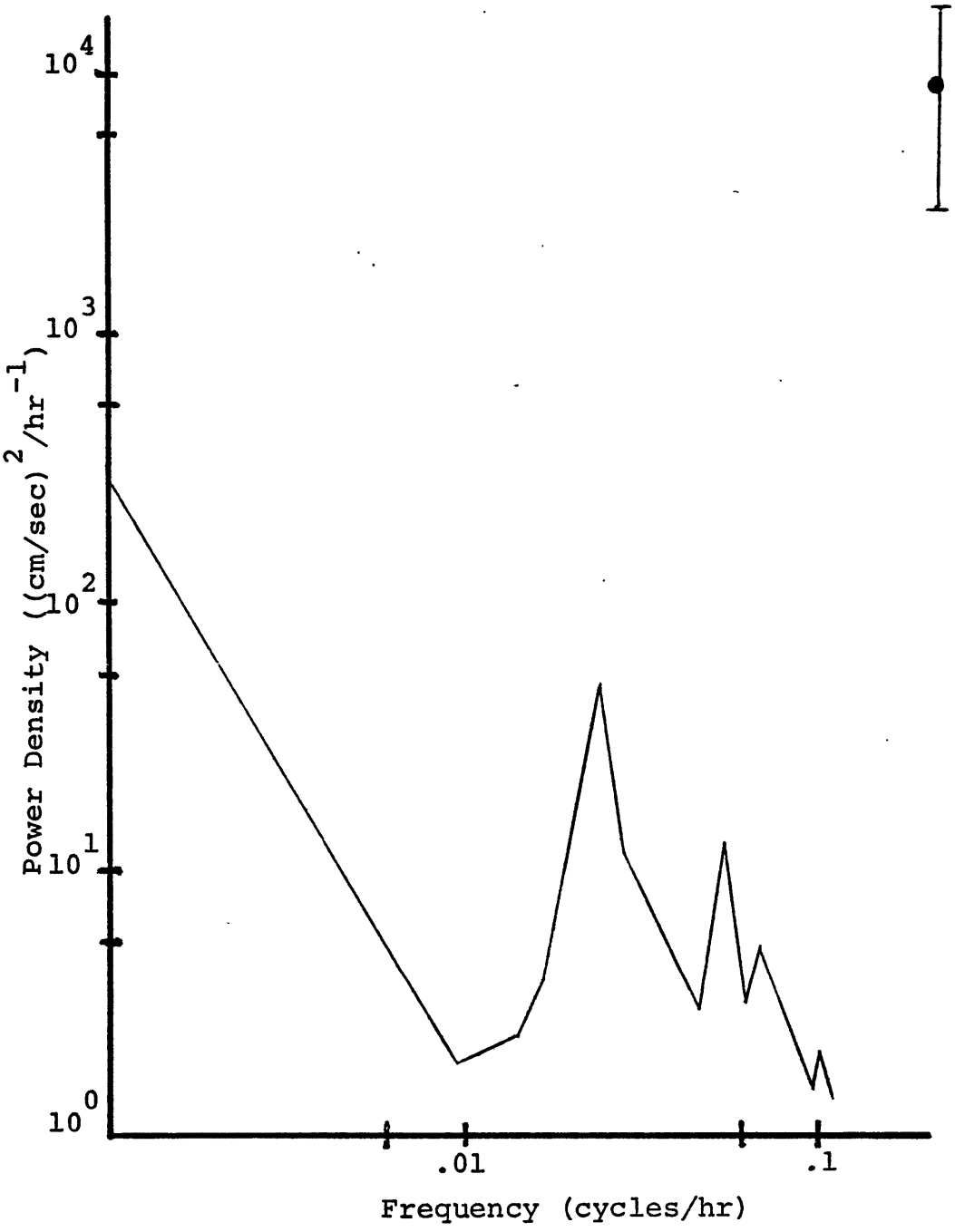

FIGURE 26

4332 U Power Density

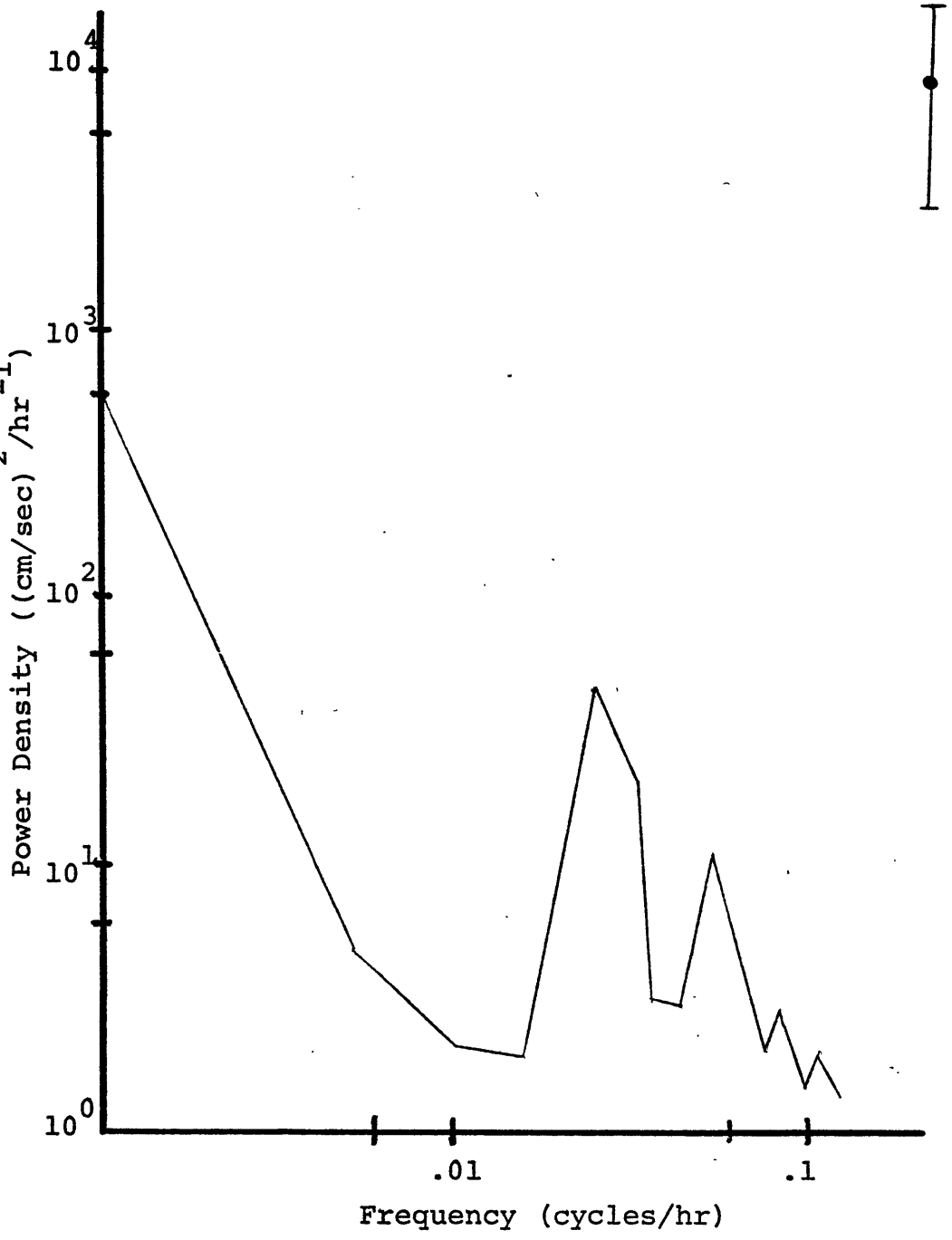

FIGURE 27
4332 V Power Density

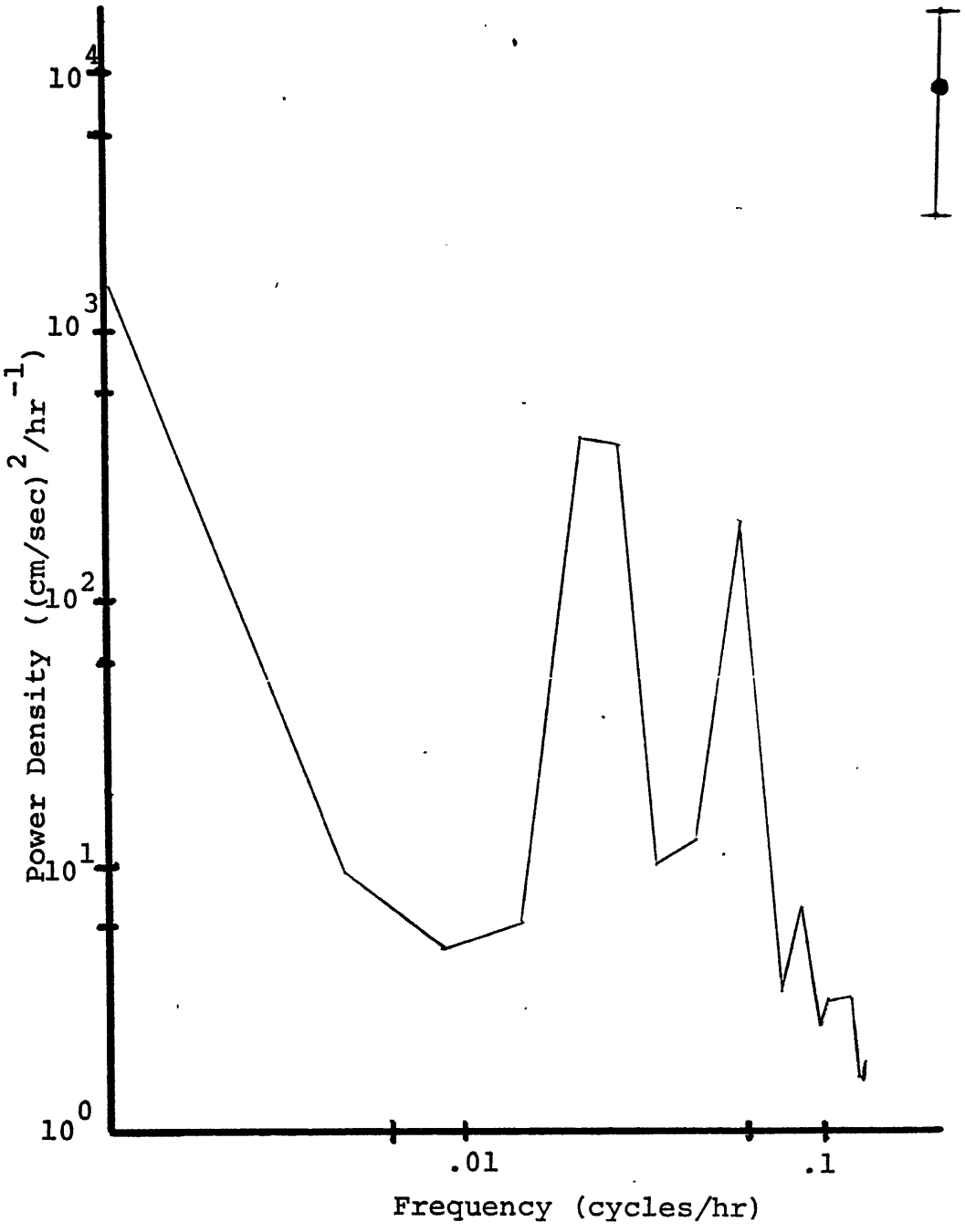

FIGURE 28
4342 U Power Density

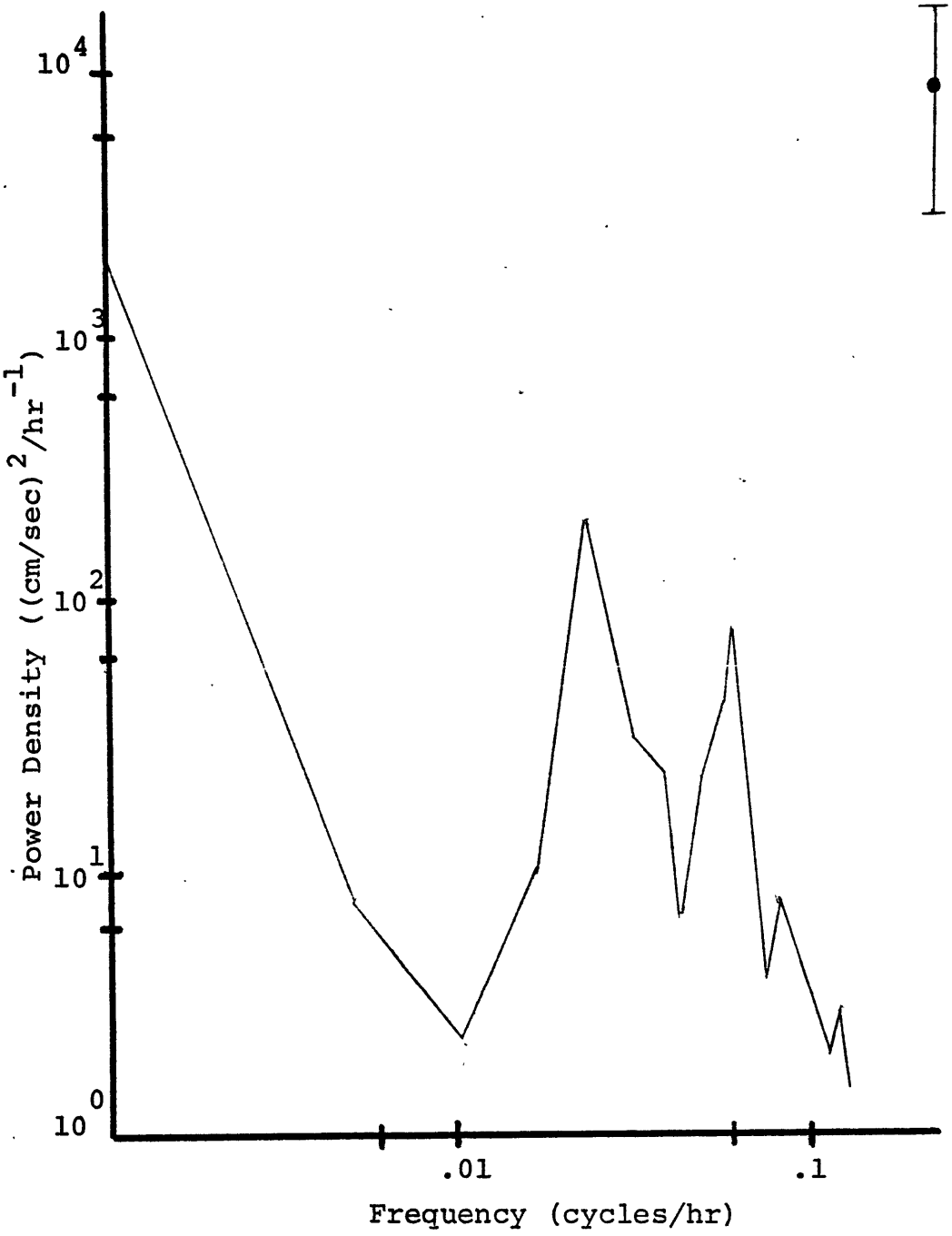

FIGURE 29
4342 V Power Density

hour averaged samples; there are 5 degrees of freedom in the lowest frequency band and 10 degrees of freedom in all others. Bars denote approximate 80% confidence limits. Normally one takes half the sum of the spectra from each of the two horizontal components to be the horizontal power density spectrum. However, in these figures the east and north spectra have not been added so that we might look at them separately.

Generally the spectra show a rise in power density from high to low frequencies. At the center of Array-2, 28°10.5N 68°23.8W, the inertial period is 25.3 hours. For purposes of this work, we are only interested in periods longer than the inertial period. Spectral levels for a single component usually agree to within an order of magnitude for all instruments in the lowest frequency band. The one exception is current meter 4332 where the spectral levels are approximately a factor of 10 lower in both components than at the other instruments. There are no obvious differences between surface mooring spectra and subsurface spectra.

It is informative to compare the spectral levels of instruments on mooring 424. In the u components, the spectra are universally red for all three instruments. However, we note that energy is rising faster as frequency gets lower at 1500 m. and 4000 m. than at 5000 m. Another distinction between the three instruments is in the band

of periods from 5 to 15 days. 4244 shows some energetic structure in this band, where current meters 4242 and 4243 show a well. This indicates that the motions previously discussed in the vector component plots are large enough to appear in the spectrum. Implications of the motion in this frequency band will be thoroughly pursued in Chapter 4. For the v components, the spectra look very similar at all three levels. No obvious structure is present in the 5-15 day band, and overall the v spectra are 6 to 10 times more energetic than the u components, at the lowest frequencies.

The other mooring with vertical information, 430, shows spectral differences between currents at 4000 m. and 5000 m. The u components of current meter 4302 show the enhancement in the 5 to 15 day band when compared to the u components measured on 4301 at 4000 m. The enhancement is less than that found on mooring 424. On mooring 430 the measured v component spectra are very similar to those on mooring 424.

Temperature Data

Three moored temperature time series were obtained from Array-2. Current meter 4354, whose velocity sensors failed to operate properly, yielded a temperature record 64 days long. At current meter 4301 there are temperature measurements for 68 days, and current meter 4242 recorded

temperature for 103 days. Plots of the low-passed, daily averaged temperature are shown in Figures 30 through 32. Record 4242, which at 1500 meters is near the bottom of the thermocline, shows considerably more variability than do the other two measurements. Of course, mooring 424 is a surface mooring, so vertical motions induced in the mooring line due to surface wave action may contaminate temperature measurements made from this mooring. Wunsch and Dahlen (1974) have discussed some of the problems to be expected from temperature measurements made from surface moorings.

We can see that the two 4000 m. measurements, one on each side of the ridge, show little variability for the first month of the experiment. Both show a sharp rise in temperature during the second month; the rise at instrument 4354 persists for roughly 20 days before the temperature settles back to its mean level and the instrument is recovered. At instrument 4301, however, the transients are not as short and the temperature remains higher for a longer period of time. Generally the longer period of high temperature at 4301 corresponds to the period of strong southward flow in the velocity field that was noted west of the ridge near the end of the experiment. The less energetic flow seen east of the ridge in the velocity field is perhaps reflected in the shorter transients in the temperature field at 4354. We can also note that the

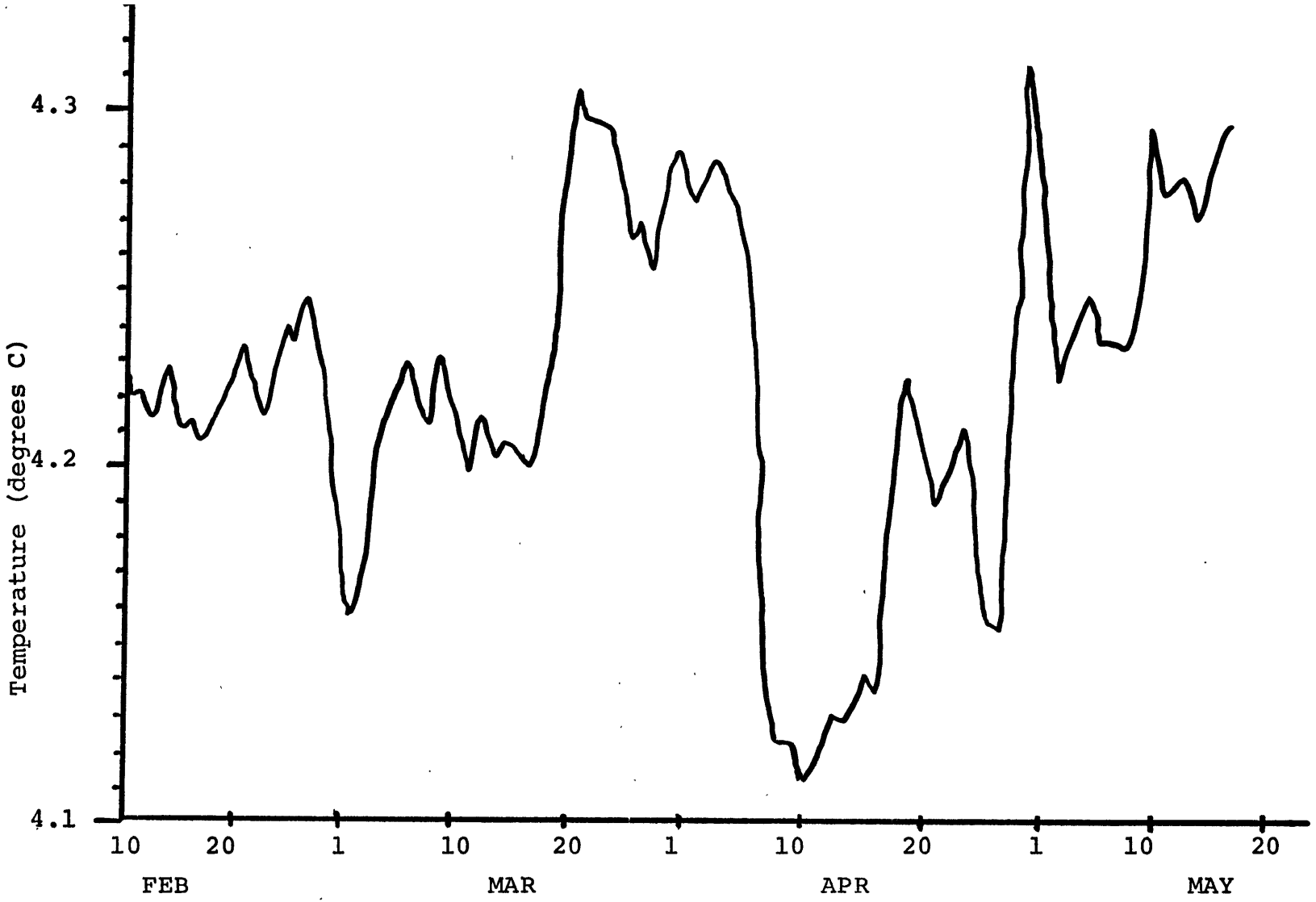

FIGURE 30
4242 Temperature

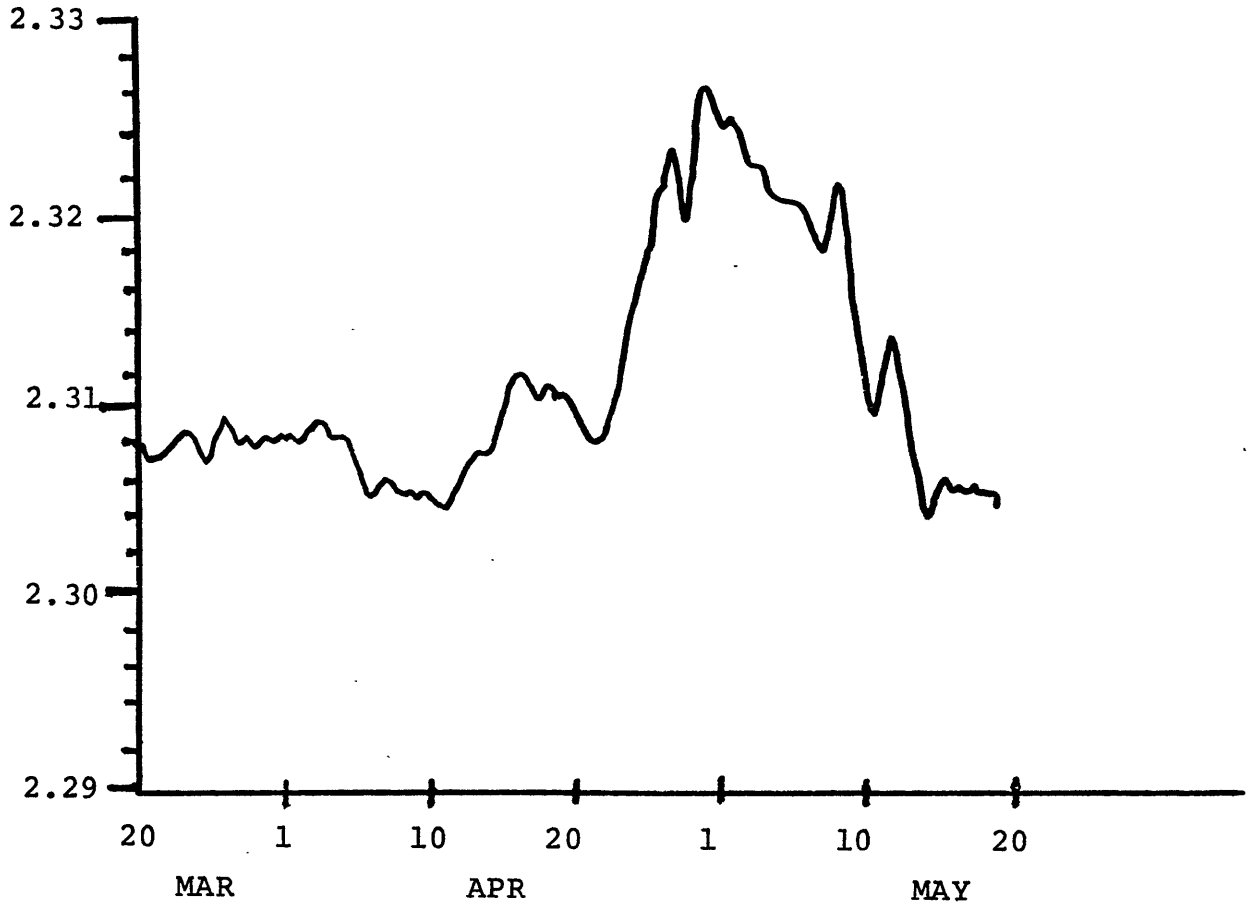

FIGURE 31
4301 Temperature

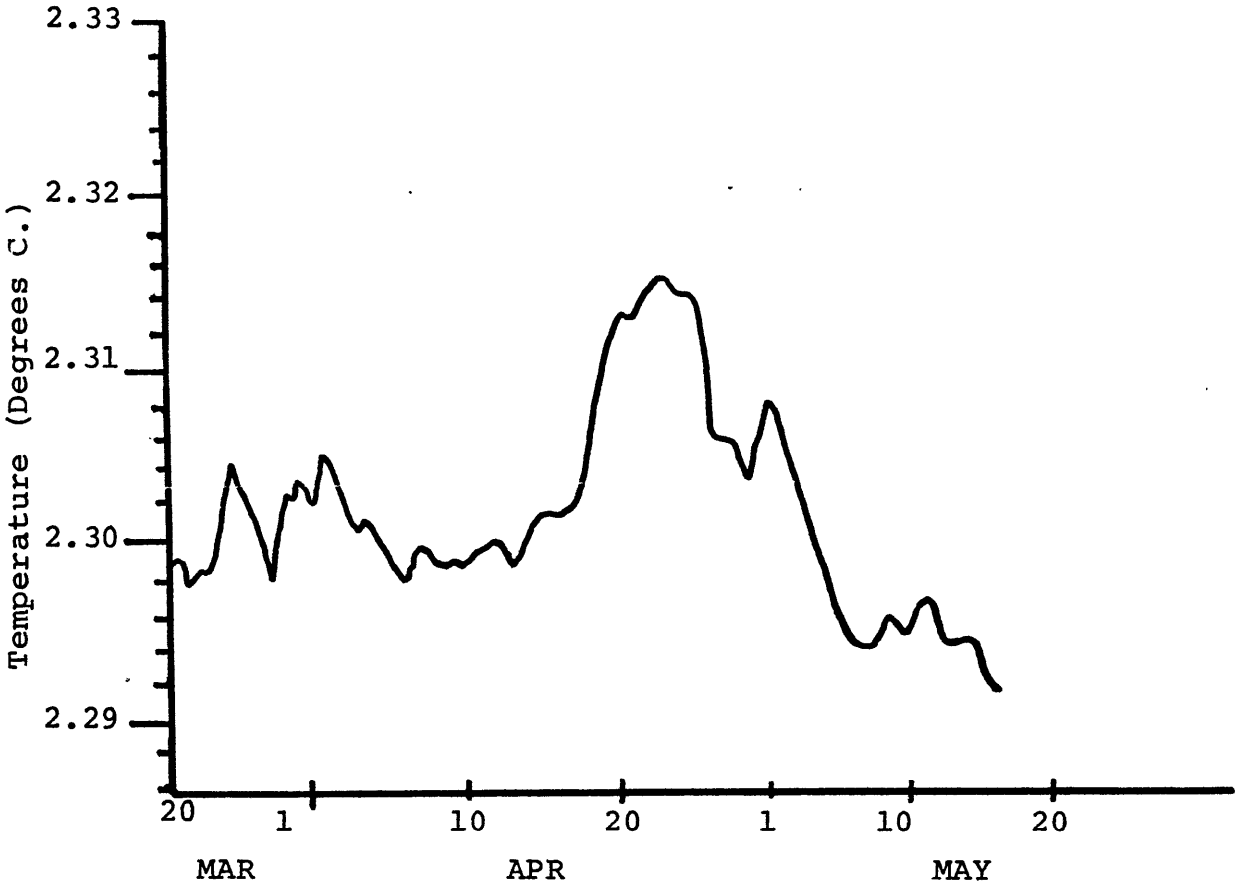

FIGURE 32
4354 Temperature

temperature mean at current meter 4301 is approximately .01° C higher than the mean at 4354. 4301 is located 7 meters deeper (3975 m.) than 4354 (3968 m.), so if this effect is real, there must be horizontal density gradients at this depth, and hence geostrophic shears. Wunsch and Dahlen (1974) report 10 m. vertical excursions of subsurface moorings, so the exact depth of the temperature sensor is not known for all times. In addition, they have found that a record of pressure at the instrument is needed to recover the true temperature signal from the measured one, which is contaminated from vertical excursions. Lacking any pressure records to go with the temperature records from Array-2, we can only hope that the measurements made are a good estimate of the true temperature.

Power density spectra for the three temperature measurements are shown in Figures 33 through 35. We see that the inertial and tidal peaks and the overall shape of the spectrum is very similar to those found by Wunsch and Dahlen (1974). In addition, energy levels in the lowest frequencies appear similar to those of Wunsch and Dahlen to within a factor of 2. Current meters 4301 and 4354 show only small differences in their spectra. Wunsch (1972) has computed a normalized spectrum of vertical kinetic energy from a 14 year long series of hydrographic measurements at Bermuda. Using some results

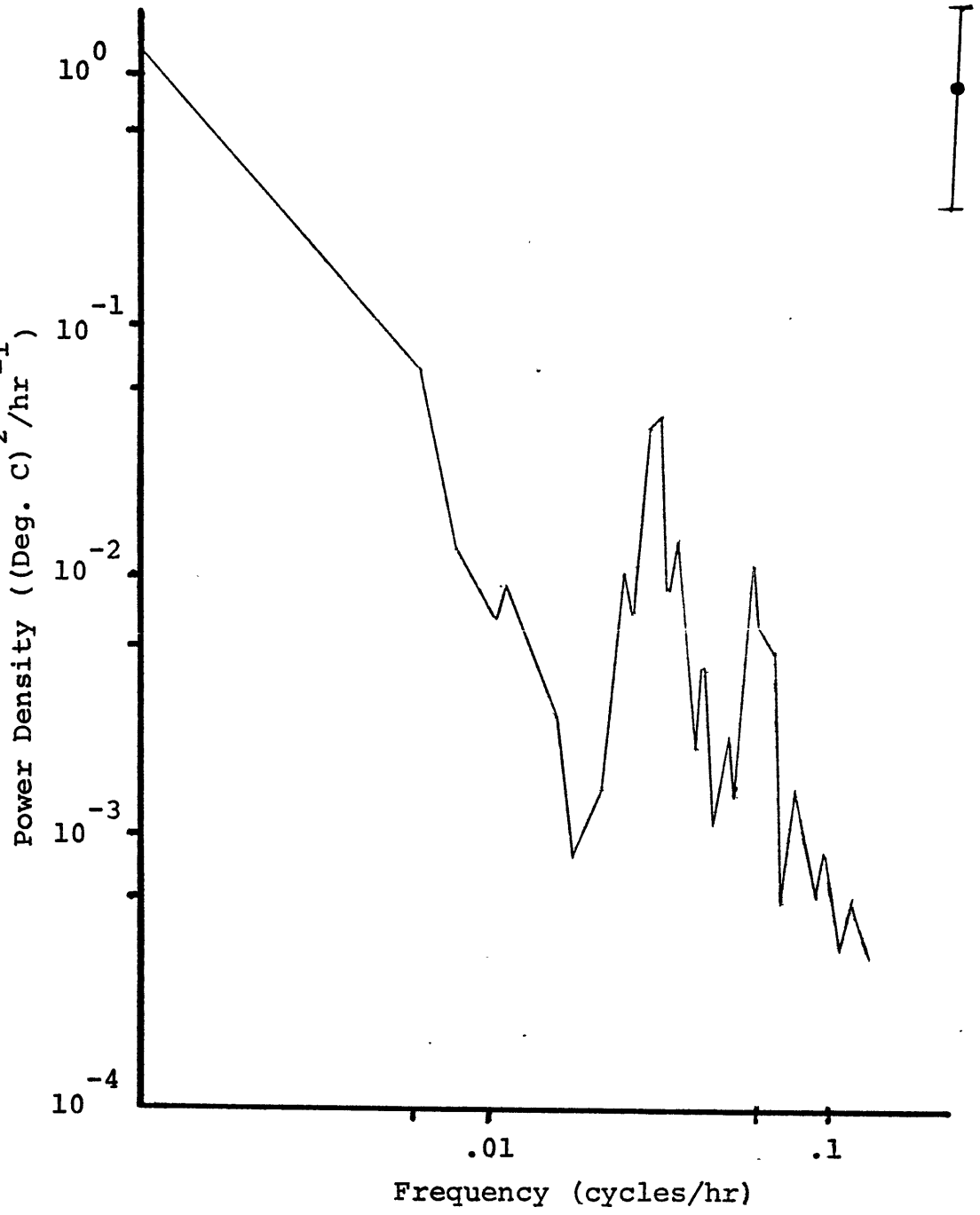

FIGURE 33
4242 Temp. Power Density

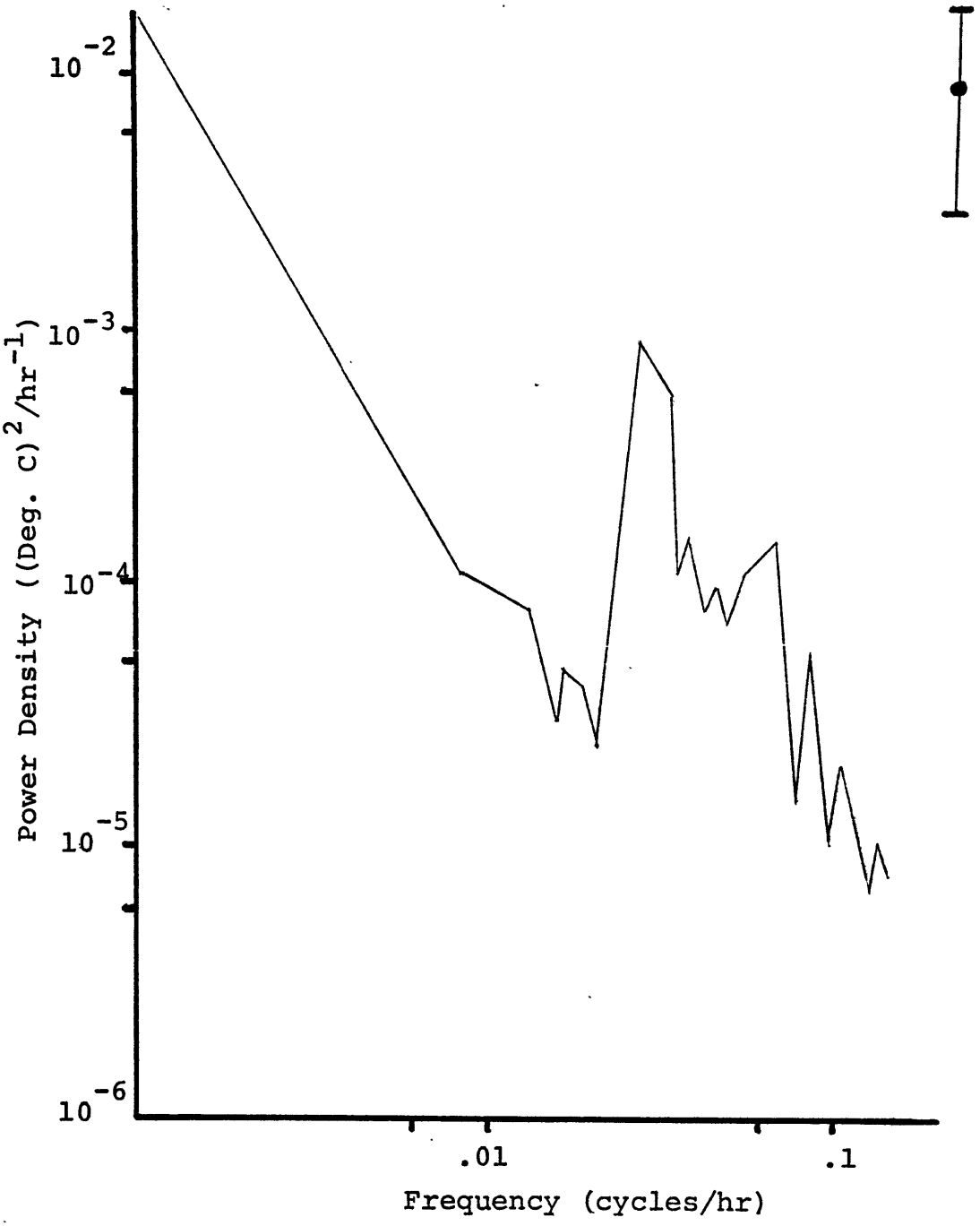

FIGURE 34
4301 Temp. Power Density

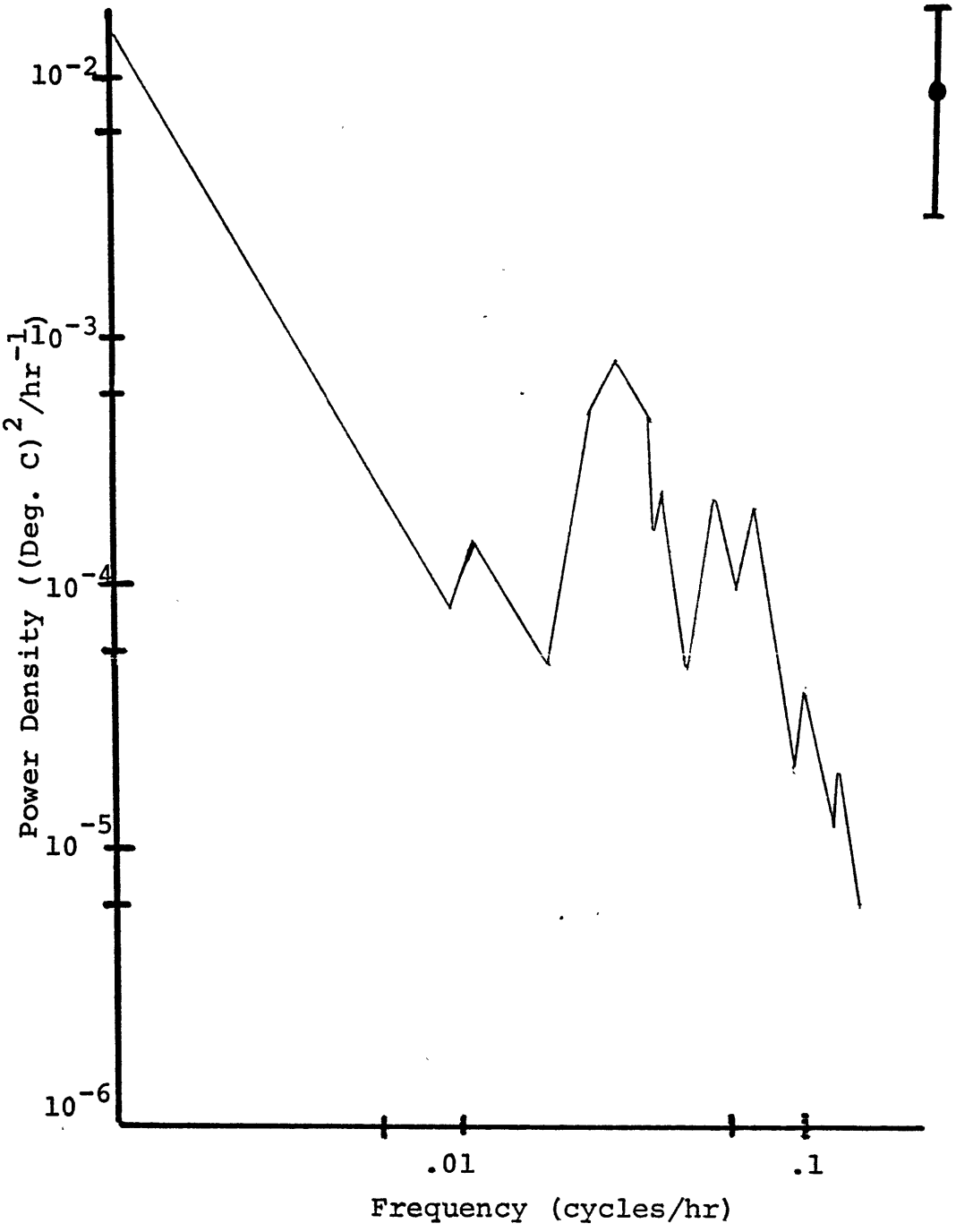

FIGURE 35

4354 Temp. Power Density

from their temperature-pressure recorder, Wunsch and Dahlen (1974) have computed a similar normalized spectrum. These two sets of data, along with the above temperature data from Array-2 at 4000 meters have been plotted in Figure 36. The spectrum of vertical velocity has been calculated from

$$\Phi_{ww}(\sigma) = \frac{(2\pi\sigma)^2}{2} \Phi_{TT}(\sigma) \Big/ \left(\frac{dT_0}{dz}\right)^2$$

where Φ_{TT} is the power density computed above and shown in Figures 33 through 35. $\frac{dT_0}{dz}$ is the mean temperature gradient at each depth, and σ is the frequency in cycles per hour. Before plotting, all values have been multiplied by N(z), the local Brunt-Vaisala frequency, in order to normalize. This is because the linear WKBJ solutions to the wave equation for w are proportional to $N(z)^{-1/2}$. Thus by multiplying the spectrum by N(z), we are effectively cancelling the depth dependence, and the resultant should show depth independent spectral levels. We can see in Figure 36 that generally the MODE-0 temperature data from instruments 4301 and 4354 are in good agreement with vertical velocity spectral levels found by Wunsch and Dahlen. At this time we have not been able to compare the very low frequency temperature spectrum in the MODE area to that at Bermuda measured by Wunsch (1972) due to the lack of very long term temperature measurements in

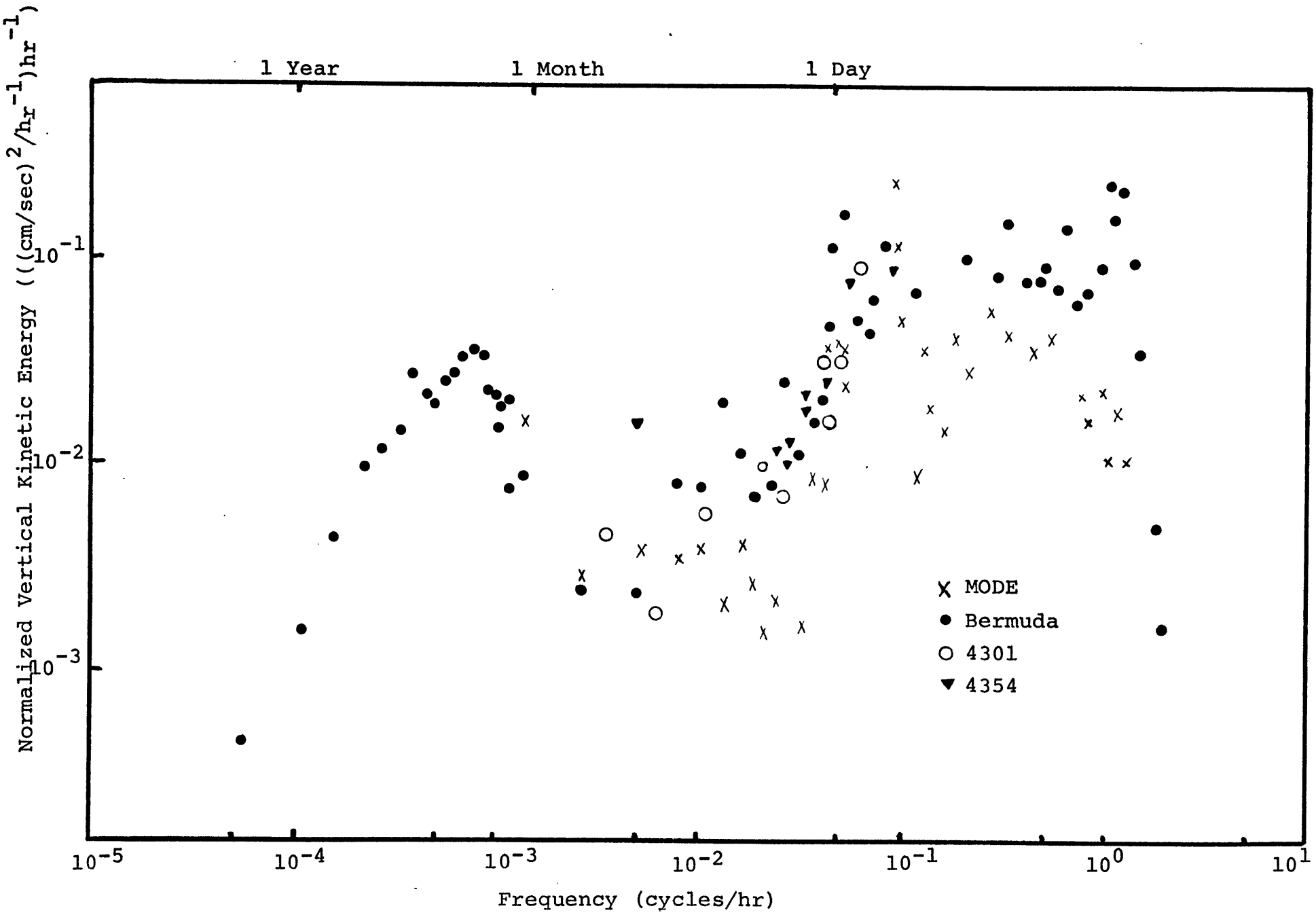
1 Year
1 Month
1 Day
Normalized Vertical Kinetic Energy (((cm/sec)^2/hr^{-1})hr^{-1})
10^{-1}
10^{-2}
10^{-3}
MODE
Bermuda
4301
4354
10^{-5}
10^{-4}
10^{-3}
10^{-2}
10^{-1}
10^{0}
10^{1}
Frequency (cycles/hr)

FIGURE 36

the MODE area. All of the values calculated from record 4242 plot off the figure by several orders of magnitude, indicating contamination of the record due to mooring motion.

Summary of the Data

We can see from the data presented thus far that there are some very complicated processes occurring in the vicinity of Array-2. The few current meter measurements that we have suggest that there are horizontal anisotropies present in the velocity field that are different from the effects on the flat bottom as seen in Arrays-1 and 3. Progressive vector diagrams from instruments only 40 km. apart, as with 4301 and 4342, show marked dissimilarity. In the vicinity of the chain of seamounts we see strong southward currents whose time scales cannot be determined from these measurements alone. To the east of the seamount chain no such trend is evident. Temperature measurements on either side of the ridge show a dissimilarity during the last month of the experiment when a strong flow from the north is present west of the ridge.

In the vertical we have only two separate measurements, but these also suggest some interesting phenomena not observed in the other MODE-0 arrays. The deepest measurements,

approximately 100 m. above the local bottom in each case, show intensification in the east components of current at periods of 5 to 15 days when compared to similar measurements 1000 m. above the bottom. This intensification is clearly evident in the horizontal velocity spectra.

There are some similarities to the data returned from Arrays-1 and 3 however. The characteristic 60-75 day eddy period so prominent on the smooth area is also observed over the rough topographic area of Array-2. Large scale effects may be similar everywhere in the MODE area; in Array-2 we may be witnessing the breaking up of the mesoscale eddies by the rough bottom. In the next chapter, we will continue to explore the effects of bottom topography.

CHAPTER 3--SOME CALCULATIONS MADE FROM SPECTRA

Coherences

We are interested in comparing records from neighboring instruments in a more quantitative fashion. In the last chapter we saw that the presence of a chain of seamounts seemed to divide the data from Array-2 into distinct regions. First, the two measurements west of the ridge seemed to show a strong southward flow near the end of the two month record. To the east of the ridge the only measurements we have suggest that (1) the presence of seamounts influences the flow; (2) 30 km. east of the ridge the local topography has an influence on the flow; (3) there is no evidence of the strong southward flow east of the ridge.

A more quantitative measurement of similarities are the coherences between records. We can define the coherence between two random processes x and y as

$$C_{xy}(\omega) = \frac{\Phi_{xy}(\omega)}{\left\{ \Phi_{xx}(\omega)\ \Phi_{yy}(\omega) \right\}^{1/2}}$$

where Φ_{xy} is the cross spectrum between processes x and y; Φ_{xx} is the auto spectrum of x. The coherence is thus a complex quantity whose amplitude is less than or equal to one. A detailed discussion of the meaning of coherence is given in Amos and Koopmans (1963) and in Jenkins and Watts (1968). All of our data are finite and sampled, and for data of this type the usual procedure for taking

an expected value is to average Fourier coefficients over some small frequency band, say of width N Fourier coefficients. Thus, an estimator for Φ_{xx} is

$$\Phi_{xx} = E\{\hat{x}_n \hat{y}_n^*\} = \frac{1}{N} \sum_{n=1}^{N} \hat{x}_n \hat{x}_n^*$$

where $\hat{x}_n$ denotes the nth Fourier coefficient of x. The * denotes a comples conjugate. Continuing along this line, then, an estimator for the coherence between random processes x and y is

$$C_{xy}(\omega) = \frac{\frac{1}{N} \Sigma \hat{x}_n \hat{y}_n^*}{\left[\left(\frac{1}{N} \Sigma \hat{x}_n \hat{x}_n^*\right)\left(\frac{1}{N} \Sigma \hat{y}_n \hat{y}_n^*\right)\right]^{1/2}} = \frac{\Sigma \hat{x}_n \hat{y}_n^*}{\left[\Sigma \hat{x}_n \hat{x}_n^* \; \Sigma \hat{y}_n \hat{y}_n^*\right]^{1/2}}$$

where all sums are understood from 1 to N. This is the definition of coherence usually used when working with oceanographic time series. After a value of coherence amplitude is calculated, one usually looks in a table of coherence tabulations such as Amos and Koopmans (1963) to find the level of significance for the given number of degrees of freedom, N.

Strictly speaking, however, coherence defined in this manner and listed in the tables implicitly assumes that the underlying process is white. In fact, this may not be the case, for oceanographic spectra are notoriously red. Because of this, the traditional estimator for coherence is biased when estimating oceanographic spectra. We can see from the algorithm that the expected values are weighted unevenly by the frequencies containing the most

power, so the estimates of coherence obtained in this manner may not be reliable.

It is possible to construct another estimator of coherence to remedy this problem. If we sum coherence estimates and then average, as opposed to averaging spectra and then forming coherence estimates, we get an estimator for coherence of the form

$$C_{xy}(\omega) = \frac{1}{N} \sum \frac{\hat{x}_n \hat{y}_n^*}{|\hat{x}_n \hat{y}_n^*|}$$

where the sums again run from 1 to N. This estimator first normalizes all spectral estimates so that the magnitude of the estimate is unimportant; all vectors thus have the same magnitude and only the phase relationship is important. Now we are really computing a measure of phase stability instead of coherence in the strictest sense. Of course, the distribution of coherence and phase for this estimator may be very different than that for the traditional estimator, and in fact this distribution is not tabulated. Thus questions of statistical significance arise that may not be answerable without some additional calculations.

We hope to make coherence calculations from the data, and since we are mainly interested in low frequency variability, we are working in the red portion of the spectrum. If we calculate coherence both ways and compare the results, we should be able to get an idea of

how meaningful our results are. If the two calculations are wildly different, then the redness of the spectrum is probably biasing the calculation so as to render the results meaningless. If the two estimators give consistent values, then we might assume that the redness of the spectrum is not too important over the band we are interested in, and the results are in fact meaningful.

In Table II estimates of coherence amplitude between pairs of corresponding horizontal velocity components from Array-2 current meters are given. The coherences have been calculated using both estimators for all possible pairs of current meters at a given depth. In addition coherences between temperature records and temperature and velocity records have been calculated. The estimates were made using 8 degrees of freedom, so the band of interest included in the estimate included periods from about 10 days to the record length. Since the record lengths vary, the width of this band varies somewhat also. Amos and Koopmans (1963) list .6 as the 95% confidence limit of coherence amplitude for 8 degrees of freedom. Physically, this means that two random processes that are incoherent (such as light radiated from two different point sources) will give a coherence estimate less than .6 95% of the time when computed with 8 degrees of freedom.

In the coherence estimates greater than .6, we note

TABLE II.

Coherence and Phase from MODE-0 Array-2

Pair	Depth (m.)	Separation (km.)	Component	Coherence/Phase in Lowest Freq. Band	
				TD*	PWC*
4242-4243	1500-4000		u	.74	.70
				-88	-81
			v	.42	.39
				63	49
4242-4244	1500-5000		u	.65	.64
				-72	-70
			v	.59	.55
				-29	-22
4243-4244	4000-5000		u	.90	.89
				4	-1
			v	.72	.68
				23	29
4301-4302	4000-5000		u	.96	.96
				-37	-39
			v	.98	.92
				4	10
4243-4301	4000	4	u	.97	.93
				12	10
			v	.99	.98
				-7	-3
4244-4302	5000	4	u	.90	.90
				5	6
			v	.99	.98
				12	10
4243-4312	4000	27	u	.82	.69
				15	17
			v	.36	.11
				-132	19
4243-4332	4000	19	u	.82	.69
				15	17
			v	.42	.30
				2	-86
4243-4342	4000	37	u	.56	.47
				-5	8
			v	.56	.49
				-51	-37
4301-4312	4000	25	u	.95	.92
				-9	-7
			v	.94	.90
				-22	-16
4301-4332	4000	17	u	.62	.60
				-44	-49
			v	.91	.87
				-1	6

* TD = Traditional Coherence Estimate

PWC = Prewhitined Coherence Estimate

TABLE II. (continued)

Pair	Depth (m.)	Separation (km.)	Component	Coherence/Phase in Lowest Freq. Band	
				TD	PWC
4301-4342	4000	37	u	.60	.57
				-73	-79
			v	.48	.38
				-49	-70
4312-4332	4000	19	u	.80	.75
				-53	-40
			v	.93	.88
				13	-1
4312-4342	4000	27	u	.84	.78
				-66	-37
			v	.57	.40
				0	-17
4332-4342	4000	18	u	.71	.66
				-24	-16
			v	.79	.72
				27	20

that there is agreement to within .1 between the two coherence estimators for amplitude and to within about 20% for the phase estimate. Even for those values less than the 95% level the agreement in coherence estimates is reasonable good, although phase estimates vary substantially between the two methods. However, for incoherent processes there is much error in phase estimation anyway, so this should not be bothersome. We also note that the value for prewhitened coherence is less than the traditional estimate. This is also to be expected: the prewhitened coherence estimate effectively includes information equally from all coefficients instead of much information from a single coefficient, so the coherence should go down. Overall we may conclude that our estimates are in fact realistic, because those estimates that are significant with one estimator are significant with the other.

It is helpful to look at coherence as a function of horizontal separation of measurements. Figures 37 and 38 show plots of coherence versus horizontal separation as calculated by GSW for data from Arrays-1 and 3. The frequency band is again the lowest available. As GSW have noted, coherence versus horizontal separation plots as nearly a linear relationship independent of direction. There is no obvious anisotropy in the data from the smooth

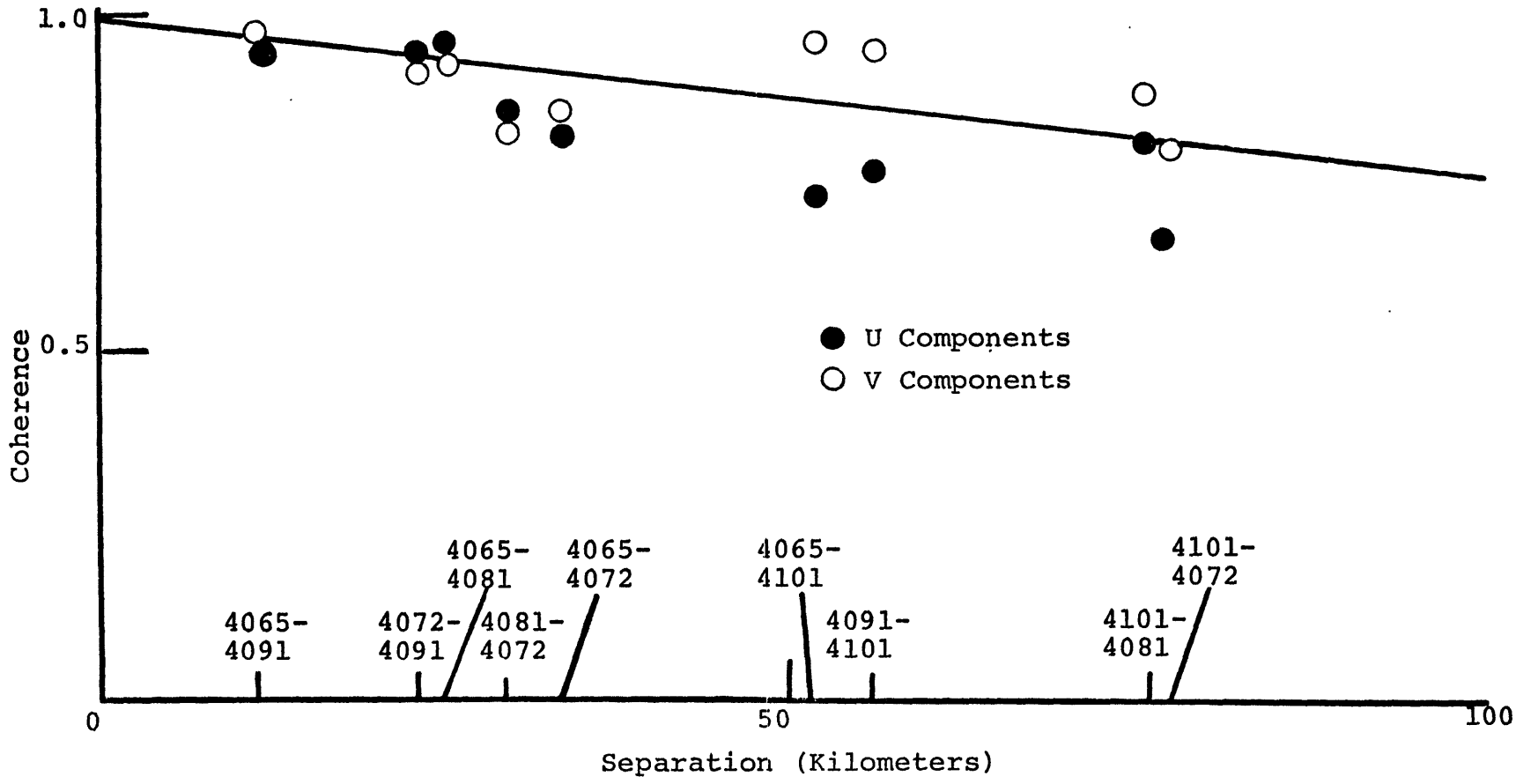

FIGURE 37

(from GSW)

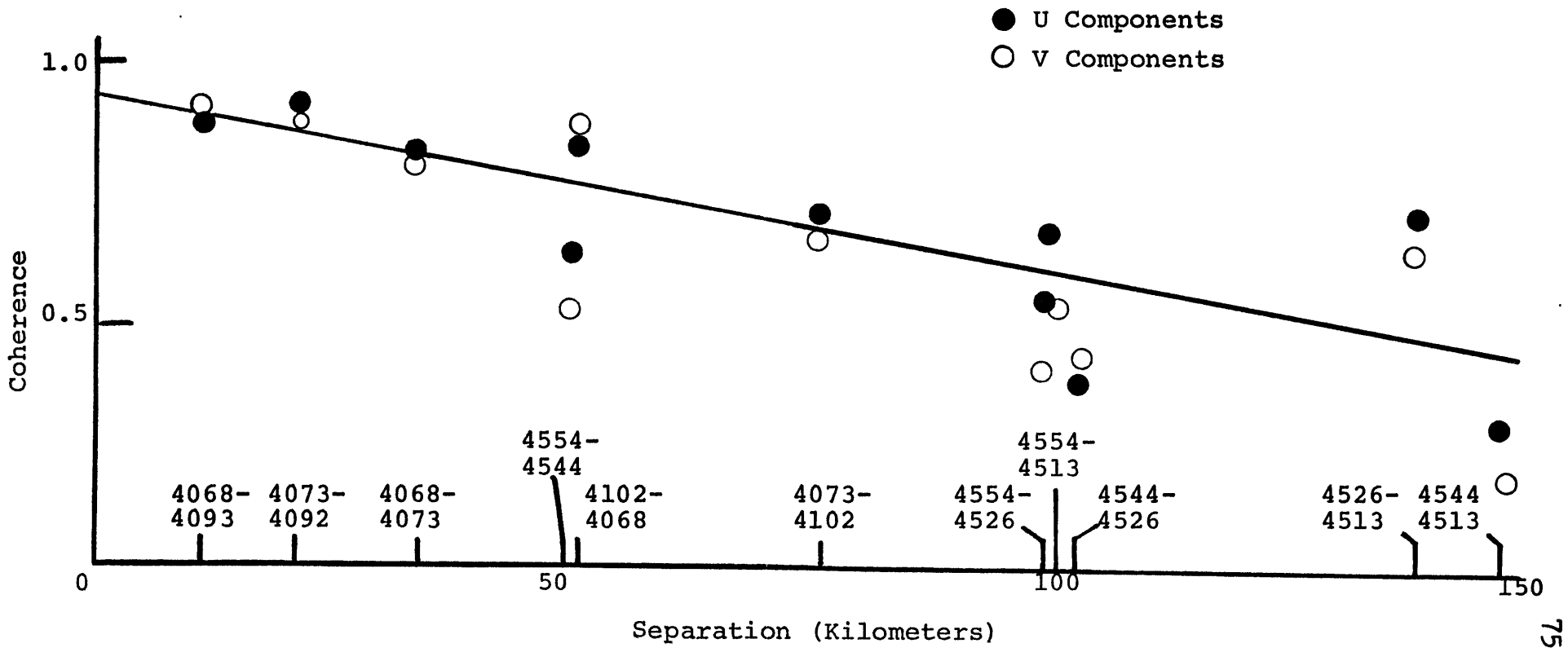

FIGURE 38
(from GSW)

area. Their plots show that for 1500 m.

$$C(\Delta r) = .95 - 2\times10^{-3}\Delta r$$

and at 4000 m.,

$$C(\Delta r) = .95 - 3\times10^{-3}\Delta r$$

where C is the coherence and Δr is the separation between instrument pairs in kilometers. The 95% level of significance, .6 here, is crossed at about Δr= 100 km. for the measurements at 4000 m. This implies that the pattern we are viewing has a horizontal extent of something greater than a distance of 100 km.

Similar plots have been constructed in Figure 39 from the coherences calculated from Array-2 measurements. Because of the design of the experiment, there are no separations larger than 37 km., so we are immediately limited in constructing a coherence-horizontal separation diagram. We note the very large scatter of plotted values. Obviously the data cannot be well fit with a single linear relationship due to the anisotropies involved. On Figure 39 a line has been drawn corresponding to the fit obtained by GSW at 4000 m. for Array-1 and Array-3. Though coherence in Array-2 does not fit a linear law, it is seen that coherence falls off generally much faster with increasing horizontal separation than in the results on the smooth bottom topography. Some of the rough area results do agree with the smooth, but in general there is no good agreement. We note the

FIGURE 39

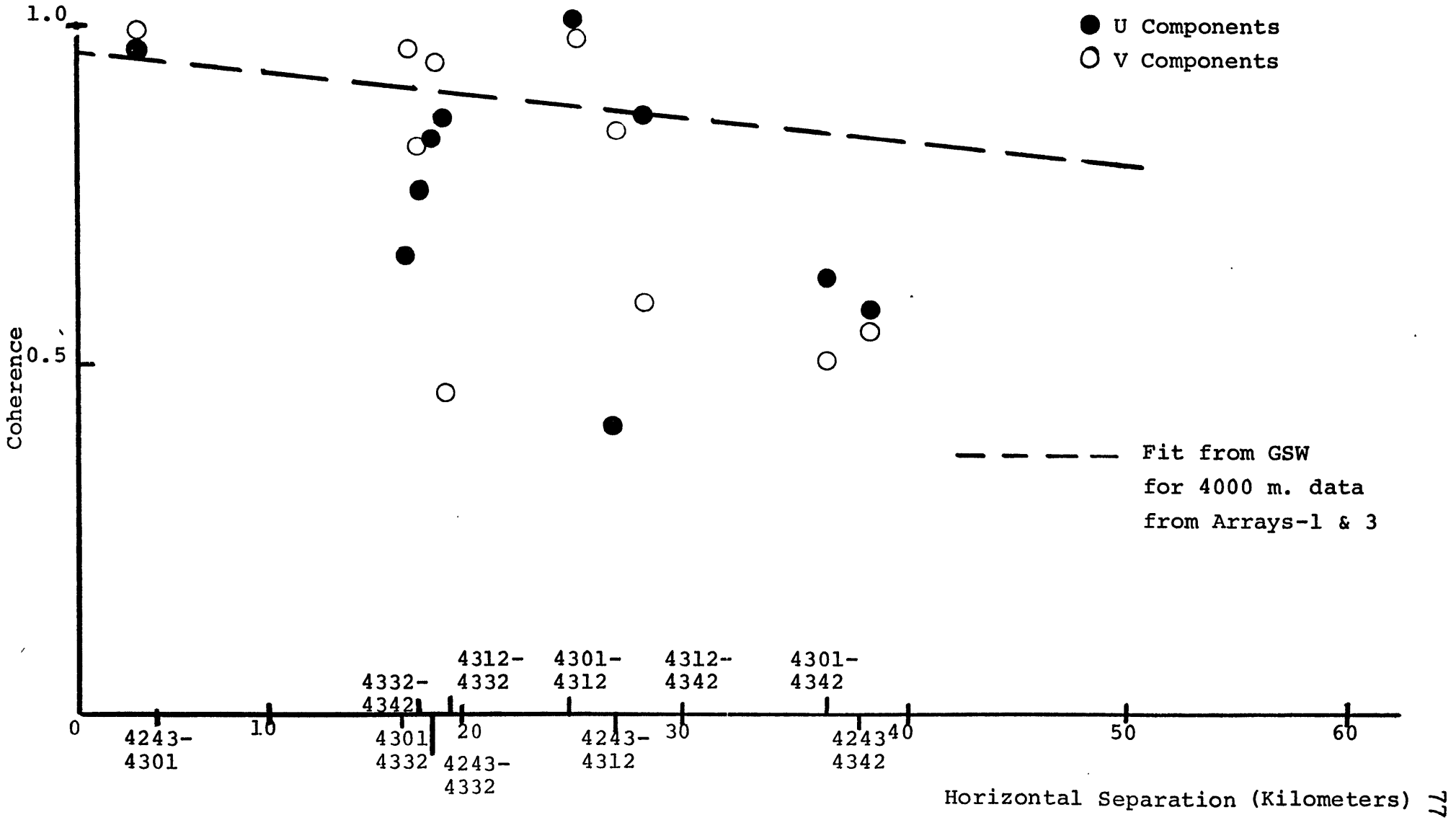
1.0
0.5
0
Coherence
U Components
V Components
Fit from GSW
for 4000 m. data
from Arrays-1 & 3
4243-
4301
4301
4332
4243-
4332
4243-
4312
4243
4342
4332-
4342
4312-
4332
4301-
4312
4312-
4342
4301-
4342
10
20
30
40
50
60
Horizontal Separation (Kilometers)

apparent discrepancy between the calculations for u and v components for Array-2. GSW found that coherence between east components was not significantly different than coherence between north components; however, the Array-2 calculations show a striking disparity in component coherences. In pairs 4243-4332, 4243-4312, and 4312-4342 the v component coherence is generally much less than u coherence; in the pair 4301-4332 the v coherence is much greater than the u. Except for the pair 4312-4342, each instrument of these pairs is separated from the other member of the pair by the ridge.

Some coherence estimates, on the other hand, show nearly identical values for the u components and v components. The pairs 4243-4301, 4312-4332,4301-4342, and 4243-4342 show nearly identical values for the coherence estimates for both components. Of these, only 4301-4342 and 4243-4342 are clearly separated by the ridge. We thus get the picture of a velocity field with many small scales of motion. At horizontal separations greater than about 30 km., there is virtually no significant coherence, indicating that the velocity field must possess some scales of motion smaller than 30 km. This is not surprising; when a quasigeostrophic flow impinges on a bottom containing roughness scales smaller than the scale of the flow, we

expect the bottom to act as a forcing, thus producing (initially at least) scales of motion in the flow that resemble scales in the bottom roughness. When we look back at Figure 1, we see that Array-2 has an abundance of these small scales in the bottom roughness of order 10 to 50 km. It is thus possible that bottom effects are being observed.

A more graphic view of these coherences is given in Figures 40 and 41. The coherences have been plotted over their position in the array (see Figure 1 for corresponding topography). Figure 40 shows the u components. A positive phase angle implies that the tip of the arrow leads the tail, and conversely. The plot of the u components shows generally significant coherence, with the largest separation (424-434) giving the lowest value of coherence and the smallest separation (424-430) giving the largest. Phase angles are such that eastward instruments usually lead westward ones in phase. One of the two exceptions is the pair 424-431: instrument 4243, to the west of 4312, shows a phase lead of 15.5°; the other is the pair 4243-4332, where 4243 leads 4332 by 4.4°. We must remember that mooring 424 is a surface mooring, and velocities measured from it may be contaminated due to surface wave action. The plot for v coherences is in Figure 41. This plot shows more variation than for the u components. The smallest horizontal separation, 424-430,

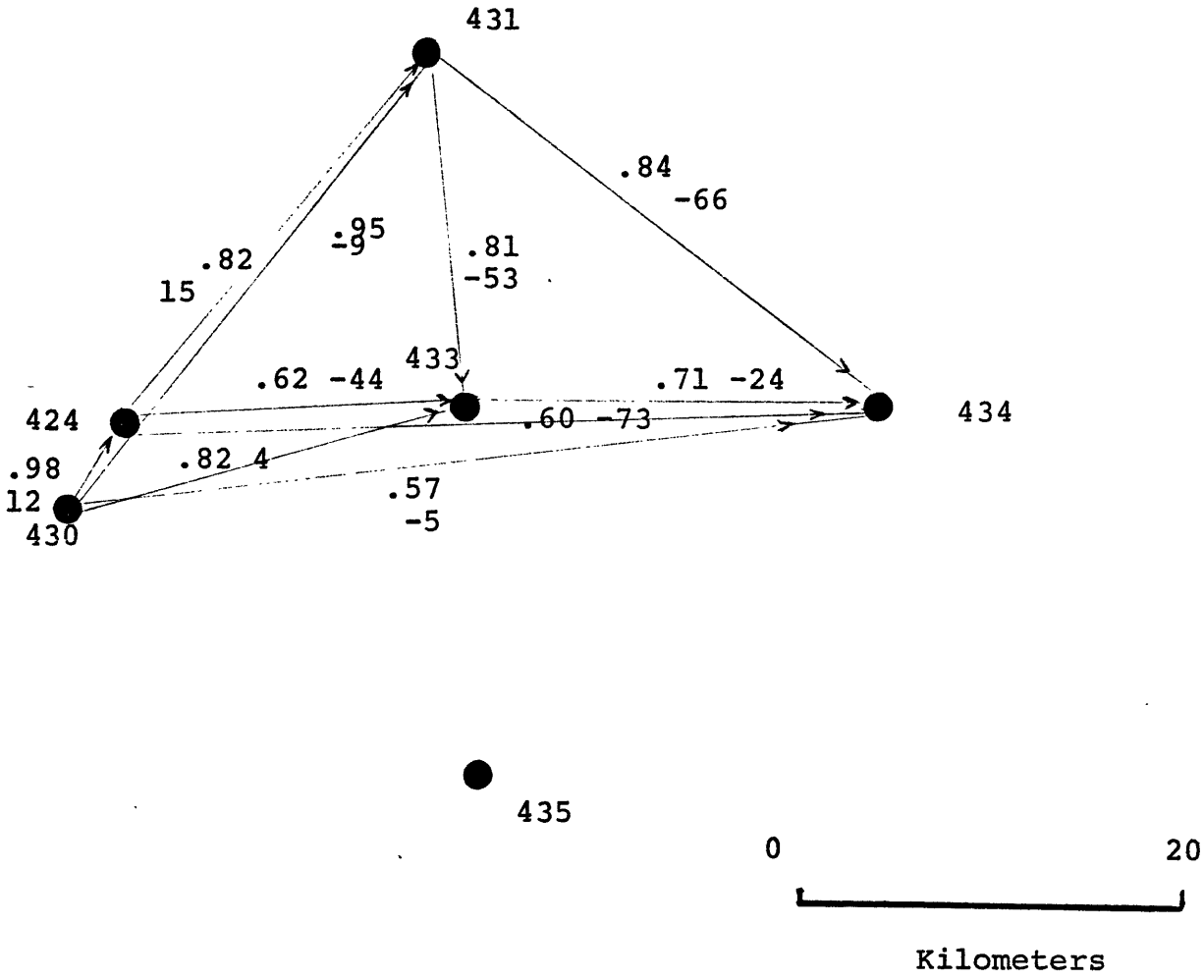
431
.84
-66
.95
-9
.82
15
.81
-53
433
.62 -44
.71 -24
424
434
.60 -73
.98
12
.82 4
.57
-5
430
435
0
20
Kilometers

FIGURE 40

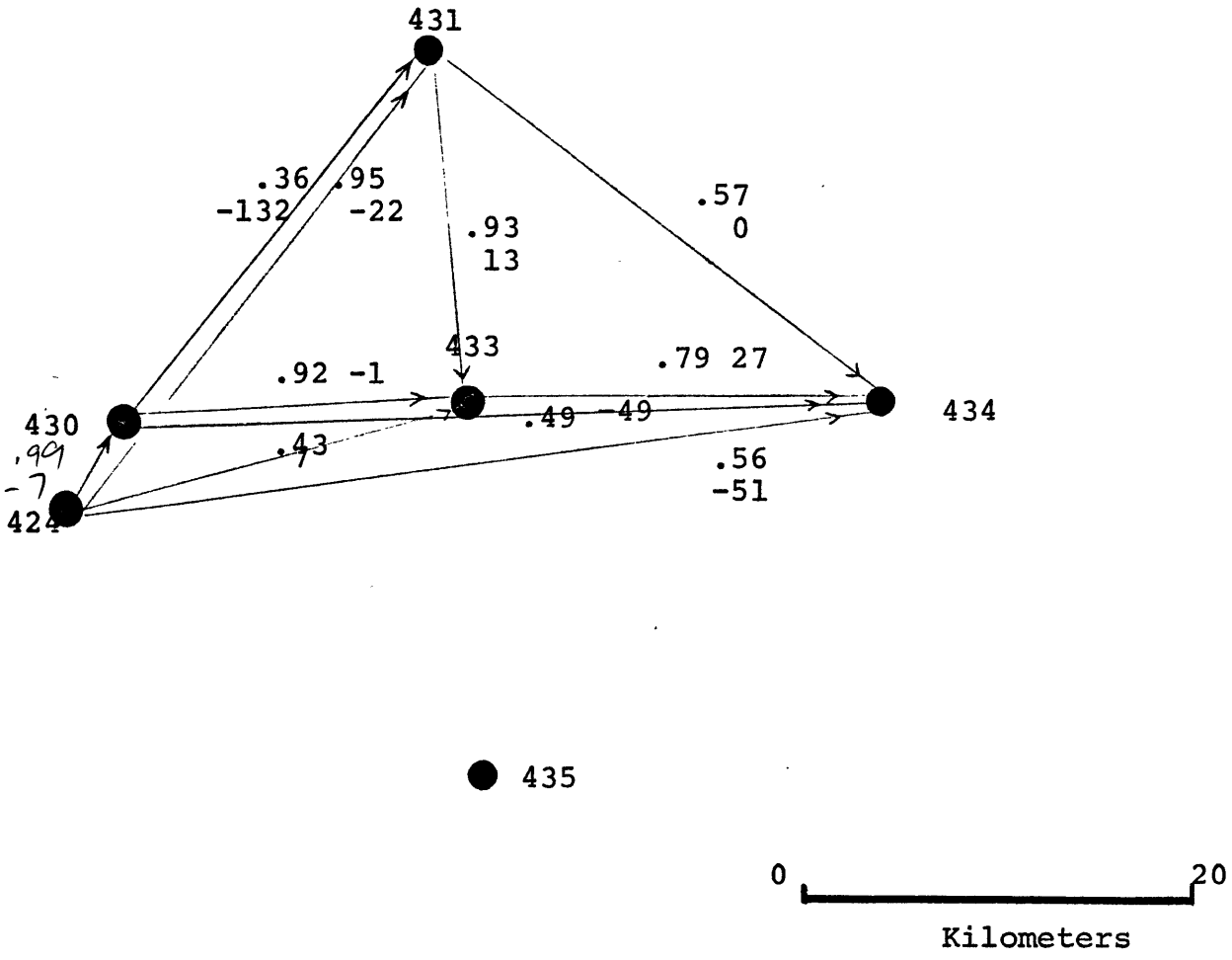
431
.36 .95
-132 -22
.93
13
.57
0
433
.92 -1
.79 27
430
.99
-7
424
.43
.49 -49
.56
-51
434
435
0
20
Kilometers

FIGURE 41

shows the highest coherence. However, several other separations give coherences below the significance level. The pair 424-431 shows a very small coherence (.3) although there are no obvious topographic features separating these instruments. Coherence across the ridge is again small. No obvious pattern emerges from the phase angles, either. There seems to be no directional preference for leads or lags.

One interesting facet of the coherence map in Figures 40 and 41 is the calculated coherence between instruments 4312 and 4332. In both components the coherence is high (.8,u;.9,v) in spite of the presence of a seamount between the instruments (see Figure 1 for topographic details). Of course, the summit of the seamount is approximately 800 m. below the level of the current meters. However, elsewhere in the array the bottom topography does appear to influence the flow above it over vertical distances of at least 800 m. In Chapter 4 a further comment will be made concerning this feature of the data.

In Figures 42 and 43 temperature-velocity and temperature-temperature coherences are plotted, using the temperature at instrument 4301 as a reference. We note that coherence between temperature and velocity is a monotonically decreasing function of separation, with the exception of temperature at 4301 and velocity at

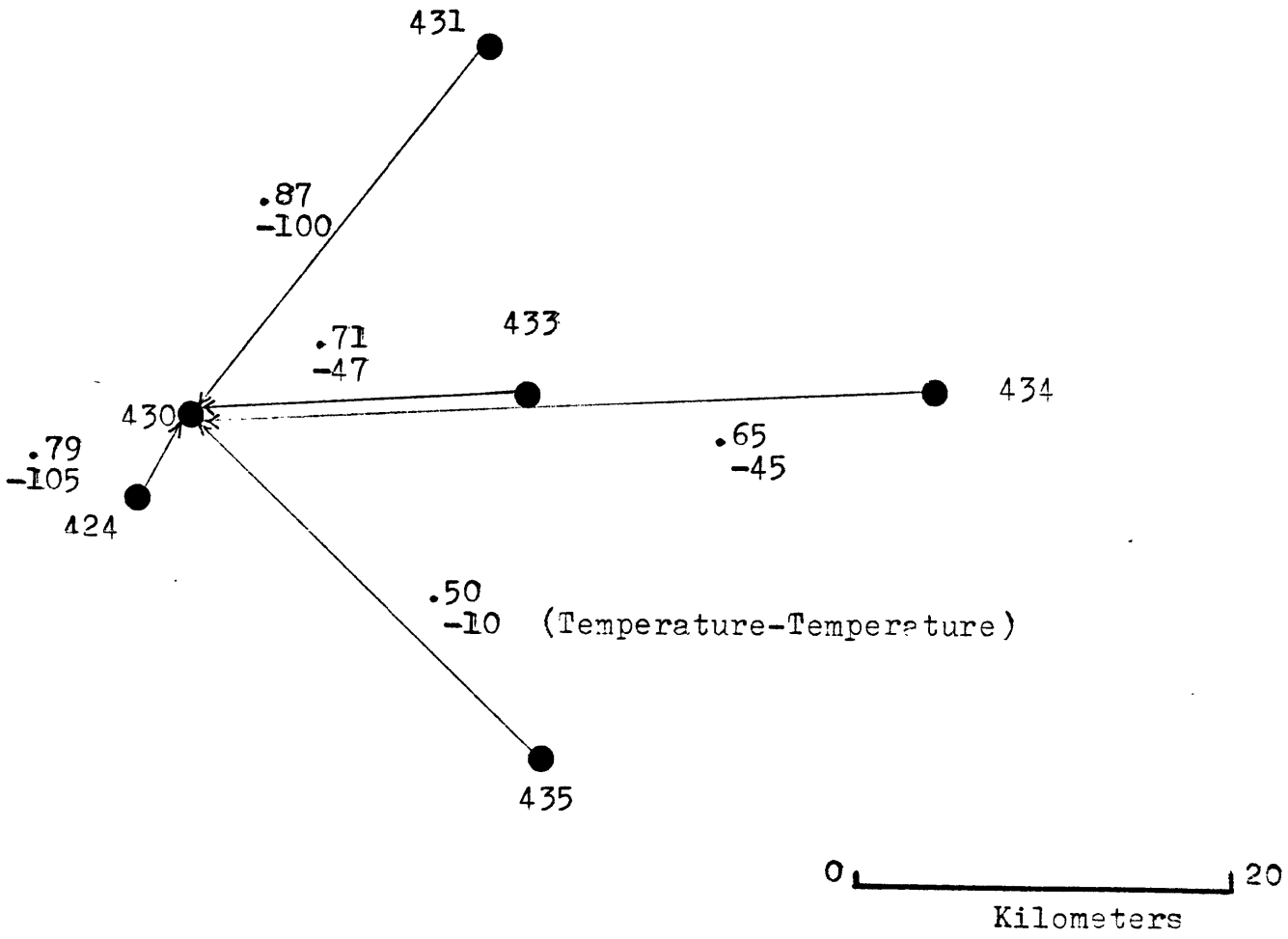

FIGURE 42

Temperature-Velocity Coherence Referenced to the Temperature at Instrument 4301

U Components

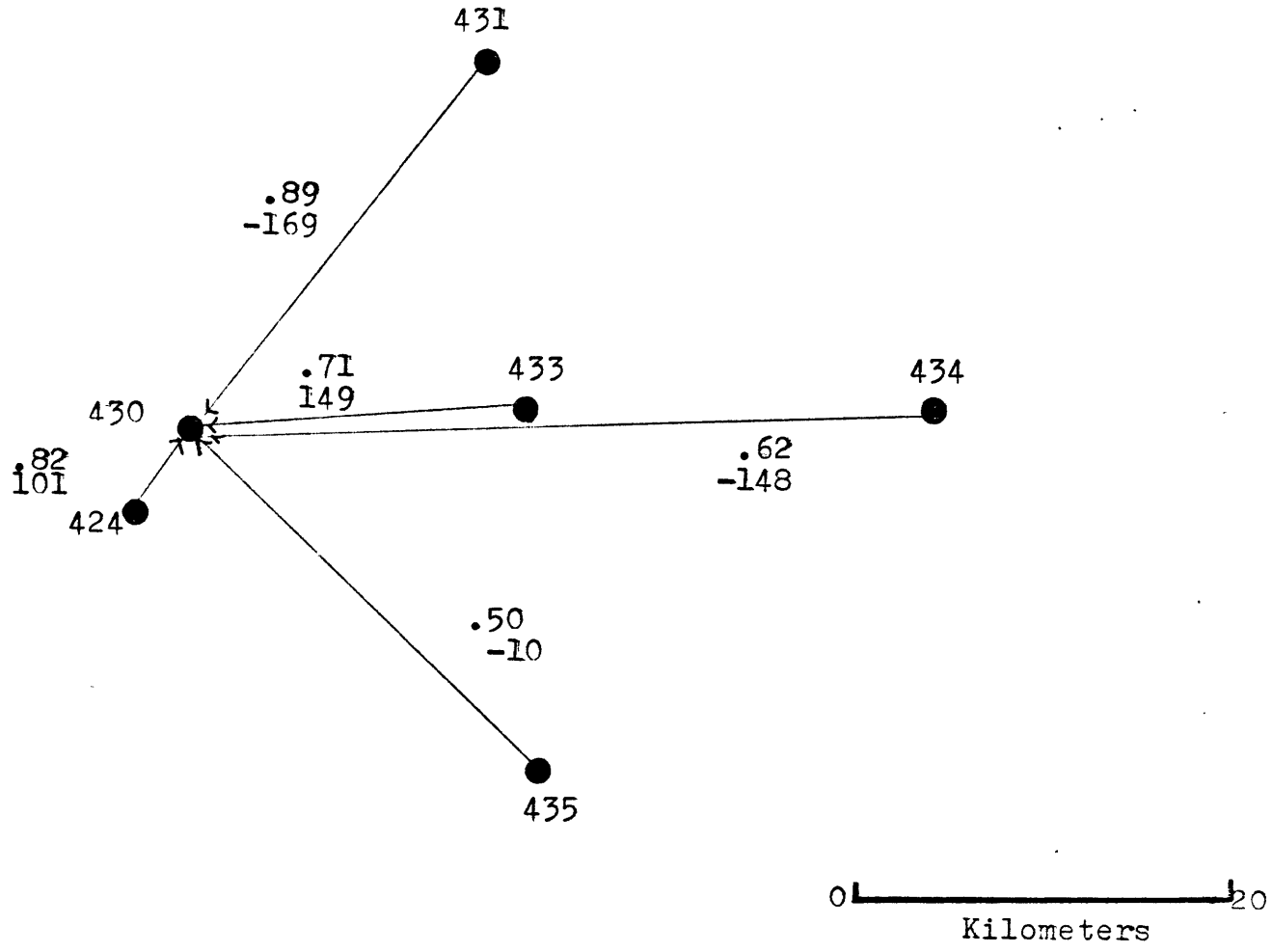

FIGURE 43

Temperature-Velocity Coherence Referenced to the Temperature at Instrument 4301
V Components

4243 at a separation of 4 km. It has been previously noted that some coherences referenced to 4243 have given anomalous values; this has been attributed to the fact that mooring 424 is a surface mooring. We must use caution when comparing velocity-velocity coherence, temperature-temperature coherence, and temperature-velocity coherence. Nevertheless, the plots of temperature in Figures 31 and 32 show strong variability at the end of the experiment west of the ridge, but none east of it as has been previously noted, so the low value of temperature-temperature coherence is not unreasonable when compared to the other calculations. It is difficult to interpret the meaning of phase angles in a temperature-velocity coherence calculation. However, the temperature-temperature calculation shows 4354 leading 4301 by 10° (which is probably not statistically different from zero). Looking at the v component-temperature coherence, we note a similar pattern. Once again the coherence between the temperatures across the ridge is lower than any of the temperature-velocity coherences. Similar plots are shown in Figures 44 and 45 using temperature at 4354 as a reference.

The amount of data involved in these calculations is probably to little to use in making detailed conclusions. Some features of the data do emerge, however.

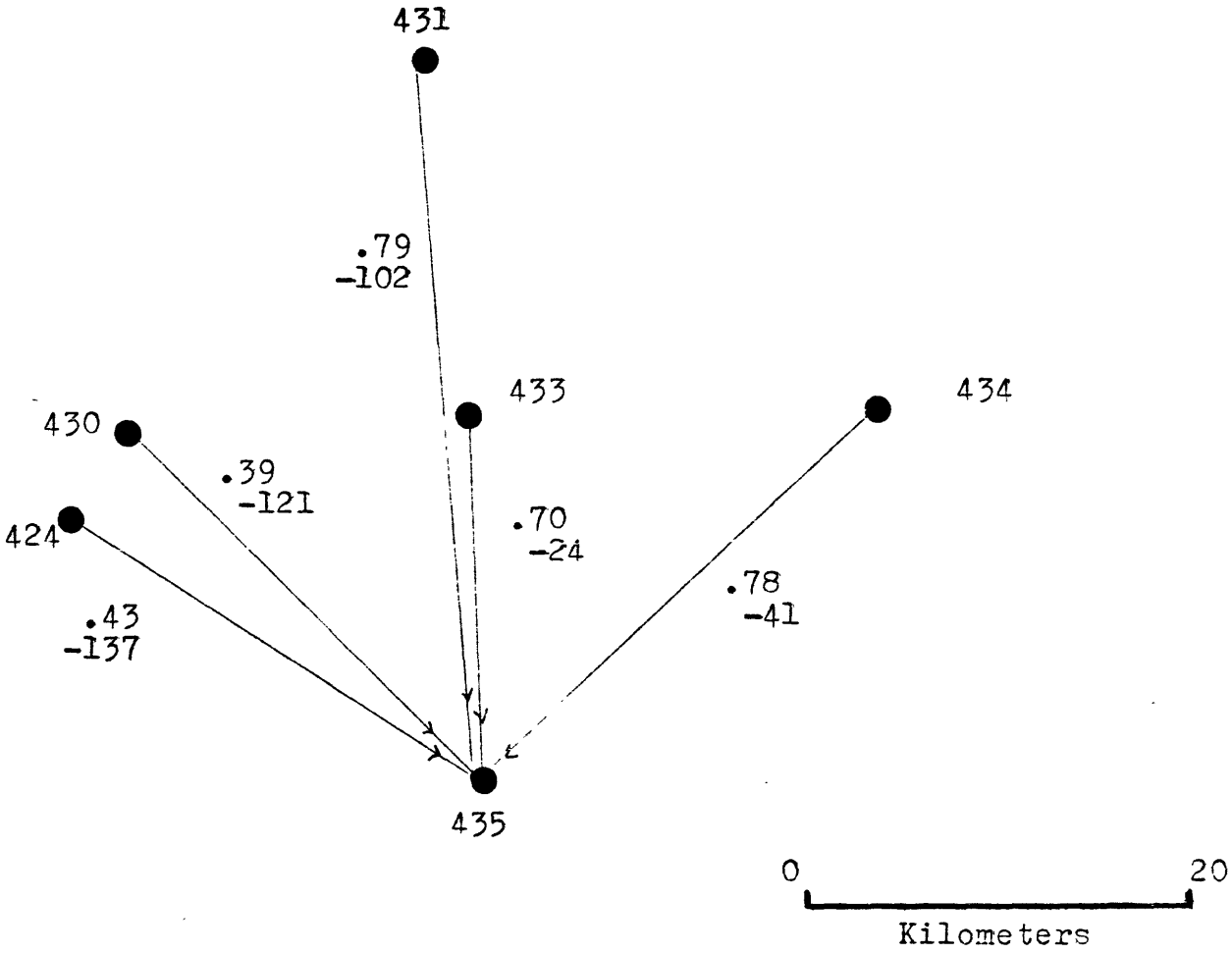

FIGURE 44

Temperature-Velocity Coherence Referenced to the

Temperature at Instrument 4354

U Comp.

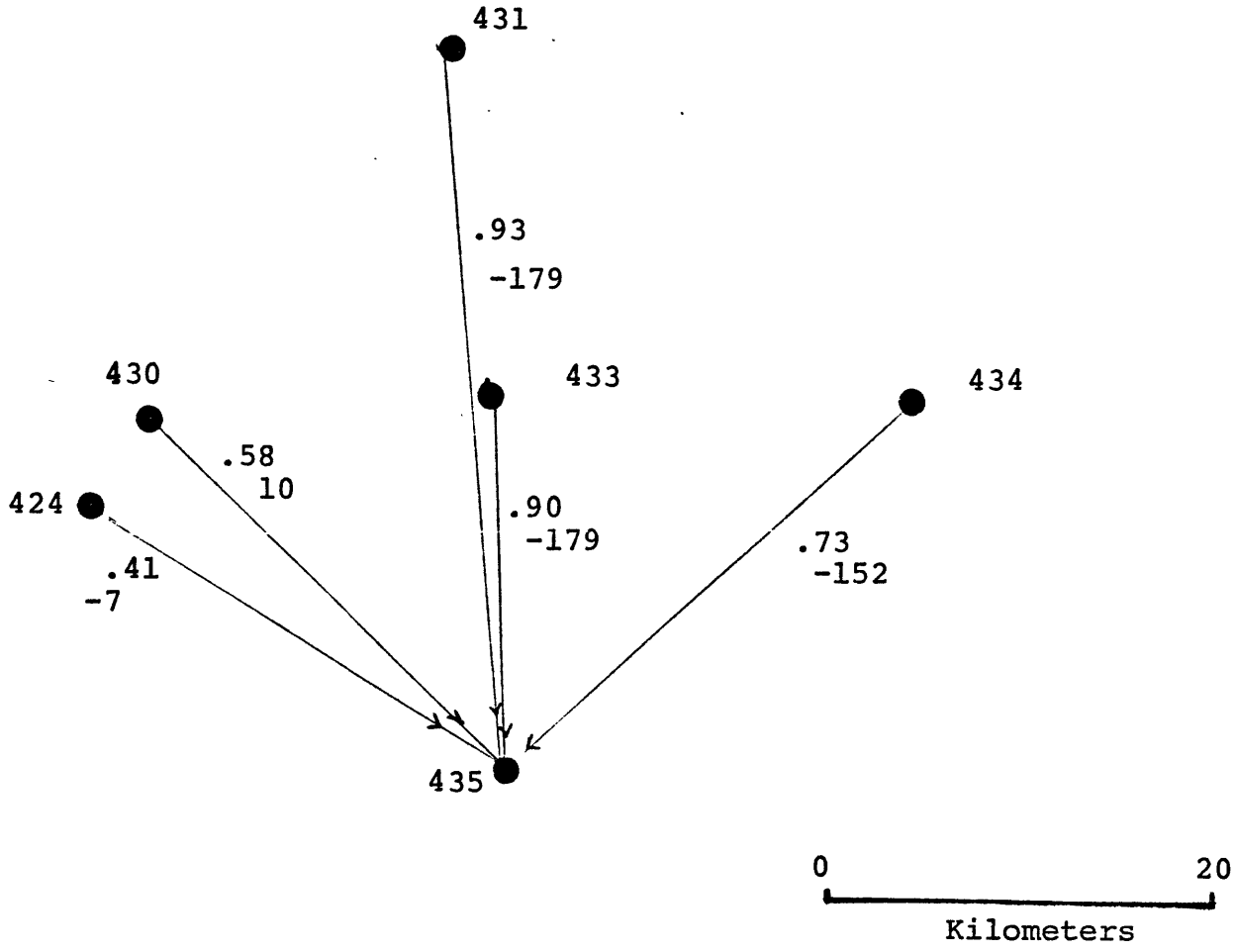

FIGURE 45

Temperature-Velocity Coherence Referenced to the Temperature at Instrument 4354

V Comp.

In Arrays-1 and 3 there was no similar pattern of coherences between instruments at 4000 m. Indeed, over the smooth topography coherences at separations of 30 to 50 km. were invariably significant.

CHAPTER 4--THEORETICAL CALCULATIONS

Effects of a Seamount Chain

We wish to investigate possible explanations for the major features of the data. The most obvious phenomenon requiring explanation is the lack of similarity of records separated by the ridge, evidenced from the coherence calculations in Chapter 3. The small amount of data available from the experiment makes any theory somewhat speculative; however, it is possible to estimate parameters such as scales of topography, horizontal velocity scales, and time scales. Of course, there is only one measurement above 4000 m., so the available data on vertical shear is only minimal, and there is no information about the density field. Nevertheless, it is useful to try to fit the information at our disposal into a simple theoretical framework. Hopefully this can serve as a guide in planning future experiments.

We can picture the flow in this area as a low frequency ($\ll f$), long scale ($\sim$300 km.) quasigeostrophic process encountering some bottom topography with length scales smaller than the length scales of the fluid motion. The bottom topography thus may act only as a perturbation on the main flow. Prandtl (1952) proposed that for quasigeostrophic flows, motion induced by small scales at a fluid boundary will penetrate to a distance of $\frac{fL}{N}$ into the fluid. This is just the Rossby

radius of deformation. Here f is the Coriolis parameter, L the horizontal length scale of the topography, and N a typical Brunt-Vaisala frequency. This is only a rough estimate: effects due to sheared currents are ignored, the exact form of the bottom topography is ignored, time dependence and possible instabilities are ignored. However, data to study such topographically induced phenomena are sparse, so Prandtl's idea may be a reasonable starting point.

The Brunt-Vaisala frequency in the MODE area is depth dependent; averaged over the water column, $\frac{N}{f} \sim 10$. For an individual seamount, such as that near current meter 4332 (see Figure 1), we can estimate $L_{SM} \sim 5$ km. For a chain of seamounts such as that running through the Array-2 area we estimate $L_{CH} \sim 40$ km. Thus we have approximate penetration into the fluid of

$$H_{SM} \sim \frac{5\,\text{km}}{10} = 500 \text{ meters}$$

for effects induced by an individual seamount, and

$$H_{CH} \sim \frac{40\,\text{km}}{10} = 4000 \text{ meters}$$

for effects induced by the ridge chain as a whole. We also see that bottom induced effects are felt at the surface for topographic length scales greater than about 50 km.

These simple results can be somewhat enlightening. In Chapters 2 and 3 we noted a drop in coherence across

the ridge. From the simple calculation above we expect the ridge to induce scales of motion into the fluid that penetrate 4000 m. aloft, or to near the bottom of the main thermocline. It is conceivable that this topographically induced motion effectively divides the Array-2 region into two regiemes, one east of the ridge and one west of it. West of the ridge a strong southward current was observed as high in the column as 3700 m. above the bottom, so perhaps the deformation radius can be used to estimate bottom induced effects here.

Hogg (1973) has proposed a more elaborate model of topographically induced processes. He considers the effects of circularly symmetric topography on a steady geostrophic current. The current may be vertically sheared although flow reversals in the velocity profile upstream of the topography are not allowed. For cases such that $\frac{NH}{fL} \sim 1$, where H is now the water depth, Hogg finds that a closed streamline region (a Taylor column) always forms over the bottom bump. The degree of vertical penetration of these closed streamlines depends upon the amount of nonlinearity (the Rossby number), the height of the bottom topography, and the form of the upstream vertical shear.

Such closed streamline regions may be present in the Array-2 area. However, it is doubtful if any meaningful

conclusions could be drawn by applying Hogg's theory. His theory is only concerned with steady flow, and the velocity field in the MODE area is strongly time dependent. In addition, the form of the local bottom topography in the MODE-0 Array-2 area is far from circularly symmetric. Perhaps the most serious objection to interpreting the data via Hogg's theory is the form of the velocity profile in the MODE area. Data presented by Stommel (1972) consistently shows a flow reversal near a depth of 1200 m., thus violating one of Hogg's most crucial assumptions. Bryan (1973) has attempted a numerical model of flow in the Array-2 area. He assumed a steady flow from the north and used real bottom topography digitized on a 128 by 128 grid. His results showed no closed streamline regions induced by the bottom topography. However, as Bryan points out, his attempts to reproduce features in the data were not too encouraging.

It appears that future experiments are necessary to improve the quality and quantity of measurements so that we may better model the effects of bottom topography on the mid-ocean circulation. The small amount of data currently available suggests that flow patterns are sufficiently complicated that no existing model can describe them.

Near Bottom Effects

In Figures 46 and 47 unaveraged Fourier coefficients from current meters on moorings 424 and 430 have been plotted. On mooring 424 the section of record used was from February 20 to April 20, 1972. On mooring 430 the records cover the interval from March 26 to May 10, 1972. These portions of the complete records were chosen because of the presence of apparent bottom intensification during these time intervals. We see that on mooring 424, all records show a dominant peak in the Fourier coefficients at a period near 60 days. The v components at 4000 m. show the highest peak at this frequency, the u components at 1500 m. the lowest. Away from the spectral peak, at higher frequencies, we note the general levels of the Fourier coefficients at 1500 and 4000 m. fall off with increasing frequency. At 1500 m., and to a lesser extent at 4000 m., the Fourier magnitudes quickly reach some very low level as frequency increases, presumably near the noise level of the instrument, and then remain fairly constant at this level. At 4000 m. peaks in the Fourier coefficients occur at periods of near 15 days, and then reach the noise level as at 1500 m. However, at a depth of 5000 m. peaks in the Fourier coeffients occur at periods as short as seven days, and throughout the band from 7 to 20 days the Fourier

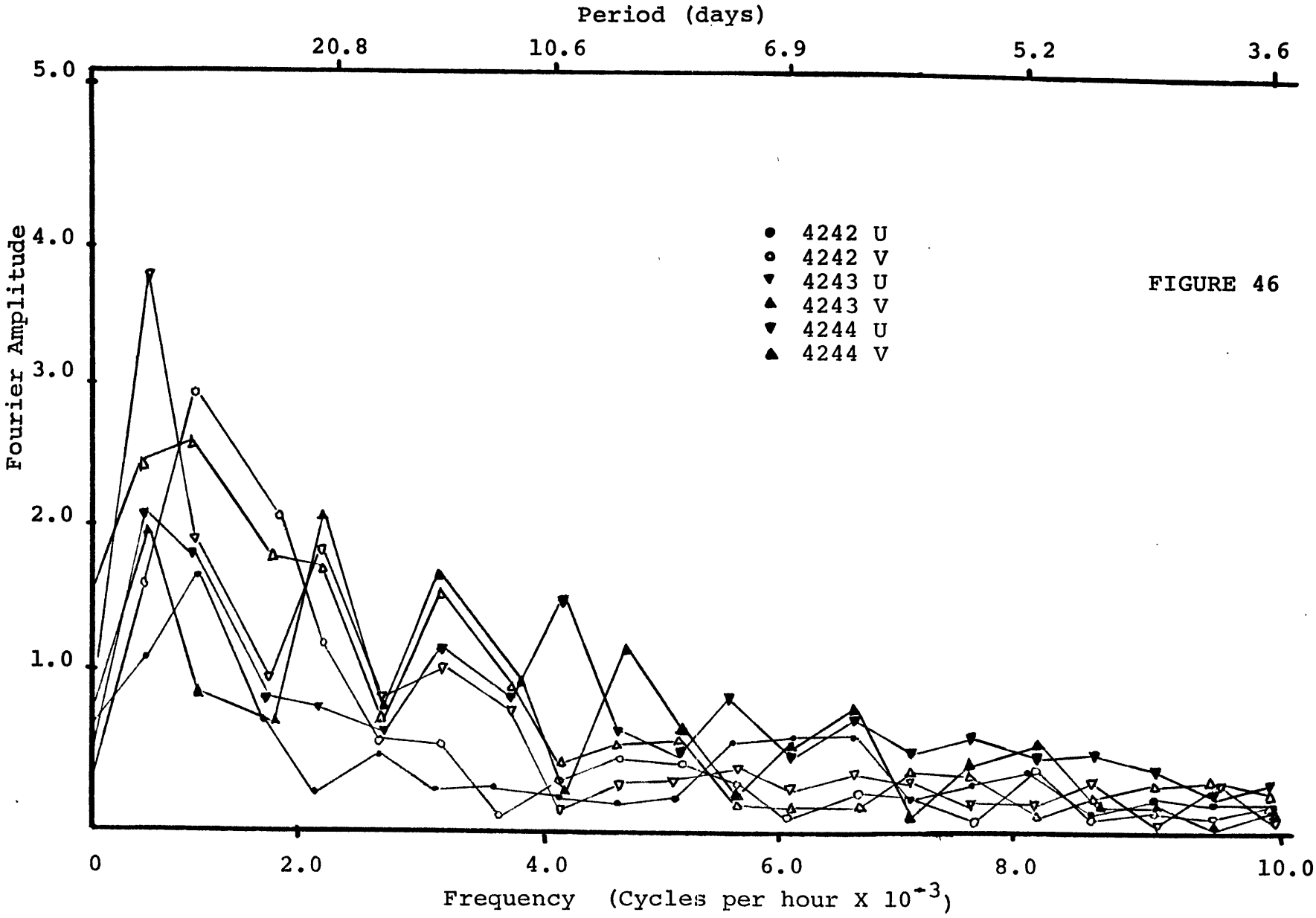
Period (days)
20.8
10.6
6.9
5.2
3.6
5.0
4.0
3.0
2.0
1.0
Fourier Amplitude
4242 U
4242 V
4243 U
4243 V
4244 U
4244 V
0
2.0
4.0
6.0
8.0
10.0
Frequency (Cycles per hour X 10^{-3})

FIGURE 46

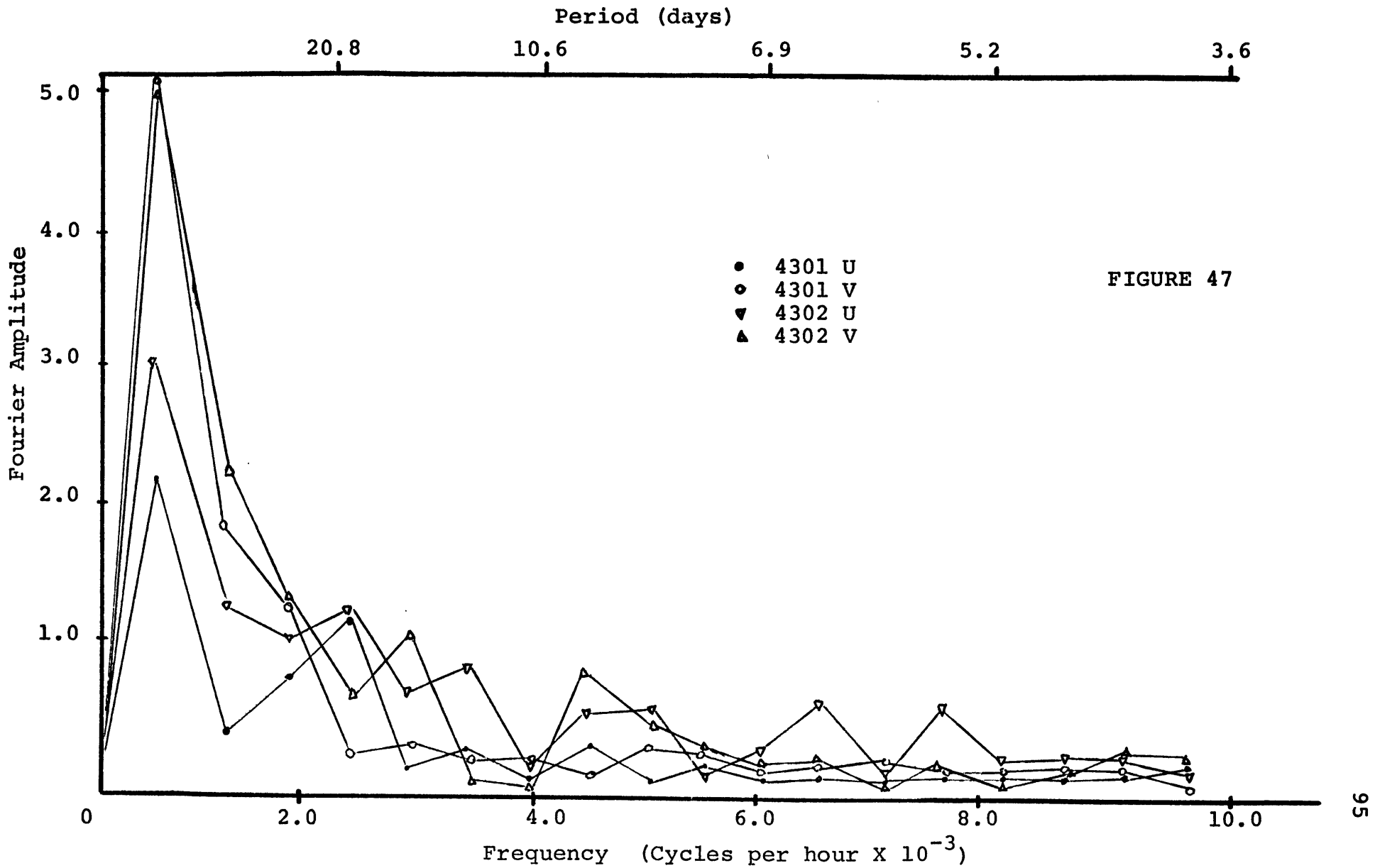
Period (days)
20.8
10.6
6.9
5.2
3.6
5.0
4.0
3.0
2.0
1.0
Fourier Amplitude
4301 U
4301 V
4302 U
4302 V
0
2.0
4.0
6.0
8.0
10.0
Frequency (Cycles per hour X 10^{-3})

FIGURE 47

amplitudes at 5000 m. are larger than those at 1500 or 4000 m. Of course, there is no averaging involved in presenting these coefficients, so individual peaks may not be significant. It is clear, however, that the average amplitude of the coefficients at 5000 m. is greater by at least a factor of two than the amplitudes at 4000 and 1500 m. On mooring 430 we note a similar pattern. The amplitude of the main peak, near a period of 60 days, is virtually the same in the v components at both 4000 and 5000 m. The amplitudes of the main peak in the east components is slightly greater at 5000 m. than at 4000 m. At frequencies greater than this main peak frequency, the amplitudes at 5000 m. are clearly consistently greater by a factor of at least two than the amplitudes at 4000 m. Thompson (1973) has noted similar bottom effects in this frequency band at Woods Hole's Site D, near 39°N 70°W on the New England continental slope.

One simple model that might be applicable to this apparent bottom intensification is that proposed by Rhines (1971). He showed that the presence of a sloping bottom in a rotating stratified fluid causes low frequency motion to be trapped to the bottom. Physically, as Suarez (1971) has pointed out, this occurs so as to release the ocean interior from the constraints imposed by the bottom topography. Near the bottom there is a

response generated due to the effective forcing by the bottom topography; however, in a fluid where $\frac{NH}{fL} \sim 1$ the response is confined near the bottom because of the strong stratification.

We can construct a simple model for these observations by using the same general equations that Rhines did. However, Rhines was interested in the case of a constant Brunt-Vaisala frequency because it was the simplest case to consider analytically. In reality the Brunt-Vaisala frequency is not constant with depth in the area of the Array-2 observations, so we will formulate our equations for the more general case.

We can begin with the dimensional equations of motion:

$$\frac{\partial u^*}{\partial t^*} + \underset{\sim}{u}^* \cdot \nabla u^* - f v^* = -\frac{1}{\rho_0} \frac{\partial p^*}{\partial x^*} \tag{1}$$

$$\frac{\partial v^*}{\partial t^*} + \underset{\sim}{u}^* \cdot \nabla v^* + f u^* = -\frac{1}{\rho_0} \frac{\partial p^*}{\partial y} \tag{2}$$

$$\frac{\partial w^*}{\partial t^*} + \underset{\sim}{u}^* \cdot \nabla w^* = -\frac{1}{\rho_0} \frac{\partial p^*}{\partial z^*} - \frac{\rho^*}{\rho_0} g \tag{3}$$

$$\frac{\partial \rho^*}{\partial t^*} + \underset{\sim}{u}^* \cdot \nabla \rho^* = 0 \tag{4}$$

$$\nabla \cdot \underset{\sim}{u}^* = 0 \tag{5}$$

We lose no loss of generality if we apply a rigid lid to our model ocean. At the bottom (assumed to be a constant slope shelving to the east) there is a kinematic condition stating that there can be no normal flow to the bottom. These two boundary conditions can be

stated as

$$w^* = 0 \qquad z = 0 \tag{6}$$

$$\underset{\sim}{u}^* \cdot \nabla(z-h) = 0 \qquad z = -H + \epsilon x \tag{7}$$

where we have used a righthand coordinate system (x east, y north, z vertically upward) with corresponding velocity components (u,v,w). p^* denotes the pressure and ρ^* the density. H is the mean ocean depth. A * has been used to denote a dimensional quantity.

We will assume a constant value for the Coriolis parameter, f. Also, we assume the Boussinesq approximation holds in our model ocean; that is, the pressure and density may be expanded as

$$\tilde{p}^* = p^*_{(z)} + p^*(x^*, y^*, z^*, t^*) \tag{8}$$

$$\tilde{\rho}^* = \rho_0 + \bar{\rho}^*(z^*) + \rho^*(x^*, y^*, z^*, t^*) \tag{9}$$

The Boussinesq approximation implies that we will neglect variations in $\tilde{\rho}^*$ with respect to ρ_0 except in the buoyancy terms.

We can now nondimensionalize the problem as follows:

put $(u^*, v^*) \rightarrow U(u,v)$

$w^* \rightarrow W, w$

$(x^*, y^*) \rightarrow L(x,y)$

$z^* \rightarrow Hz$

$$t^* \to \gamma^{-1} f^{-1} \tau$$

$$p^* \to \rho_0 f L U p$$

and thus

$$\rho^* \to \frac{\rho_0 f L U}{gH} \rho$$

Putting these newly defined quantities in the original momentum equations, we get a new set of nondimensional equations

$$\gamma \frac{\partial u}{\partial \tau} + Ro\, \underline{u} \cdot \nabla u - v = -\frac{\partial p}{\partial x} \tag{10}$$

$$\gamma \frac{\partial v}{\partial \tau} + Ro\, \underline{u} \cdot \nabla v + u = -\frac{\partial p}{\partial y} \tag{11}$$

$$\gamma \frac{\partial w}{\partial \tau} + Ro\, \underline{u} \cdot \nabla w = -\frac{\partial p}{\partial z} - \rho \tag{12}$$

$$\gamma \frac{\partial \rho}{\partial \tau} + Ro\, \underline{u} \cdot \nabla \rho - S^2 \lambda^2 w = 0 \tag{13}$$

$$\nabla \cdot \underline{u} = 0 \tag{14}$$

with boundary conditions

$$w = 0 \qquad z = 0 \tag{15}$$

$$w = \gamma u \qquad z = -1 + \gamma x \tag{16}$$

In these equations we have defined Ro as the Rossby number; $S = \frac{N}{f}$; $\lambda = \frac{H}{L}$ and is the aspect ratio; $\gamma = \epsilon \frac{\epsilon}{H}$. We can rewrite equation (13) by noting that $S^2 \lambda^2 = \frac{N^2 H^2}{f^2 L^2}$. In general, N=N(z), so let $N = N_0 n(z)$ where N_0 is the maximum value of the Brunt-Vaisala frequency. We then have

$$\gamma \frac{\partial \rho}{\partial \tau} + Ro\, \underline{u} \cdot \nabla \rho - B_0^2 n^2(z)\, w = 0 \tag{13}$$

where n(z) is a nondimensional function ranging in value from zero to one, describing the Brunt-Vaisala frequency distribution. We have defined $S_0 = \frac{N_0}{f}$ and $B_0 = \lambda S_0$.

Making assumptions that

$$Ro \leq O(\gamma) \qquad \gamma \ll 1$$

we can expand all variables in powers of γ. From (10) and (11) we then have at lowest order,

$$v^{(0)} = p^{(0)}_x \qquad u^{(0)} = -p^{(0)}_y$$

which just states that the horizontal velocity field is geostrophic at lowest order in γ. From (12), (13), and (14) we have

$$\frac{\partial p}{\partial z} = -\rho^{(0)} \quad ; \quad B_0^2 n^2(z) w^{(0)} = 0$$

which states that at lowest order in γ, the ocean is hydrostatically balanced. We infer that $w^{(0)} = 0$, and the continuity equation becomes

$$\frac{\partial u^{(0)}}{\partial x} + \frac{\partial v^{(0)}}{\partial y} = 0$$

Thus the velocity field is horizontally nondivergent at this order. At order γ we have

$$\frac{\partial u^{(0)}}{\partial T} + \left(\frac{R_0}{\gamma}\right) \underline{u}^{(0)} \cdot \nabla u^{(0)} - v^{(1)} = -p^{(1)}_x \tag{17}$$

$$\frac{\partial v^{(0)}}{\partial T} + \left(\frac{R_0}{\gamma}\right) \underline{u}^{(0)} \cdot \nabla v^{(0)} + u^{(1)} = -p^{(1)}_y \tag{18}$$

$$\frac{\partial p^{(1)}}{\partial z} - \rho^{(1)} = 0 \tag{19}$$

$$\frac{\partial \rho^{(0)}}{\partial T} + \left(\frac{R_0}{\gamma}\right) \underline{u}^{(0)} \cdot \nabla \rho^{(0)} - B_0^2 n^2(z) w^{(1)} = 0 \tag{20}$$

$$\frac{\partial u^{(1)}}{\partial x} + \frac{\partial v^{(1)}}{\partial y} + \frac{\partial w^{(1)}}{\partial z} = 0 \tag{21}$$

so that at this order there are deviations from geostrophic and hydrostatic balance, and the field is horizontally divergent. From (20) we find that

$$w^{(1)} = \frac{1}{B_0^2 n^2(z)} \left\{ \frac{\partial \rho^{(0)}}{\partial T} + \left(\frac{R_0}{\gamma}\right) \underline{u}^{(0)} \cdot \nabla \rho^{(0)} \right\} \tag{22}$$

or, substituting for the density in terms of pressure,

$$w^{(1)} = \frac{1}{B_0^2 n^2(z)} \left\{ -\frac{\partial}{\partial T}\left(\frac{\partial p^{(0)}}{\partial z}\right) + \left(\frac{R_0}{\gamma}\right) \underset{\sim}{u}^{(0)} \cdot \left(\frac{\partial p^{(0)}}{\partial z}\right) \right\} \tag{23}$$

Now, by taking $\partial/\partial y$ of (17) and $\partial/\partial x$ of (18) and adding to $\partial/\partial t$ of (23), after simplification and substitutions of the geostrophic velocities, we have

$$\frac{\partial}{\partial T}\left(\nabla_H^2 p^{(0)} + \frac{1}{B_0^2}\frac{\partial}{\partial z}\left(\frac{1}{n^2(z)}\frac{\partial p^{(0)}}{\partial z}\right)\right) + \left(\frac{R_0}{\gamma}\right)\left\{ J\left(p^{(0)}, \nabla_H^2 p^{(0)} + \frac{1}{B_0^2}\frac{\partial}{\partial z}\left(\frac{1}{n^2}\frac{\partial p^{(0)}}{\partial z}\right)\right)\right\} \tag{24}$$

where J( ) denotes the Jacobian of the bracketed quantity.

Our boundary conditions were

$$w = 0 \qquad z = 0 \tag{15}$$

$$w = \gamma u \qquad z = -1 + \gamma x \tag{16}$$

If $\gamma \ll 1$, we can linearize (16) around z=-1 to simplify. This is done by expanding both sides of (16) in a Taylor expansion in γ and equating terms. This just yields the

simplified bottom boundary condition of $w^{(1)} = u^{(0)}$ on z=-1. Using this, and substituting everywhere for velocity in terms of pressure in (15), we now have a complete system of equations to be solved:

$$\frac{\partial}{\partial T}\left(\nabla_H^2 p^{(0)} + \frac{1}{B_0^2}\frac{\partial}{\partial z}\left(\frac{1}{N^2(z)}\frac{\partial p^{(0)}}{\partial z}\right)\right) + \left(\frac{R_0}{\gamma}\right)\left\{J\left(p^{(0)}, \nabla_H^2 p^{(0)} + \frac{1}{B_0^2}\frac{\partial}{\partial z}\left(\frac{1}{N^2(z)}\frac{\partial p^{(0)}}{\partial z}\right)\right)\right\} \tag{25}$$

$$\frac{\partial}{\partial T}\left(\frac{\partial p^{(0)}}{\partial z}\right) = \left(\frac{R_0}{\gamma}\right) J\left(p^{(0)}, \frac{\partial p^{(0)}}{\partial z}\right) \qquad z = 0 \tag{26}$$

$$\frac{\partial}{\partial T}\left(\frac{\partial p^{(0)}}{\partial z}\right) = B_0^2 N^2(z) p_y^{(0)} + \left(\frac{R_0}{\delta}\right) J\left(p^{(0)}, \frac{\partial p^{(0)}}{\partial z}\right) \qquad z = -1 \tag{27}$$

If $\frac{R_0}{\gamma} \ll 1$ these equations can be linearized. A realistic Brunt-Vaisala frequency profile is

$$N(z) = N_0 e^{\alpha z}$$

The equations to solve then become

$$\frac{\partial}{\partial T}\left(\nabla_H^2 p^{(0)} + \frac{1}{B_0^2}\frac{\partial}{\partial z}\left(e^{-2\alpha z} p_z\right)\right) = 0$$

$$\frac{\partial}{\partial T}\left(\frac{\partial p^{(0)}}{\partial z}\right) = 0 \qquad z = 0$$

$$\frac{\partial}{\partial T}\left(\frac{\partial p^{(0)}}{\partial z}\right) = B_0^2 e^{2\alpha z} p_y^{(0)} \qquad z = -1$$

Taking wavelike solutions with functional vertical dependence for pressure,

$$p = P(z)\, e^{i(kx + ly - \omega t)}$$

we get the set

$$\frac{d}{dz}\left(e^{-2\alpha z} P'(z)\right) - B_0^2 K^2 P(z) = 0$$

$$P'(0) = 0$$

$$P'(-1) = -\frac{l}{\omega} B_0^2 e^{-2\alpha} P(-1)$$

where $\kappa^2 = k^2 + l^2$.

Using the top and bottom boundary conditions together with the above differential equation, it can be shown that

$$P(z) = Ae^{\alpha z}\left\{I_1\left(\frac{B_0 K}{\alpha} e^{\alpha z}\right) + \frac{I_0(B_0K/\alpha)}{K_0(B_0K/\alpha)} K_1\left(\frac{B_0 K}{\alpha} e^{\alpha z}\right)\right\}$$

and that the dispersion relation is

$$\omega = -B_0 l e^{-\alpha}\left[\left(\frac{I_0(B_0K/\alpha)}{K_0(B_0K/\alpha)}K_1\left(B_0K/\alpha e^{-\alpha}\right) + I_1\left(\frac{B_0K}{\alpha}e^{-\alpha}\right)\right)\Big/\left(K\left\{I_0\left(\frac{B_0K}{\alpha}e^{-\alpha}\right) - \frac{I_0\left(\frac{B_0K}{\alpha}\right)}{K_0\left(\frac{B_0K}{\alpha}\right)}K_0\frac{B_0K}{\alpha}e^{-\alpha}\right\}\right)\right]$$

where I_0, K_0, I_1, K_1, are modified Bessel functions of zero and first order. In order to better interpret this dispersion relation we can go back to dimensional quantities to find that

$$\sigma = \epsilon N_0 e^{-\alpha H}\sin\theta\left\{\frac{\left(I_0(\Omega)/K_0(\Omega)\right)K_1(\Omega e^{-\alpha H}) + I_1(\Omega e^{-\alpha H})}{\left(I_0(\Omega)/K_0(\Omega)\right)K_0(\Omega e^{-\alpha H}) - I_0(\Omega e^{-\alpha H})}\right\}$$

where σ is now the frequency in cycles/time, and $\Omega = \frac{N_0 K}{\alpha f}$. θ is the angle between the actual wave vector and east, measured in a counterclockwise manner.

We can now try to apply this simple model to the data. We note from Figure 1 that moorings 424 and 430 are located to the west of the ridge on a gently sloping plain. This relatively smooth sloping region extends approximately 30 km. to the west of the ridge where there are several small seamounts. The average slope in this smooth area between roughness features is of the order of 10^{-2}. If we take $N_0 = 3\,hr^{-1}$, $\alpha = 5.5\times10^{-4}\,m^{-1}$ (reasonable values for the MODE region below the seasonal thermocline) we can determine periods and wavenumbers of free waves in this area, assuming

that values of slope that we pick for the constant slope model are consistent with the actual geometry of the bottom. Table III gives periods and wavelengths of free waves calculated from the dispersion relation for various choices of slope.

Our data suggests that intensification near the ocean bottom in the Array-2 area does seem to occur. Clearly from the calculations in Table III for slopes greater than .009 there are a myriad of possible free waves available to us at wavelengths less than 100 km. Because of the complicated bottom topography, the theory constructed above is probably only marginally valid for wavelengths this large, because the smooth region in which we are applying the theory is only 50 km. square. In addition, the assumption of a constant Coriolis parameter fails for waves larger than 100 km.

There are several parameters measurable with moored current meters in a field of these waves: frequency, wavenumber, and vertical structure. Since the two moorings we are interested in are only 4 km. apart, they offer essentially a point measurement for wavelengths of 50 km. or greater. Thus since we really have no directional information about the waves, all calculations will assume that $\theta = \frac{\pi}{2}$, that is, that the waves are propagating to the north. This will then give us a lower bound on possible

TABLE III.

Periods and Wavelengths Calculated from the Dispersion Relation. $\theta = \frac{\pi}{2}$

Slope=.005

Period (days)	Wavelength (km.)
16	300
23	150
27	100
30	75
32	60
34	50
35	43
36	38
37	33
38	30
39	27

Slope=.011

7	300
10	150
12	100
14	75
15	60
15	50
16	43
17	38
17	33
17	30
18	27
18	25

TABLE III. (continued)

Slope=.015

Period (days)	Wavelength (km.)
5	300
8	150
9	100
10	75
11	60
12	43
13	30
14	19

Slope=.021

4	300
5	150
6	100
7	75
8	50
9	25
10	20

periods. Since vertical trapping is not a function of frequency but only of wavenumber, we can uniquely determine a wave if we know its frequency and vertical structure. We know the frequency band of interest from the Fourier coefficients. From the three current meters on mooring 424 we can attempt an estimate of the vertical structure. By knowing the vertical structure we can estimate the wavelength; this estimate can be compared to that calculated from the dispersion relation, and it is hoped that the two values of wavelength will be consistent.

The nondimensional vertical dependence of these bottom trapped waves previously calculated was

$$P(z) = Ae^{\alpha z}\left\{I_1\left(\frac{B_0 K}{\alpha}e^{\alpha z}\right) + \left(I_0(B_0 K/\alpha)/K_0(B_0 K/\alpha)\right)K_1\left(B_0 K/\alpha\, e^{\alpha z}\right)\right\}$$

Using this result, vertical trapping has been plotted for various wavelengths as a function depth in Figure 48. We have plotted $\frac{E(z)}{E(5000)}$ where z is the depth; E(z) is assumed proportional to the square of the vertical amplitude dependence given above. We note that shorter wavelengths are more effectively trapped to the bottom than longer ones. This is not unexpected: as wavelengths increase towards two pi times the internal radius of deformation, the influence of these waves is felt higher and higher in the water column. When this critical wavelength is reached the waves penetrate to the surface. For the waves considered here, the theory shows that very little influence of the bottom is felt above 2000 m. depth. Also plotted

on Figure 48 are the values of energy calculated from the data. This has been done as follows: from each instrument on moorings 424 and 430 Fourier magnitudes in the band of periods from 7 to 20 days have been squared and then added for both u and v components. The sum $E=\frac{1}{2}(P_{uu}+P_{vv})$ has been formed for each instrument, where $P_{uu}=\overline{|u|^2}$, $P_{vv}=\overline{|v|^2}$, and the resulting E(z) has been divided by E(5000) on its mooring. These calculations have been tabulated in Table IV. We have only a small number of points to plot from these calculations.

Looking again at Figure 48, we see that the two sets of data at 4000 m. fall at different locations: on mooring 424 the point plots nearest to the curve for a wavelength of 75 km. On mooring 430 the point is near to the curve for a wavelength of 38 km. The one point at 1500 m. from 4242 does not plot near any of the curves, which all have a value very near zero at this depth. At first this may seem to imply that the simple theory suggested here does not hold. However, there may be an explanation. This theory for bottom trapped waves includes only baroclinic effects. Any barotropic effects, or any noise in the measurement, will tend to make the data depart from a completely baroclinic field of motion as described by the theory. We note in the figure that if both the point from 4242 and 4243 were shifted to the left by .2, then the results would be in better agreement with the theory

FIGURE 48.

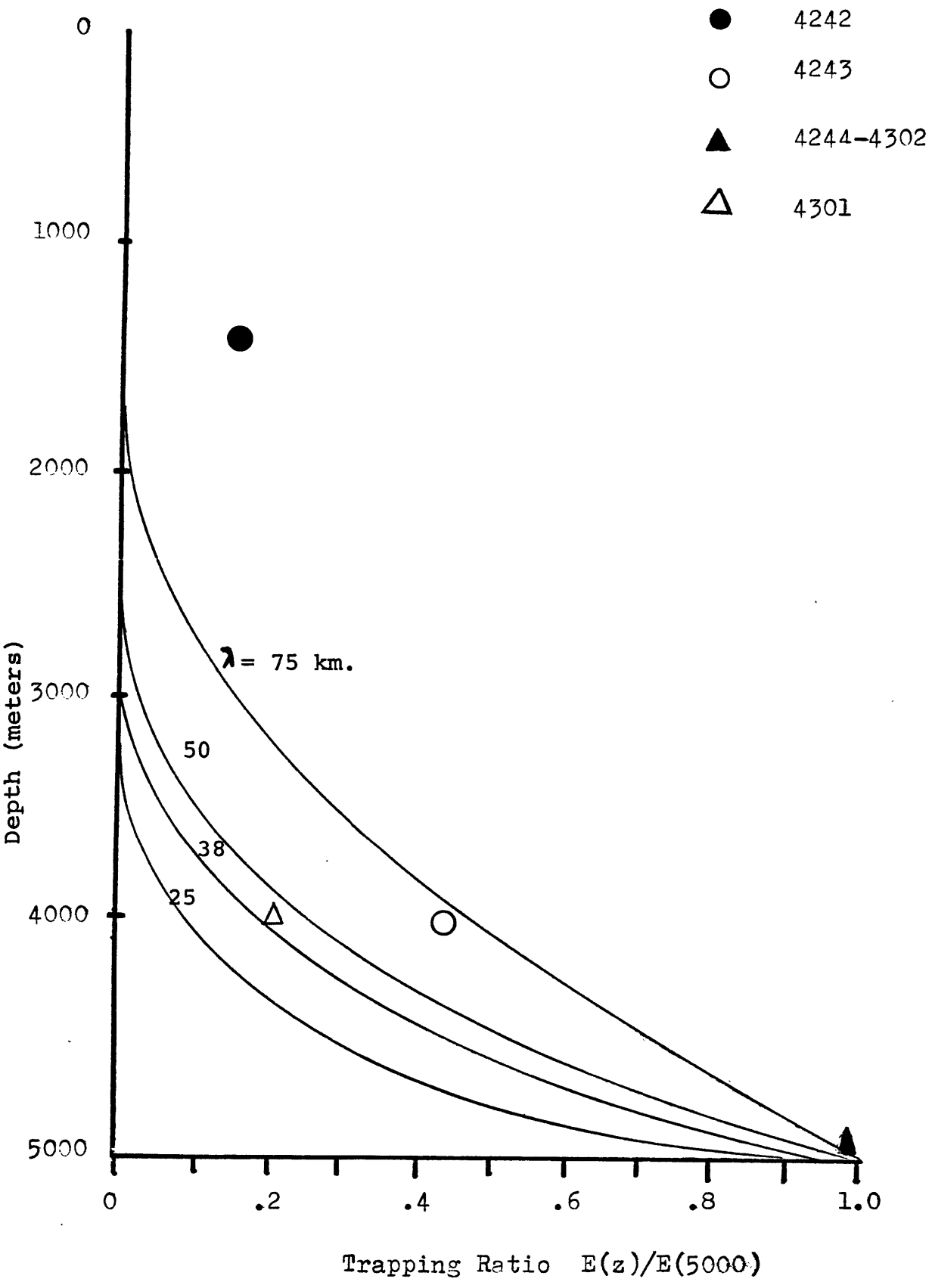
4242
4243
4244-4302
4301
0
1000
2000
3000
4000
5000
Depth (meters)
λ = 75 km.
50
38
25
0
.2
.4
.6
.8
1.0
Trapping Ratio E(z)/E(5000)

TABLE IV.

Normalized Energies in
Band of Periods 7-20 Days

Current Meter	Depth (m.)	P_{uu} $(cm/sec)^2$	P_{vv} $(cm/sec)^2$	$E(z)$ $(cm/sec)^2$	$\frac{E(z)}{E(5000)}$
4242	1500	2.08	4.57	3.33	.28
4243	4000	3.45	8.82	6.19	.49
4244	5000	13.60	11.51	12.55	1.00
4301	4000	1.96	0.35	1.15	.26
4302	5000	5.31	3.46	4.39	1.00

and more consistent with the values obtained from mooring 430. Then all four of the data points would tend to fall between wavelengths of 38 and 50 km.

We can estimate the barotropic signal needed to shift the curve this much by solving

$$\frac{E(4000) - E_{BAR}}{E(5000) - E_{BAR}} = \frac{E(4000)}{E(5000)} - .2$$

If we put E(5000)=12.5, E(4000)=6.1, we can solve for the barotropic part of the signal to be 3.6 $\frac{cm^2}{sec^2}$. This is just the amount that would be added to the total signal by a barotropic component, or noise level. of about 1.9 cm/sec, assuming this barotropic (noise) component is uncorrellated with the baroclinic signal. This explanation is only suggestive, of course. The apparent differences in the calculation between mooring 424 and 430 may be related to the fact that mooring 424 is a surface mooring while 430 is a subsurface type, but there is not enough data to say more.

There is, however, a hint that the wavelength is near 50 km. for the near bottom effects we are viewing in Array-2. This simple estimate is not unreasonable: when the mesoscale eddies encounter the rough bottom we can expect that part of the energy of the mesoscale is scattered into smaller scale motions near the bottom by the bottom roughness. Initially the distribution of length scales in these bottom motions should be similar

to the distribution of the length scales of the bottom topography. For waves with length scales of O(10 km.) as we may have here, there exist a plethora of topographic features of similar dimensions that may be possible generation sites. Interaction with other scales of motion may eventually destroy these near bottom motions. We have, of course, ignored nonlinearities in the theory by assuming $\frac{R_0}{\gamma} \ll 1$. In fact, for the cases considered here, $R_0 \sim \gamma$, so the waves are strongly nonlinear. It is encouraging that Rhines (1970) has found numerically that quasigeostrophic eddies on a rough bottom behave very similarly to waves, and even appear to obey a dispersion relation, when $R_0 \sim \gamma$, so linear dynamics may still have some meaning. In nonlinearities are to be studied in detail, numerical models are needed.

CHAPTER 5--SUMMARY AND DISCUSSION

Two phenomena have been investigated based on data taken in the Array-2 experiment. First, the presence of a seamount chain seems to divide the array into two regiemes on either side of the chain. The one vertical measurement available suggests that this influence is felt at least to the bottom of the main thermocline at a depth of 1500 m. It has been shown that this penetration height into the fluid is consistent with that deduced using a theoretical argument advanced by Prandtl (1952), based on the topographic length scales and measures of rotation and stratification.

Second, oscillations (predominantly in the up-slope velocity component) with periods of 5 to 15 days are present in the very deep measurements of velocity and to a lesser extent in the shallower measurements. It has been shown that these oscillations are not inconsistent with bottom trapped quasigeostrophic oscillations of wavelength near 50 km, as calculated from a simple linear theory. It has been speculated that waves of this wavelength may be generated possibly by the interaction of the larger scale flow in the area with bottom roughness features. There are many pieces of bottom topography in this area with length scales on the order of 10 km., so wavelengths of 50 km. are not unreasonable.

Both of these inferences suffer the same criticism: they arise from an experiment which yielded few good measurements. The lack of current meter data from this area of rough topography makes these inferences somewhat speculative. In retrospect it is regretable that there were not more successful temperature and velocity measurements at 1500 m. and above in this experiment. Looking to the future, however, it is clear that flow patterns over rough topography are sufficiently complicated that moored instruments alone are not enough to adequately sample the physics of these processes. A combination of moored instruments, tracked floats, and closely spaced hydrographic stations (such as in MODE-I) appears to be the best suggestion for field experiments in such areas.

Eventually results obtained thus far may be extendable. The program of site moorings set by Woods Hole Oceanographic Institution will continue into the future, and eventually there will exist time series of temperature and horizontal velocity of several years duration in this area. Because of the relatively long time scales associated with mid-ocean processes, these long term measurements are necessary to understand the complicated structure of currents in this area. Since the bottom topography in this area is typical for the North Atlantic, a knowledge of the effects of these topographic features is necessary to understand dynamics of the mid-ocean.

REFERENCES

Amos, D.E., and L.H. Koopmans (1963) Tables of the Distribution of the Coefficient of Coherence for Stationary Bivariate Gaussian Processes, Sandia Corporation, 328 pages.

Bryan, K. (1973) A Model Study of Abyssal Currents in the Array-2 Area. MODE HOT LINE NEWS, No. 35, Woods Hole Oceanographic Institution, unpublished manuscript.

Crease, J. (1962) Velocity Measurements in the Deep Water of the Western North Atlantic, Jour. Geophys. Res., 67, 3173-3176.

Fofonoff, N.J., and T.F. Webster (1971) Current Measurements in the Western Atlantic, Phil. Trans. Roy. Soc. A, 270, 423-436.

Gould, W.J. (1972a) Current Measurements from Surface and Subsurface Moorings, MODE HOT LINE NEWS, No. 10, Woods Hole Oceanographic Institution, unpublished manuscript.

Gould, W.J. (1972b) SCOR Moorings -- Some Preliminary Results, MODE HOT LINE NEWS, No. 16, Woods Hole Oceanographic Institution, unpublished manuscript.

Gould, W.J., W.S. Schmitz and C. Wunsch (1974) Preliminary Field Results from a Mid Ocean Dynamics Experiment, submitted to Deep Sea Research.

Hogg, N.J. (1973) On the Stratified Taylor Column, J. Fluid Mech., 58, 517-537.

Jenkins, G.M., and D.G. Watts, Spectral Analysis and its Applications, Holden Day, Inc., 524 pages.

Longuet-Higgins, M.S. (1965) Some Dynamical Aspects of Ocean Currents, Q. Jl. Roy. Met. Soc., 91, 425-451.

Phillips, N.A. (1966) Large Scale Eddy Motion in the Western Atlantic, J. Geophys. Res., 71, 3883-3891.

Prandtl, L. (1952) Essentials of Fluid Dynamics, Hafner Publishing Co., 452 pages.

Rhines, P.B. (1970) unpublished manuscript.

Rhines, P.B. (1971a) Edge-, Bottom-, and Rossby Waves in a Rotating Stratified Fluid, Geophys. Fl. Dyn., 1, 273-302.

Rhines, P.B. (1971b) A Comment on the Aries Observations, Phil. Trans. Roy. Soc. A, 270, 461-463.

Schmitz, W.J. (1972a) unpublished manuscript.

Schmitz, W.J. (1972b) Current Measurements from Array-2

MODE HOT LINE NEWS, No. 11, Woods Hole Oceanographic Institution, unpublished manuscript.

Schulman, E.E. (1967) The Baroclinic Instability of a Mid Ocean Circulation, Tellus, 19, 292-305.

Stommel, H.M. (1972) Vertical Modal Structure of Long Period Motions, MODE HOT LINE NEWS, No. 13, Woods Hole Oceanographic Institution, unpublished manuscript.

Suarez, A.A. (1971) The Propagation and Generation of Topographic Oscillations in the Ocean, Ph.D. Thesis, MIT-WHOI.

Sverdrup, H.U. (1957) Wind Driven Currents in a Baroclinic Ocean; with application to the Equatorial Currents of the Western Pacific, Proc. Nat. Acad. Sci., Wash., 33, 318-326.

Swallow, J.C. (1971) The Aries Current Measurements in the Western North Atlantic, Phil. Trans. Roy. Soc. A, 270, 451-460.

Thompson, R.O.R.Y. (1973) Private Communication.

Webster, T.F. (1967) A Scheme for Sampling Deep Sea Currents from Moored Buoys, In Trans. 2nd Intl. Buoy Technology Symposium, p. 419-431, Marine Technology Society, Wash., D.C.

Wunsch, C. (1972) The Spectrum from Two Years to Two Minutes of Temperature Fluctuations in the Main Thermocline at Bermuda, Deep Sea Res., 19, 577-593.

Wunsch, C. and J. Dahlen (1974) A Moored Temperature and Pressure Recorder, to appear in Deep Sea Research.